ORNL-6935

ornl

OAK RIDGE NATIONAL LABORATORY

LOCKHEED MARTIN

GRAIN GROWTH BEHAVIOR AND HIGH-TEMPERATURE HIGH-STRAIN-RATE TENSILE DUCTILITY OF IRIDIUM ALLOY DOP-26

C. G. McKamey
A. N. Gubbi
Y. Lin
J. W. Cohron
E. H. Lee
E. P. George

MANAGED AND OPERATED BY
LOCKHEED MARTIN ENERGY RESEARCH CORPORATION
FOR THE UNITED STATES
DEPARTMENT OF ENERGY

ORNL-27 (3-96)

ORNL-6935

RADIOISOTOPE POWER SYSTEM PROGRAM

GRAIN GROWTH BEHAVIOR AND HIGH-TEMPERATURE HIGH-STRAIN-RATE TENSILE DUCTILITY OF IRIDIUM ALLOY DOP-26

C. G. McKamey, A. N. Gubbi, Y. Lin, J. W. Cohron, E. H. Lee, and E. P. George

April 1998

Prepared for Department of Energy
Office of Engineering and Technology Development
Space and National Security Programs
Under Budget and Reporting Classification AF 70 10 20 0

Prepared by the
OAK RIDGE NATIONAL LABORATORY
Oak Ridge, Tennessee 37831
Managed by
LOCKHEED MARTIN ENERGY RESEARCH CORP.
for the
U.S. DEPARTMENT OF ENERGY
under contract DE-AC05-96OR22464

CONTENTS

GRAIN GROWTH BEHAVIOR AND HIGH-TEMPERATURE HIGH-STRAIN-RATE TENSILE DUCTILITY OF IRIDIUM ALLOY DOP-26*

C. G. McKamey, A. N. Gubbi, Y. Lin, J. W. Cohron, E. H. Lee, and E. P. George

ABSTRACT

This report summarizes results of studies conducted to date under the Iridium Alloy Characterization and Development subtask of the Radioisotope Power System Materials Production and Technology Program to characterize the properties of the new-process iridium-based DOP-26 alloy used for the Cassini space mission. This alloy was developed at Oak Ridge National Laboratory (ORNL) in the early 1980's and is currently used by NASA for cladding and post-impact containment of the radioactive fuel in radioisotope thermoelectric generator (RTG) heat sources which provide electric power for interplanetary spacecraft. Included within this report are data generated on grain growth in vacuum or low-pressure oxygen environments; a comparison of grain growth in vacuum of the clad vent set cup material with sheet material; effect of grain size, test temperature, and oxygen exposure on high-temperature high-strain-rate tensile ductility; and grain growth in vacuum and high-temperature high-strain-rate tensile ductility of welded DOP-26. The data for the new-process material is compared to available old-process data.

INTRODUCTION

Iridium has many interesting properties. It is considered to be the most corrosion-resistant element [1]. It has the highest melting temperature of any of the face-centered-cubic metals (2443°C), the highest density of any element (22.65 g/cm^3), and the second highest shear modulus (220 GN/m^2 at 25°C) of the metals [2]. Its high-temperature strength is second only to tungsten among the refractory metals [3,4]. Because of these properties, and its compatibility with the $^{238}PuO_2$ fuel and external graphitic components, the iridium-based alloy designated DOP-26 was chosen for the fuel containment shell in radioisotope thermoelectric generators (RTGs). RTGs have provided stable electric

*Research sponsored by the Space and National Security Programs at the Oak Ridge National Laboratory, managed by Lockheed Martin Energy Research Corporation for the U.S. Department of Energy under contract No. DE-AC05-96OR22464.

power for various space missions such as Voyagers I & II, Galileo, and Ulysses, and was again used in the recently launched Cassini spacecraft. The fuel shell material has to possess high-temperature high-strain-rate tensile ductility as it needs to survive impact conditions (1273 to 1623 K at a velocity of 50 to 85 m/sec) which might occur in case of an accident during launching or re-entry of the space craft into earth's atmosphere.

The DOP-26 alloy contains nominally 0.3 wt % W to which thorium is added to improve the high-temperature high-strain rate tensile ductility [5-9]. Auger electron spectroscopy has indicated that thorium segregates strongly to the grain boundaries in this alloy [8,10], resulting in increased cohesive strength of the boundaries and a change in fracture mode from brittle intergranular in the undoped alloy to ductile transgranular fracture in the thorium-doped alloy. In addition to segregating to grain boundaries, thorium in excess of the solubility limit (which may be as low as 5-10 wppm [11]) forms a second phase with a composition of Ir_5Th [7,12], which pins the grain boundaries resulting in retarded grain growth [8,13]. Because of its low solubility in iridium, most of the thorium in DOP-26 is present in the form of the Ir_5Th intermetallic particles, the distribution of which depends on the fabrication process. The beneficial effect of thorium is therefore related to both its enrichment at the grain boundaries and its precipitation as Ir_5Th intermetallic particles. The maximum beneficial effect (highest impact ductility) is obtained when thorium is present at a level of 200 wppm [8]. Because this level of Th results in decreased weldability [14], the current generation of DOP-26 alloys contain nominally 60 wppm Th as a compromise between ductility and weldability.

Because grain growth can have a detrimental effect on the high-temperature itensile ductility [9,15], several past studies have concentrated on determining grain growth characteristics of DOP-26, not only in vacuum [13,16], but also in a low-pressure oxygen environment which simulates the type of environment encountered in service [11,15,16]. Earlier studies on DOP-26 material produced by the "old process" [17] (see next section for processing details) showed that, in poor vacuums, where a low partial pressure of oxygen existed, abnormally large grains grew near the surface of the DOP-26 specimen during prolonged heat treatment at temperatures near 1330°C [11]. Concurrent with growth of these near-surface grains (NSGs) was the depletion of thorium from grain boundaries and the reduction in size and eventual disappearance of Ir_5Th precipitates. This phenomenon appeared to involve diffusion of thorium along the grain boundaries to

the external surface of the alloy where it reacted with oxygen to form discrete ThO_2 precipitates [11]. Depletion of segregated thorium and dissolution of Ir_5Th precipitates unpinned the grain boundaries and allowed grain growth to take place.

Recently our efforts to determine the oxygen compatibility of the DOP-26 alloys have been extended to batches of material produced by a new fabrication process (hereafter referred to as "new process", to be defined later), which was designed to improve the yield of DOP-26 alloy blanks [6,18,19]. The objectives for this new series of oxygen compatibility studies are twofold: (1) to determine whether thorium depletion and anomalous grain growth behavior are similar in the old-process and new-process materials; and (2) to determine the effects of changes in oxygen partial pressure and temperature on relative rates of thorium depletion (i.e., to determine if there is some region in pressure-temperature space where the grain-growth kinetics are slower). To date, compabitility studies have been completed at 1230, 1280, and 1330°C with an oxygen partial pressure of 1.3 mPa and at 1330°C with a partial pressure of 13.3 mPa. The results of these studies, as well as data for grain growth in vacuum, are included in this report.

Although uniform grain growth is known to be deleterious to the high-temperature high-strain-rate tensile ductility of iridium-based alloys [8,20], it is not clear how anomalous growth in oxygen affects ductility. Thus, for example, in tensile specimens with a non-uniform grain-size distribution across the gage section, it is not known whether the average or the near-surface grain size controls ductility. Therefore, as a further extension of the grain-growth studies, this report presents data on the high-temperature high-strain-rate tensile ductility of DOP-26 alloy specimens that were exposed to a low partial pressure of oxygen (1.3 mPa) at 1330°C and compares the data to results taken from specimens annealed in vacuum.

In service the fuel capsule is composed of two DOP-26 cups that are welded together and although the properties of welded old-process DOP-26 have been studied [21], the properties of welded new-process DOP-26 have not so far been reported. Additionally, it is known that thorium in large concentrations (~200 wppm and above) is harmful to weldability because it promotes hot cracking by the formation of a low-melting Ir-Ir_5Th eutectic at the fusion-zone grain boundaries [14,21]. It is therefore of interest to determine some of the properties of welded specimens of new-process DOP-26 and to compare that data to available data on old-process DOP-26. The results of grain-growth studies in

vacuum and high-temperature high-strain-rate tensile tests, with ductility measured perpendicular to the welding direction, are included here.

It was also considered important to determine the grain growth characteristics of the completed clad vent set cup, not only as a function of the time and heat treatment temperature, but also as a function of the position in the cup with respect to both the rolling direction and the cup geometry. This report describes the effect of 1-h anneals at temperatures of 1200 to 1800°C and of heat treating for various times at 1400 and 1500°C on the grain growth behavior of clad vent set cup material and compares it to data from DOP-26 sheet material.

EXPERIMENTAL PROCEDURES

Production of Sheet Material

The specified composition for DOP-26 is given in Table I [Ref. 22]. The alloy sheet blanks that were used in these studies were prepared in either of two different methods. In the "old process" [17], the alloys were arc melted and drop cast into water-cooled

Table I. Chemistry of Iridium Alloy DOP-26 (Ref. 22)

Element	Max. Content in µg/g (unless otherwise stated)	
	Bulk[a]	Surface
Ir	Balance	Balance
Al	20-80	200
Si	50	100
Fe	150	300
Cr	25	50
Mo	50	300
C	35	Not required
O	50	Not required
W	2000-4000	Not required
Ta	50	100
Ti	50	100
Ca	50	100
Na	50	100
Th	30-90	300
Rh	150	300

[a] The sum total of all other noble metals (Au, Ag, Ru, Pt, and Pd) shall not exceed 400 µg/g and no other single element shall exceed 50 µg/g. H, He, N, Ne, Ar, Kr, Xe, Rn, and elements with an atomic number higher than 92 are excluded from the analysis.

rectangular copper molds as 500-g ingots. The ingots were clad in molybdenum and hot rolled into sheet blanks of 0.89 mm thickness at temperatures between 1200 and 1000°C. In many cases, these small ingots contained shrinkage cavities which could not be closed during subsequent rolling operations. This porosity appeared as laminar defects in the final blanks, resulting in relatively high rates of rejection of blanks for ultrasonic and dye penetrant indications. In order to improve the product yield and decrease the production costs, an improved manufacturing process was developed and qualified for the production of blanks for the Cassini spacecraft. In this "new process" [6,18,19,23], the alloy was obtained as a 63-mm-diam consumable arc-melted ingot. The ingot was then canned in molybdenum and extruded at 1425°C into a sheet bar. After acid-cleaning the bar was cut iinto sections, clad in molybdenum sheet, and hot rolled into 0.86-mm-thick sheet at temperatures between 1200 and 1000°C, with one intermediate vacuum anneal at approximately 1300°C. (A more detailed description of the old and new fabrication processes can be found in Ref. 23.) In both old and new processes, following hot rolling, the top and bottom surfaces of the sheets were ground, were electrolytically cleaned in an aqueous solution of KCN, and then were acid cleaned in a solution containing 3 parts HCl, 1 part HF and 1 part water to remove impurities or oxide scales from the surfaces. The final thickness was approximately 0.75 mm.

As discussed elsewhere [17-19,23], the distribution of Ir_5Th intermetallic particles in DOP-26 alloys depends on the fabrication process. In the old-process material, the 1 μm diameter intermetallic particles are equiaxed and are fairly evenly dispersed through the matrix [see Fig. 1(a)]. In the currently-used new process, the particles tend to be elongated and 3-4 μm in length [see Fig. 1(b)]. They also tend to occur in stringers (produced during rolling or extruding) along the rolling direction, rather than being evenly dispersed throughout the matrix.

Grain-Growth Behavior in Vacuum and Low-Pressure Oxygen

Specimens for grain growth studies were cut by electrical discharge machining from rejected blanks from the ZR (old-process) and D2 and E2 (new-process) heats. Approximately 0.1 mm was ground from the edges of the specimens to remove any damage produced by the machining. For the vacuum anneals, specimens were annealed in a vacuum better than 0.7 mPa (5 x10^{-6} torr) for various times at temperatures ranging

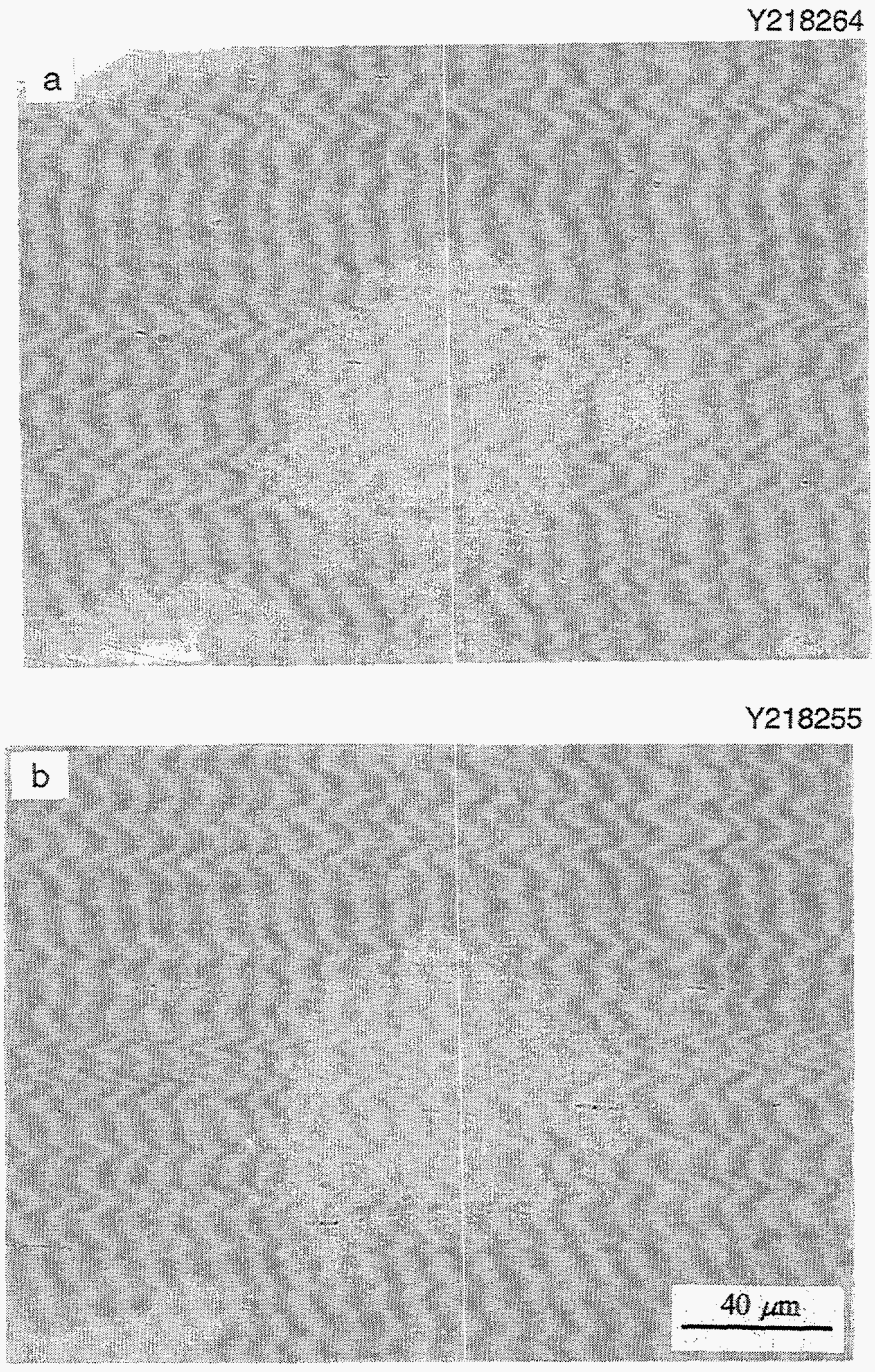

Fig. 1. Optical micrographs of unetched DOP-26 alloys showing (a) uniform distribution of Ir_5Th precipitates in old-process ZR material and (b) precipitate stringers in new process D2 material. Rolling direction is horizontal to the micrographs.

from 1300 to 1800°C. For heat treatments in low pressure oxygen, samples were first recrystallized for 1 h at 1375°C in vacuum (10^{-4} Pa range). Oxygen anneals for times up to 3000 h were then performed in a dynamically pumped tube furnace having a base pressure of 0.4 mPa (3 x 10^{-6} torr) at the elevated temperatures. Oxygen anneals were performed at two different oxygen partial pressures: 1.3 mPa at temperatures of 1230, 1280, and 1330°C and 13.3 mPa at 1330°C.

Metallography samples, which were approximately 5x10x0.75 mm, were polished and then electrolytically etched in a solution of 400 ml H_2O, 100 ml HCl, and ≈2.5 g NaCl, using a current of 0.9 A at an applied potential of approximately 10 V AC for 4-5 min. Grain sizes were measured by the linear intercept method in a plane transverse to the rolling direction. In this plane, grain diameters were determined in both the short transverse (ST) (i.e., perpendicular to the plane of the sheet) and long transverse (LT) (i.e., parallel to the plane of the sheet) directions. In the oxygen-annealed specimens, grain sizes were also measured in the LT direction as a function of depth from the specimen surface. Grain size measurements are recorded here as the average values obtained from 2-4 fields in each specimen. An exact determination of the actual grain size of the material would also have to take into consideration differences between ingots and between regions in each ingot. Other important factors affecting the grain size measurements are rounding at the edges of the sample during grinding and polishing, the difficulty in etching iridium alloys to reveal all grain boundaries, and uneven flow patterns of the oxygen around the specimens while they are in the furnace. Because these and other factors make it difficult to calculate a meaningful standard deviation for the data points, no error bars are included with the data. Instead, the confidence limits of the data are indicated by the number of intercepts counted for each data point and are recorded in parentheses in the tables.

Auger electron spectroscopy (AES) was employed for analyzing the grain boundaries of samples which had been annealed for 3000-h in oxygen partial pressures of 1.3 or 13.3 mPa at 1330°C. For comparison, samples which had not been exposed to oxygen (designated as 0-h oxygen anneal) were also analyzed. Average grain boundary thorium concentration was determined as a function of depth from the free surface of the samples. Auger analyses were performed using a Perkin-Elmer PHI 590 Scanning Auger Microprobe on specimens with approximate dimensions of 0.63 x 3 x 12 mm which had

been notched at the center and fractured by bending impact at room temperature under a vacuum better than 10^{-7} Pa (10^{-9} torr). The fractured samples were transferred in front of a cylindrical mirror analyzer and the fracture surfaces were analyzed with a beam voltage of 5 kV and a beam current of 6-8 nA. For both the 0-h and 3000-h oxygen-annealed samples, at least 5 grain boundaries were analyzed at each of ≈50 μm depth intervals from the surface to the center of the samples. In addition, at least two NSGs were analyzed at a depth interval of ≈8 μm for 0-h and ≈10 μm for 3000-h samples. The atomic concentrations of thorium at the grain boundaries were determined by a method explained elsewhere [24] using sensitivity factors for corresponding peaks of thorium and iridium specifically obtained for the PHI 590 AES system.

Grain Growth Behavior of Cassini Clad Vent Set Cup Material

Specimens for grain growth studies were cut from rejected clad vent set cups that had been fabricated using the "new-process". These cups had previously been designated as 3624-01-2783 (from the ER8 heat), 3624-30-2045 (from the E4 heat), and 3625-00-2409 (from the D2 heat). Figure 2 shows a schematic (not to scale) of the cups and shows the areas that were analyzed for grain size. These areas have been designated as top, bend, and center regions. Through visual inspection, the rolling direction was determined, and the cups were sliced and numbered with respect to the rolling direction (RD)

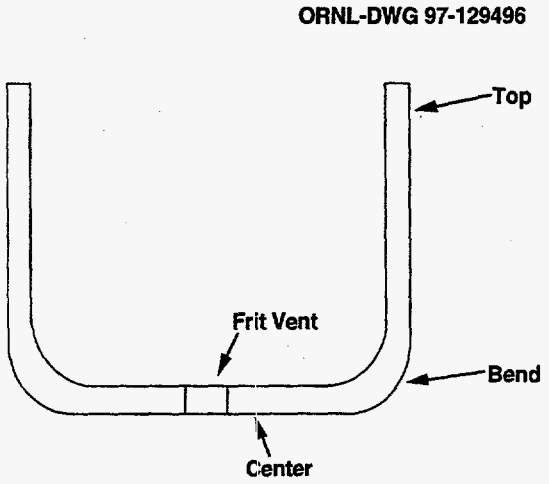

Fig. 2. Schematic showing the top, bend, and center locations of a clad vent set cup where grain sizes were measured.

according to the schematic shown in Fig. 3. Grain size data were determined not only for the top, bend, and center regions of the cup, but also for specimens cut 0, 45, and 90° to the rolling direction. One-hour heat treatments at temperatures of 1200-1800°C and heat treatments for various times at 1400 and 1500°C were performed in a vacuum of 10^{-4} Pa. After heat treating, the specimens were mounted, polished, and then electrolytically etched as described above. Grain sizes were measured by the method of linear intercepts in the direction perpendicular to the cut specimen.

High-Temperature High-Strain-Rate Tensile Ductility

The current specifications for iridium tensile specimens include a gage section of 0.64 x 2.54 x 11.43 mm, a total length of approximately 43 mm, and a fillet with a radius of 6.35 mm between the gage section and grip ends. In order to fit into the grips of the impact tester, one grip end is slightly larger than the other and the smaller end is reinforced with iridium tabs. Using these dimensions, specimens for this study were electrical-discharge machined (EDM) and then all surfaces of the gage section were ground through at least a 600-grit SiC finish. Prior to testing, specimens of new-process DOP-26 were annealed for 1 h at temperatures between 1300 and 1800°C in order to obtain different

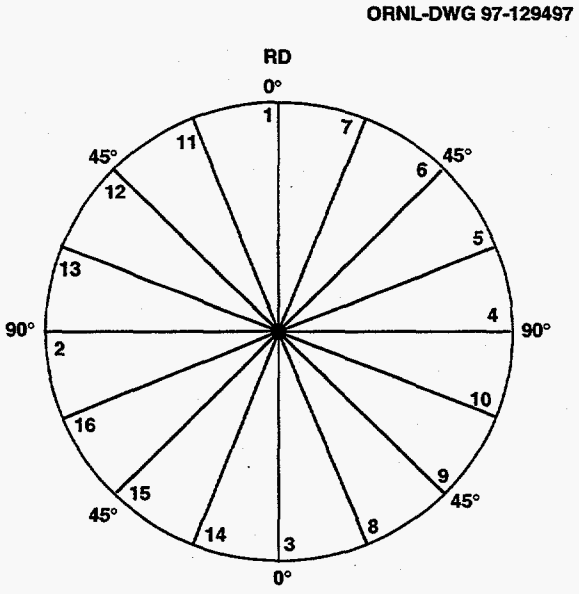

Fig. 3. Schematic showing cutting and labelling scheme for clad vent set cup material.

grain sizes (ranging from ~21 to 117 μm). Specimens of old-process DOP-26 were annealed for 1 h at 1500°C to obtain a grain size (~32 μm) similar to that of new-process DOP-26 for a comparative study of the two alloys. A comparison of some of the data was also made to data taken using an "old specimen" design. In the old design [5,8,9], 3.18 mm was specified as the fillet radius between the gage section and grip ends, and there were no specifications for surface finish or the use of extra tabs to strengthen the grip ends. This design sometimes resulted in premature fracture either in the fillet or the pin holes, resulting in uninterpretable results. For this reason, the new specimen design has been used since about 1991.

High-temperature high-strain-rate tensile testing was carried out using specially designed testing equipment developed at Oak Ridge National Laboratory, the details of which are given elsewhere [5,8,9]. (In the past these tests have sometimes been referred to as "impact tests" because, in order to generate the necessary strain rate, they are performed by impacting a "bullet" onto a small rectangular plate connected on each side to an iridium tensile specimen.) Tests were performed on samples of new- and old-process DOP-26 at a constant bullet velocity of 61 ± 3 m/s and at test temperatures between 600 and 1200°C (controlled to within ± 10°C). Samples of new-process DOP-26 with different grain sizes and old process DOP-26 at a constant grain size were tested. The fracture surfaces of the samples were examined in a scanning electron microscope.

Specimens for grain size determinations were cut from tested tensile specimens and were metallographically prepared as noted above. Grain sizes were measured by the method of linear intercepts in a plane transverse to the rolling direction, and in a direction perpendicular to the plane of the sheet (short transverse direction, ST).

Effect of Low-Pressure Oxygen Exposure on High-Temperature High-Strain-Rate Tensile Ductility

The specimens for this study were taken from rejected blanks; the blanks were from heats A604 (old process) and F2 (new process). Specimens were cut from the blanks by electrical discharge machining and the surfaces were prepared as noted above. For recrystallization, all specimens were annealed in a vacuum better than 0.7 mPa (5×10^{-6} torr) for 1 h at 1375°C. Anneals in a partial oxygen pressure of 1.3 mPa were performed at 1330°C in the same high-temperature furnace used for the oxygen-anneals described above. The base pressure was approximately 0.4 mPa (3×10^{-6} torr) at 1330°C.

High-temperature high-strain-rate tensile testing was performed as noted above on specimens from both processes at temperatures between 800 and 1300°C (controlled to within ±10°C). Several specimens from both old and new process material in the as-recrystallized condition were also tested to serve as controls. Due to the limited number of specimens available, only one test of new-process and one of old-process material were performed for each test condition. The failure modes were determined using scanning electron microscopy (SEM).

Specimens for grain size measurements were cut from the grip ends of the specimens and were polished and etched as described above. Grain sizes were determined by the linear intercept method in the ST direction in a plane transverse to the rolling direction of the blank. The grain size is reported as the average of five traverses across the thickness of two different fields (for a total of 10 traverses).

Grain Growth Behavior and High-Temperature High-Strain-Rate Tensile Ductility of Welded DOP-26

Non-flight-quality new-process DOP-26 alloy blanks designated FR3-6 and ER6-15 were selected for this study. They were acid-cleaned and given a recrystallization anneal of 1 h at 1300°C. A gas-tungsten-arc weld was then performed down the center of the blank using the following welding parameters: 125 amperes DC straight polarity (electrode negative), 12.7 mm/s (30 in./min) travel speed, 0.89 mm (0.035 in.) arc length, in an argon atmosphere containing <10 ppm oxygen and <50 ppm water vapor. The welding direction was perpendicular to the rolling direction. Tensile samples for impact testing (~11.8 mm gage length) and approximately 0.5 by 1.0 cm rectangular samples for grain-growth studies were cut in a direction perpendicular to the weld (parallel to the rolling direction). Specimens for grain-growth studies were annealed in a vacuum furnace that had been evacuated to a pressure of approximately 2×10^{-4} Pa. Annealing times of up to approximately 1000 h at temperatures of 1400 and 1500°C were used. After heat treatment, the samples were metallographically prepared and electrolytically etched as described above. Grain sizes for the base metal, weld centerline, and the weld region about 500 μm from the centerline (referred to as "weld metal" in this report) were measured by the linear intercept method in a plane transverse to the welding direction, in the short transverse (ST) direction. The tensile impact specimens were annealed for 19 h at

1500°C before testing at temperatures from 900 to 1200°C. A bullet velocity of 66 m/s (200 ft/s) was used for all impact tests.

GRAIN-GROWTH BEHAVIOR IN VACUUM AND LOW-PRESSURE OXYGEN

Results

Unetched micrographs of the old-process ZR and new-process D2 materials depicting the distribution of Ir_5Th precipitates after recrystallization at 1375°C are shown in Figs. 1(a) and (b), respectively. In both cases the rolling direction was parallel to the long dimension of the micrographs. The old-process ZR material had a fairly even distribution of precipitates of approximately 1 μm size, while the new-process D2 material had stringers of 3-4 μm precipitates distributed parallel to the rolling direction.

Vacuum Annealing

Table II and Fig. 4 illustrate the effect of annealing temperature on the grain size of new- and old-process DOP-26 heat treated in vacuum for 1 h. In general, grain size increased with increasing temperature for both alloys and for both orientations. At any given temperature, the grain size in the ST direction was smaller than in the LT direction, consistent with the anisotropy produced by rolling. Figure 4(a) shows that for all heat treatment temperatures the grain size in the ST direction was essentially the same for both the old- and new-processes. However, the results plotted in Fig. 4(b) suggest that the grain size in the LT direction of the new-process alloy continued to increase, while grain growth in the old-process alloy had slowed somewhat.

Table II. Comparison of Average Grain Sizes of ZR (old process) and D2 (new process) DOP-26 Alloys After 1 h Vacuum Anneals at Various Temperatures

Temperature (°C)	ST direction		LT direction	
	ZR (μm)	D2 (μm)	ZR (μm)	D2 (μm)
1300	15 (268)	24 (170)	33 (126)	46 (90)
1400	23 (204)	29 (199)	39 (122)	59 (159)
1500	30 (201)	33 (60)	45 (102)	55 (67)
1600	45 (182)	48 (38)	59 (143)	70 (66)
1700	90 (124)	69 (164)	94 (98)	97 (122)
1800	99 (107)	117 (94)	111 (83)	156 (76)

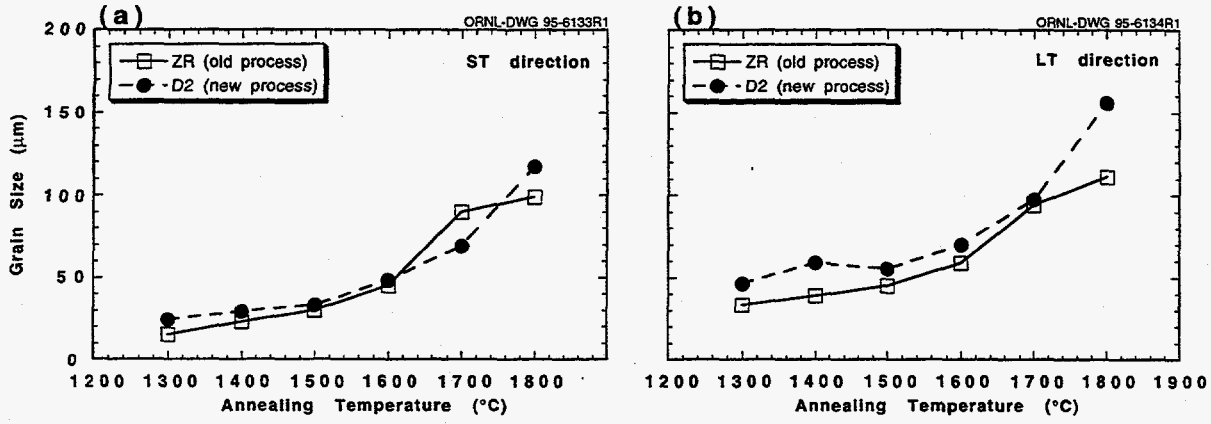

Fig. 4. The effect of 1-h anneals (in vacuum) on the grain size of the old-process ZR and new-process D2 DOP-26 iridium alloys, measured in the (a) short transverse (ST) and (b) long transverse (LT) directions.

Figure 5 and Table III show the variation of grain size (in the ST direction) as a function of annealing time at 1300, 1400, 1500, and 1600°C. The data in each case show an initial high grain-growth rate followed by a leveling-off of the curve. This type of behavior is considered typical for systems in which grain boundaries are pinned by precipitates [25-27].

Low-pressure Oxygen Annealing – 1.3 mPa Oxygen

Low-pressure oxygen anneals of the old-process ZR and new-process D2 and E2 materials were conducted as a function of time at temperatures of 1230, 1280, and 1330°C in an oxygen partial pressure of 1.3 mPa. The grain growth data for all three materials at all three temperatures are presented in Tables IV-VI. Data comparing the grain growth behavior of the old- to new-process material at each of the three annealing temperatures, for both the ST and LT directions, are plotted in Fig. 6, and the effect of annealing temperature on average grain size in the ST direction as a function of time is shown in Fig. 7. The grain sizes after the recrystallization anneal (1 h at 1375°C) are plotted as the initial grain size at 0-time. To save space and for clarity of presentation, in these plots and those to follow, only the D2 data is shown to represent the new-process material (as indicated in Tables IV-VI, results for both D2 and E2 materials were similar). The data in Figs. 6 and 7 illustrate several important points. (1) There was no indication of any significant difference in grain-growth characteristics between the old-process ZR

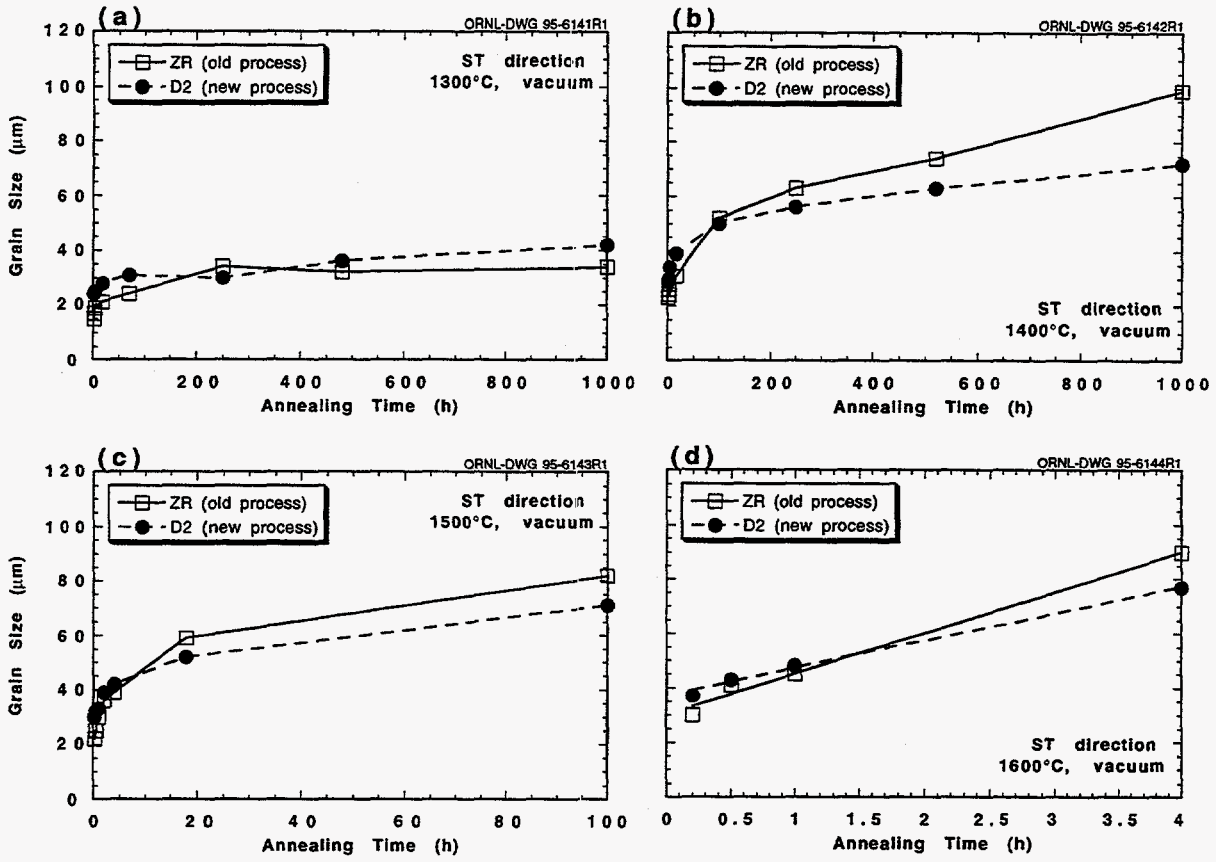

Fig. 5. Grain size versus annealing time in vacuum at (a) 1300, (b) 1400, (c) 1500, and (d) 1600°C for ZR and D2 DOP-26 iridium alloys.

material and the new-process D2 material. Therefore the difference in the morphology of the Ir_5Th distribution does not appear to affect grain growth dramatically. (2) The average grain size difference between the ST and LT directions was maintained up to the 3000 h exposure at each temperature tested. It therefore appears that longer times or higher temperatures are required to destroy the anisotropy produced by rolling and to produce equiaxed grains. (3) Slow, uniform grain growth was observed for both materials tested at 1230°C up to the 3000-h limit of the tests (see optical micrograph of ZR material in Fig. 8). For the tests at 1280 and 1330°C, the fastest grain growth for both alloys occurred in the first two weeks, after which time the rate of grain growth for the 1280°C test leveled off and remained fairly constant, while at 1330°C, grain growth appeared to continue through at least 2250 h of exposure before beginning to slow down. A comparison of the data for all three test temperatures for each alloy (Fig. 7) indicated that only the 1330°C test for the

Table III. Average Grain Sizes in ST Direction for ZR (old process) and D2 (new process) DOP-26 Alloys as a Function of Annealing Time at 1300-1600°C

Temperature (°C)	Length of Anneal (h)	Grain size (μm)	
		ZR (old process)	D2 (new process)
1300	1	15 (268)	24 (322)
	2	17 (232)	
	4	19 (94)	25 (166)
	18	21 (128)	28 (289)
	70	24 (329)	31 (340)
	250	34 (223)	30 (404)
	480	32 (282)	36 (274)
	1000	34 (146)	42 (138)
1400	1	23 (340)	29 (397)
	2	26 (208)	30 (134)
	4	24 (317)	34 (300)
	16	31 (310)	39 (283)
	100	52 (218)	50 (210)
	250	63 (40)	56 (153)
	520	74 (59)	63 (73)
	1000	99 (109)	72 (159)
1500	0.2	22 (367)	30 (336)
	0.5	25 (331)	32 (302)
	1	30 (225)	33 (80)
	2	36 (310)	39 (123)
	4	39 (233)	42 (192)
	18	59 (165)	52 (194)
	100	82 (127)	71 (153)
1600	0.2	30 (352)	37 (292)
	0.5	41 (169)	43 (134)
	1	45 (182)	48 (74)
	4	90 (70)	77 (161)

longer exposure times produced significant grain growth. The optical microstructures of the ZR and D2 materials oxygen annealed for various times at 1330°C are shown in Figs. 9 and 10, respectively. The rolling direction is in the long direction of the micrograph. In both alloys, a duplex microstructure, with larger grains near the surface, was observed after long-time exposures.

In order to determine if there was any difference in growth of near-surface grains (NSGs) for the two materials tested, and to gain an understanding of the rates of dissolu-

Table IV. Grain Size for DOP-26 Alloys as a Function of Exposure Time at 1230°C and an Oxygen Partial Pressure of 1.3 mPa

Exposure time (h)	Grain Size (μm)[a,b]					
	ZR (old process)		D2 (new process)		E2 (new process)	
	ST	LT	ST	LT	ST	LT
0	15.4 (965)	23.7 (1172)	22.5 (641)	37.2 (749)	23.8 (627)	37.8 (735)
768	22.1 (675)	32.3 (864)	27.1 (535)	41.7 (675)	26.8 (555)	45.3 (611)
1512	25.0 (598)	35.4 (785)	29.0 (497)	45.2 (612)	31.8 (468)	44.4 (629)
2252	29.0 (514)	37.9 (743)	27.8 (521)	43.2 (653)	33.5 (445)	57.1 (485)
3000	29.1 (516)	39.6 (711)	31.4 (460)	47.8 (589)	31.2 (475)	46.2 (612)

[a]Number in parentheses indicates the number of intercepts counted.
[b]ST=short transverse (perpendicular to rolling direction); LT=longitudinal (along rolling direction).

Table V. Grain Size for DOP-26 Alloys as a Function of Exposure Time at 1280°C and an Oxygen Partial Pressure of 1.33 mPa

Exposure time (h)	Grain Size (μm)[a,b]					
	ZR (old process)		D2 (new process)		E2 (new process)	
	ST	LT	ST	LT	ST	LT
0	18.0 (863)	31.3 (891)	22.7 (687)	37.0 (771)	16.7 (920)	30.4 (925)
144	26.6 (593)	40.9 (691)	26.5 (598)	45.2 (622)	22.3 (686)	35.3 (808)
380	31.1 (509)	49.1 (608)	32.5 (495)	54.3 (524)	25.9 (576)	40.0 (696)
764	35.0 (453)	53.7 (528)	35.3 (462)	53.9 (525)	28.0 (538)	41.0 (689)
1508	40.4 (400)	54.1 (540)	35.5 (445)	61.1 (469)	34.5 (454)	50.8 (583)
2250	41.2 (365)	50.3 (556)	35.4 (424)	55.2 (514)	33.8 (437)	51.7 (550)
3000	41.9 (352)	56.0 (531)	40.2 (376)	64.8 (444)	37.1 (400)	55.6 (523)

[a]Number in parentheses indicates the number of intercepts counted.
[b]ST=short transverse (perpendicular to rolling direction); LT=longitudinal (along rolling direction).

tion of Ir_5Th particles and diffusion of thorium to the surface, average grain size was also measured in the LT direction as a function of distance from the outer surface of the specimen. The data for the old-process ZR and new-process D2 and E2 materials tested at 1230, 1280, and 1330°C are presented in Tables VII-IX, respectively. The data for the 1330°C test are plotted in Fig. 11 for both the old-process ZR and new-process D2 materials exposed for times of 0, 340 h (2 weeks), 1524 h (2 months), and 3000 h (4 months). The data in this figure show a more rapid increase in NSG size after two months of exposure, particularly for the ZR alloy. At the end of 3000 h, the average grain size for the

Table VI. Grain Size for DOP-26 Alloys as a Function of Exposure Time at 1330°C and an Oxygen Partial Pressure of 1.33 mPa

Exposure time (h)	Grain Size (μm)[a,b]					
	ZR (old process)		D2 (new process)		E2 (new process)	
	ST	LT	ST	LT	ST	LT
0	16.0 (413)	28.4 (884)	19.1 (330)	35.9 (763)	22.9 (236)	47.2 (435)
166	26.3 (251)	37.2 (675)	26.5 (238)	44.7 (612)	33.4 (208)	58.4 (464)
340	34.0 (194)	43.0 (583)	29.3 (215)	46.4 (589)	37.2 (196)	66.2 (413)
760	37.4 (179)	51.2 (494)	38.2 (165)	52.3 (523)	38.7 (168)	69.1 (396)
1524	44.9 (147)	58.5 (429)	37.8 (172)	58.7 (466)	60.0 (231)	84.7 (>1000)
2265	62.0 (213)	70.0 (358)	54.6 (238)	75.0 (365)	57.6 (254)	85.8 (>1000)
3000	54.6 (238)	69.8 (392)	50.4 (133)	70.7 (387)	61.6 (240)	87.7 (>1000)

[a]Number in parentheses indicates the number of intercepts counted.
[b]ST=short transverse (perpendicular to rolling direction); LT=longitudinal (along rolling direction).

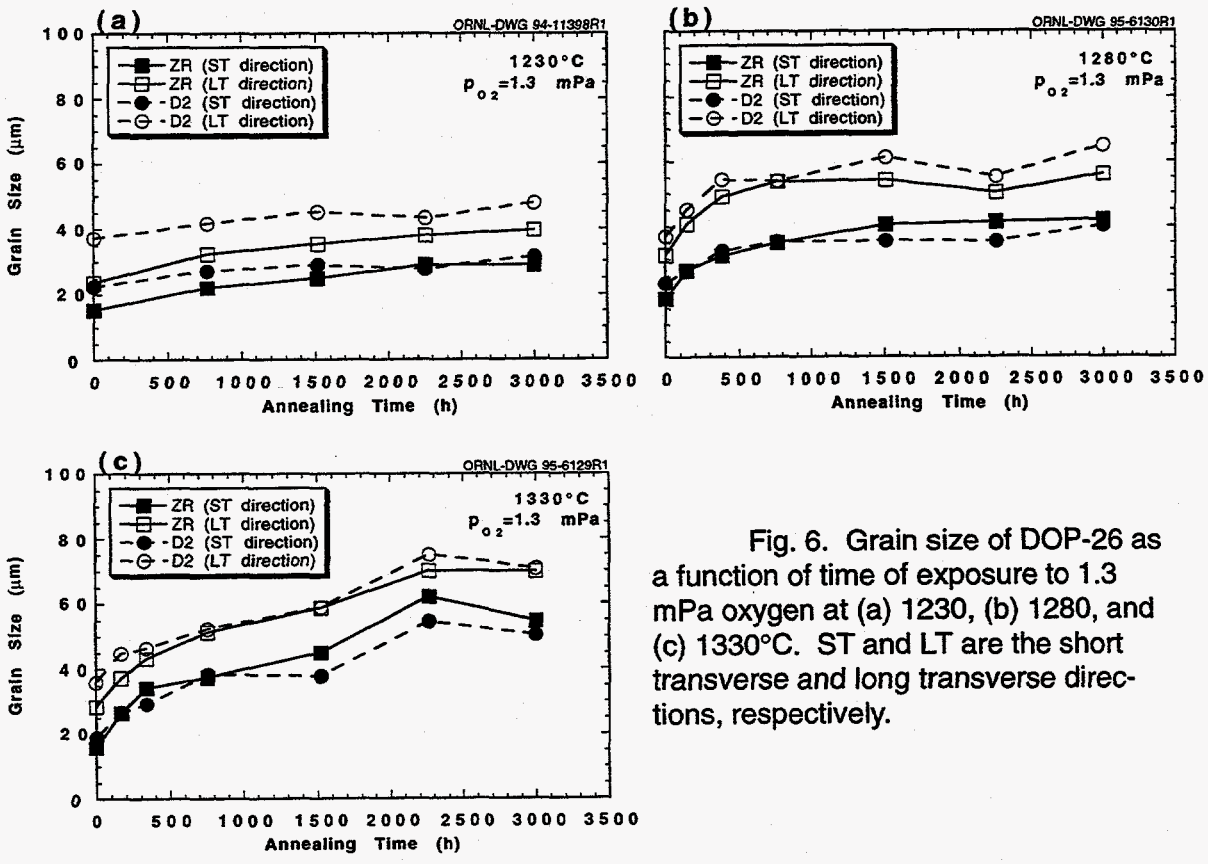

Fig. 6. Grain size of DOP-26 as a function of time of exposure to 1.3 mPa oxygen at (a) 1230, (b) 1280, and (c) 1330°C. ST and LT are the short transverse and long transverse directions, respectively.

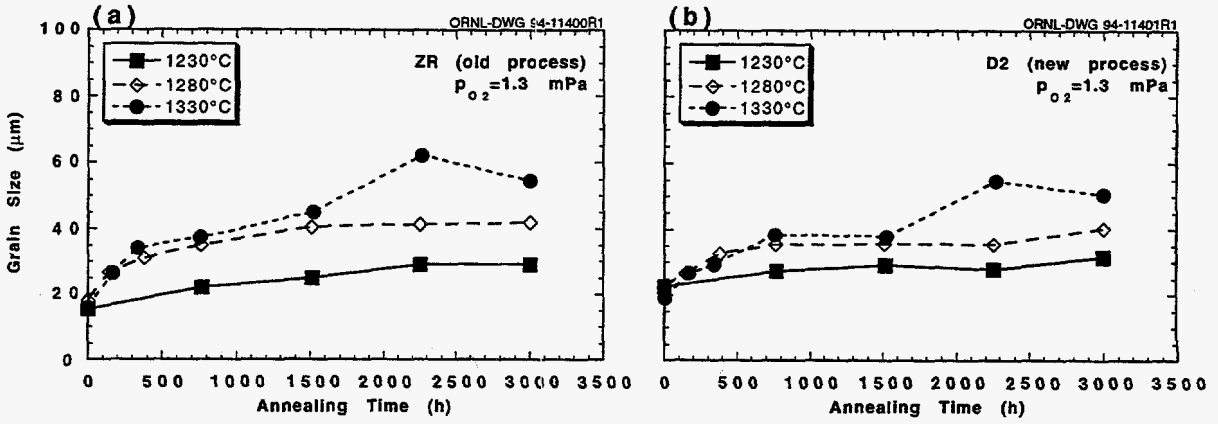

Fig. 7. Comparison of the grain size (measured in the short transverse direction) as a function of time of exposure to 1.3 mPa oxygen at 1230, 1280, and 1330°C for (a) old-process ZR and (b) new-process D2 alloys.

ORNL-PHOTO 129543-97

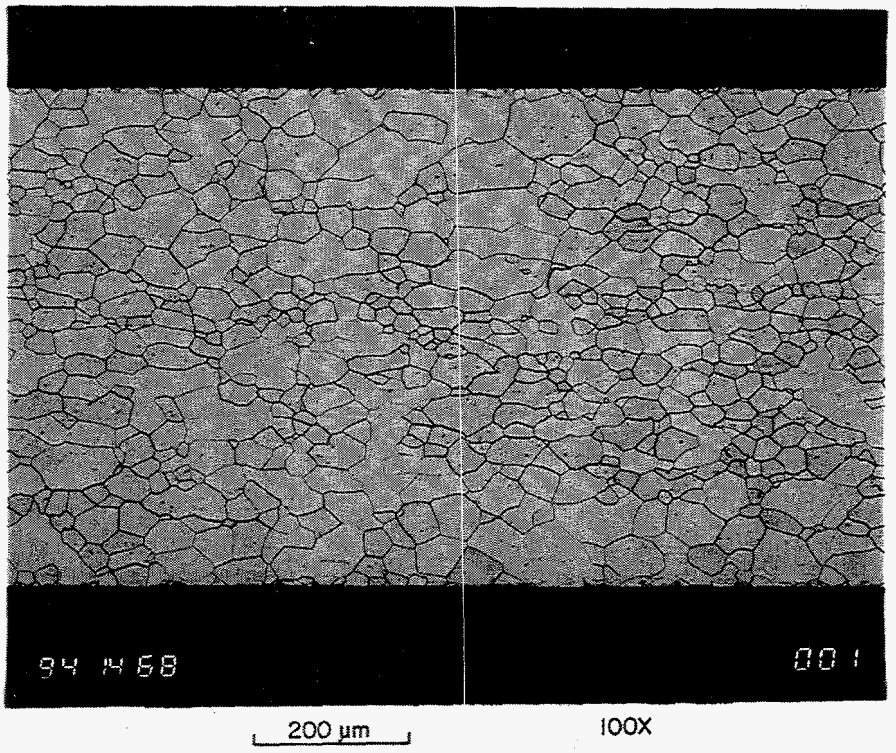

Fig. 8. Optical micrograph of the old-process ZR material after 3000 h of exposure to 1.3 mPa oxygen at 1230°C.

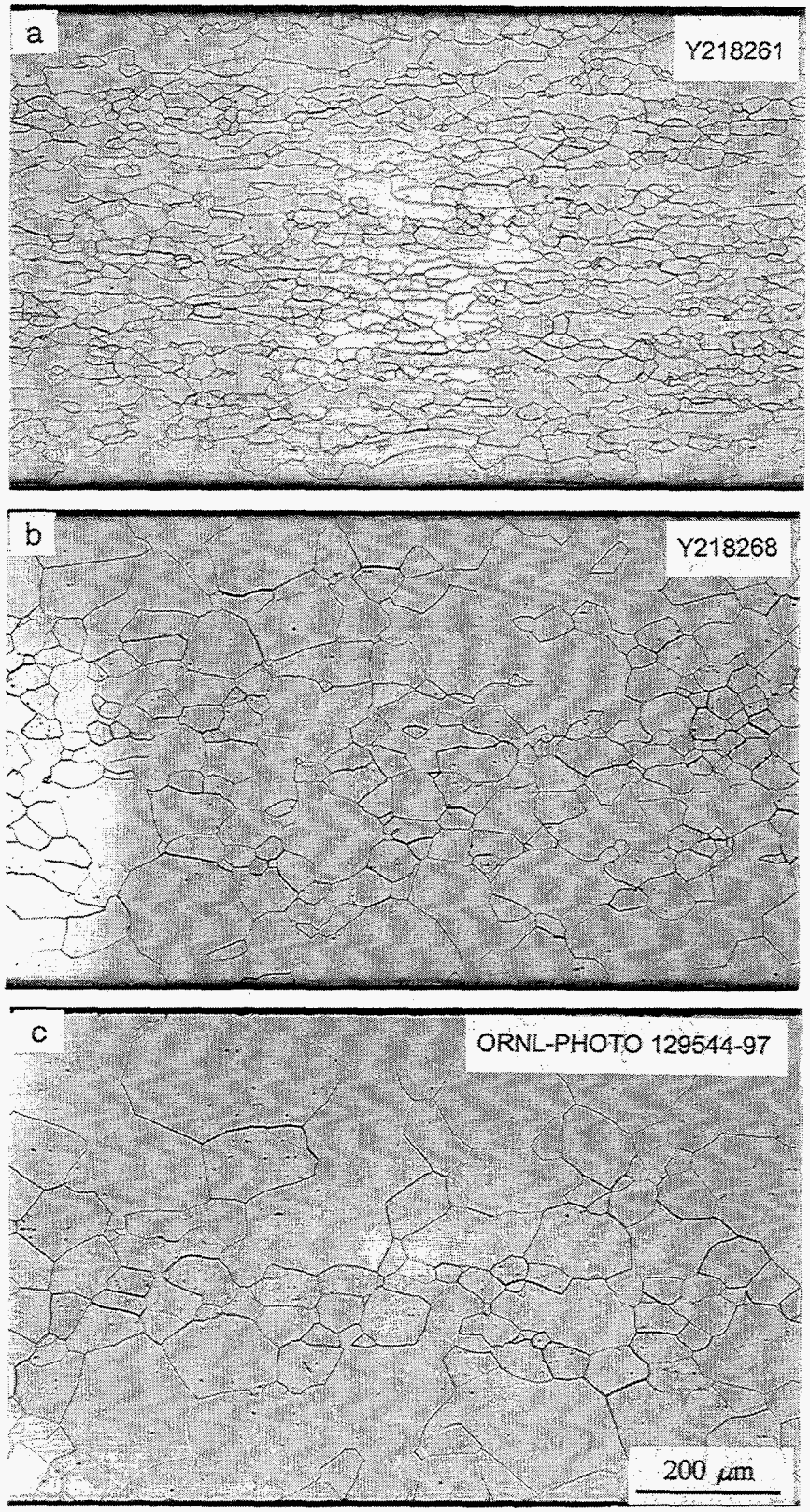

Fig. 9. Optical micrographs of old-process ZR material exposed at 1330°C to 1.3 mPa oxygen: (a) no exposure, (b) 760 h (1 month), and (c) 3000 h (4 months).

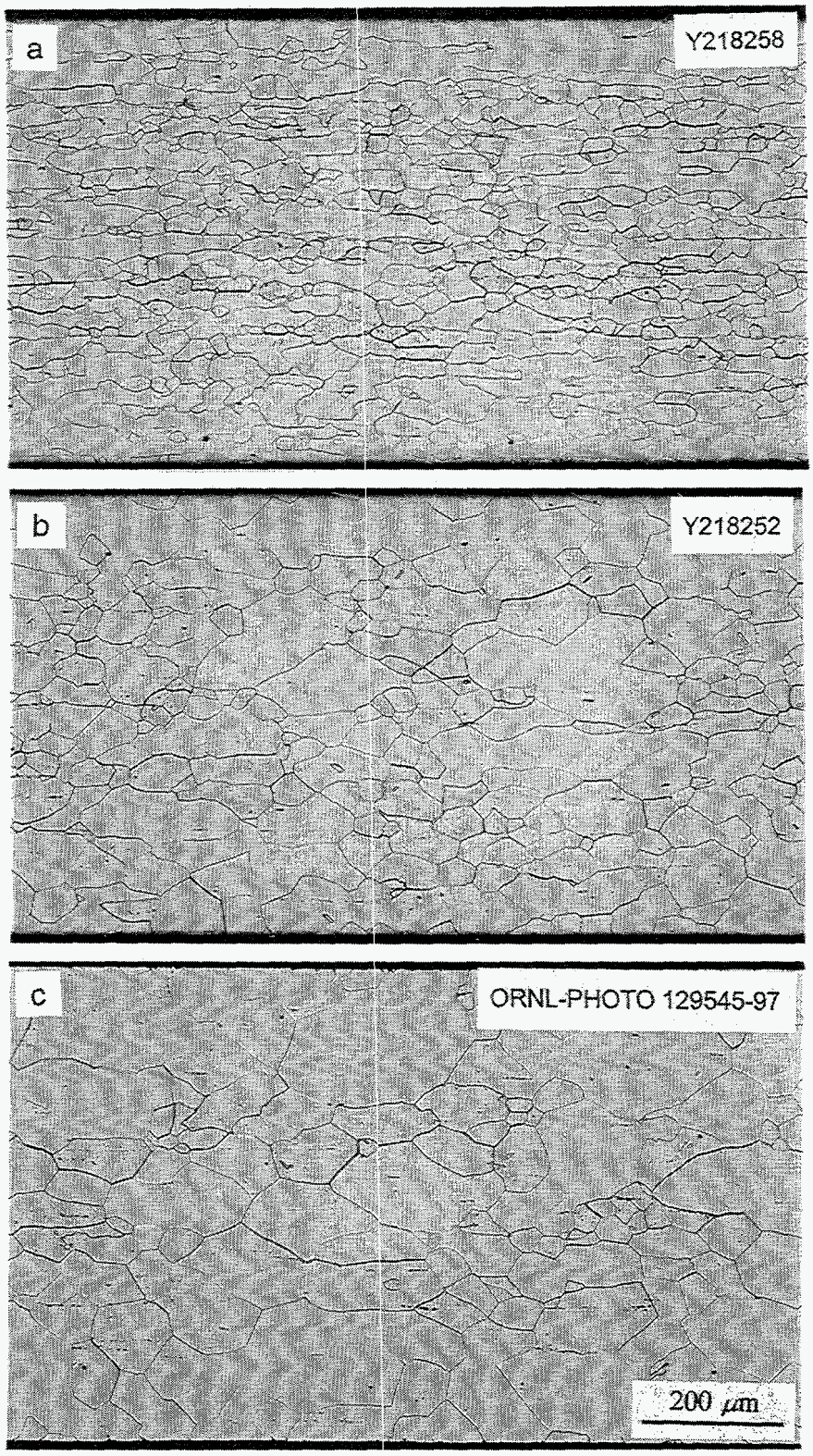

Fig. 10. Optical micrographs of new-process D2 material exposed at 1330°C to 1.3 mPa oxygen: (a) no exposure, (b) 760 h (1 month), and (c) 3000 h (4 months).

Table VII. Average Grain Size as a Function Depth Below the Surface of the Specimen for Old-and New-process DOP-26 Exposed to an Oxygen Partial Pressure of 1.3 mPa at 1230°C

Length of Anneal (h)	Depth below surface (μm)					
	50	100	150	200	250	300
ZR						
0	23.6 (195)	26.2 (180)	23.8 (192)	25.2 (181)	20.5 (223)	22.8 (201)
768	36.2 (129)	30.6 (150)	31.6 (146)	36.9 (124)	29.8 (156)	28.8 (159)
1512	38.7 (118)	34.2 (134)	33.4 (138)	35.2 (130)	36.7 (128)	34.0 (137)
2252	48.8 (96)	37.9 (121)	36.2 (127)	34.3 (135)	38.4(120)	31.8 (144)
3000	47.2 (98)	42.8 (109)	39.5 (116)	36.4 (128)	38.6 (119)	33.1 (141)
D2						
0	39.2 (121)	36.4 (128)	42.1 (110)	35.7 (128)	35.8 (128)	34.2 (134)
768	43.4 (110)	40.6 (113)	43.5 (107)	39.5 (119)	41.7 (114)	41.3 (112)
1512	41.1 (111)	47.1 (98)	51.6 (89)	45.4 (101)	44.3 (103)	41.7 (110)
2252	52.2 (88)	43.5 (105)	47.0 (99)	38.6 (120)	39.8 (119)	37.9 (122)
3000	55.5 (84)	51.2 (90)	49.1 (96)	45.8 (101)	39.8 (117)	45.2 (101)
E2						
0	43.1 (108)	37.7 (123)	36.8 (125)	36.0 (129)	37.5 (123)	36.0 (127)
768	47.3 (98)	43.2 (106)	47.3 (97)	46.6 (99)	43.3 (106)	43.9 (105)
1512	54.2 (85)	44.3 (104)	46.4 (99)	42.6 (107)	39.0 (119)	39.8 (115)
2252	57.8 (79)	56.8 (82)	56.3 (82)	60.9 (75)	55.2 (83)	55.4 (84)
3000	56.8 (87)	45.2 (101)	46.9 (98)	41.8 (110)	43.0 (108)	43.6 (108)

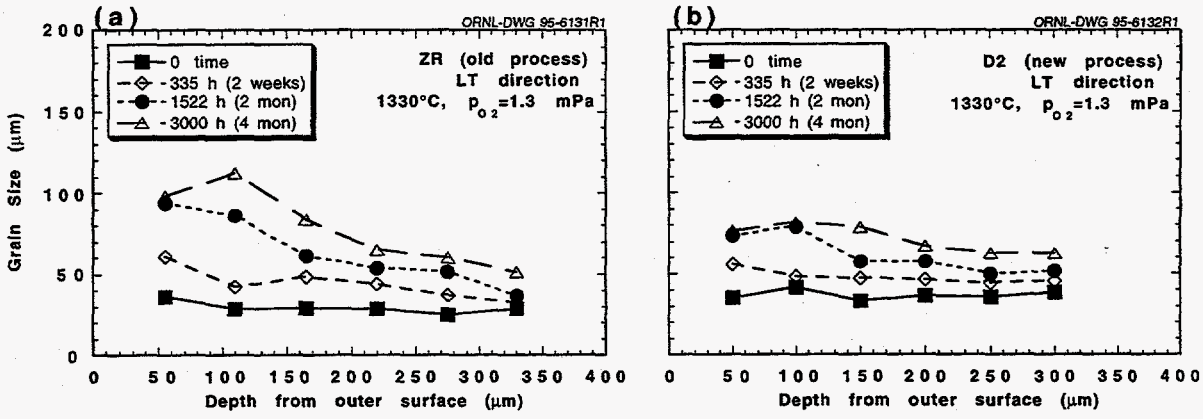

Fig. 11. Grain size as a function of depth into the specimen for (a) ZR material and (b) D2 material after exposure to 1.3 mPa oxygen at 1330°C for 0 time, 335 h (2 weeks), 1522 h (2 months), and 3002 h (4 months).

Table VIII. Average Grain Size as a Function Depth Below the Surface of the Specimen for Old- and New-process DOP-26 Exposed to an Oxygen Partial Pressure of 1.3 mPa at 1280°C

Length of Anneal (h)	Depth below surface (μm)					
	50	100	150	200	250	300
ZR						
0	35.0 (133)	32.8 (139)	30.5 (150)	33.5 (140)	29.5 (155)	26.6 (174)
144	44.0 (106)	47.7 (98)	37.8 (121)	40.9 (113)	39.6 (123)	35.4 (130)
380	63.4 (73)	59.3 (84)	42.9 (110)	47.4 (99)	48.1 (104)	33.6 (138)
764	68.0 (70)	56.6 (81)	56.6 (81)	50.2 (91)	45.6 (104)	45.4 (101)
1508	74.9 (62)	69.4 (67)	42.1 (109)	41.6 (110)	43.6 (105)	52.8 (87)
2250	59.5 (77)	56.3 (81)	52.2 (88)	44.0 (105)	45.1 (102)	44.5 (103)
3000	78.4 (59)	73.8 (66)	49.5 (94)	46.3 (102)	44.1 (105)	44.1 (105)
D2						
0	35.0 (131)	41.2 (116)	39.6 (118)	34.9 (140)	37.4 (129)	34.1 (137)
144	49.9 (92)	50.0 (93)	44.3 (103)	46.3 (102)	43.4 (107)	37.1 (125)
380	65.4 (70)	56.6 (81)	47.0 (103)	49.5 (94)	57.3 (85)	50.2 (91)
764	56.5 (82)	58.9 (79)	54.5 (84)	49.2 (94)	51.9 (99)	52.5 (87)
1508	54.5 (84)	66.3 (69)	61.9 (78)	69.7 (74)	59.9 (78)	54.1 (86)
2250	63.6 (73)	65.4 (71)	53.9 (86)	47.2 (99)	50.5 (93)	51.0 (92)
3000	82.0 (56)	75.5 (62)	67.9 (70)	56.7 (82)	56.3 (83)	50.7 (91)
E2						
0	29.8 (155)	32.4 (143)	29.4 (164)	29.4 (157)	31.8 (149)	29.6 (157)
144	42.2 (112)	32.2 (148)	31.8 (145)	37.2 (125)	31.3 (148)	37.0 (130)
380	48.6 (96)	39.0 (117)	36.2 (128)	40.6 (113)	36.8 (124)	38.9 (118)
764	52.5 (88)	44.2 (106)	39.6 (117)	40.4 (114)	34.8 (132)	34.9 (132)
1508	75.3 (61)	62.6 (76)	42.3 (109)	42.4 (110)	42.1 (112)	40.5 (115)
2250	65.0 (71)	58.1 (80)	44.5 (104)	45.5 (101)	50.5 (93)	46.8 (101)
3000	73.0 (64)	61.4 (77)	51.0 (91)	49.2 (97)	51.4 (90)	47.8 (98)

grains within 150 μm of the surface in the ZR alloy was approximately 100-110 μm, while grains near the center were nearer to 50 μm in diameter. The D2 alloy, on the other hand, had an average grain size of only 80-85 μm in the region within 150 μm of the surface. The effect of temperature is summarized in Fig. 12 for specimens annealed for 3000-h; the solid horizontal line represents the initial grain size in the LT direction. The data for the two alloys at 1230 and 1280°C are almost identical, while the data for the 1330°C anneal indicate that the NSGs of the ZR alloy continue to grow, but the growth of NSGs in the D2 alloy has slowed.

Table IX. Average Grain Size as a Function Depth Below the Surface of the Specimen for Old-and New-process DOP-26 Exposed to an Oxygen Partial Pressure of 1.3 mPa at 1330°C

Length of Anneal (h)	Depth below surface (μm)					
	50	100	150	200	250	300
ZR						
0	36.5 (129)	28.6 (162)	29.1 (161)	28.5 (161)	25.0 (191)	28.5 (80)
167	44.3 (105)	44.4 (103)	38.1 (122)	35.9 (128)	31.6 (145)	31.7 (72)
335	60.8 (76)	42.6 (109)	48.6 (96)	44.0 (105)	37.0 (125)	32.4 (72)
756	77.0 (62)	57.2 (81)	49.3 (94)	52.9 (88)	41.7 (111)	39.8 (58)
1522	94.1 (51)	86.0 (54)	61.3 (76)	53.4 (89)	51.6 (95)	36.9 (64)
2282	87.4 (54)	107.0 (46)	64.8 (74)	61.5 (79)	71.0 (65)	58.3 (40)
3000	98.0 (50)	112.3 (43)	83.7 (55)	64.8 (73)	60.0 (77)	51.0 (94)
D2						
0	35.1 (134)	41.6 (111)	33.1 (139)	36.4 (127)	35.7 (130)	38.4 (122)
167	50.8 (91)	39.8 (115)	44.7 (107)	45.2 (102)	46.6 (99)	48.0 (98)
335	55.5 (83)	48.1 (99)	46.9 (98)	46.1 (101)	44.3 (104)	45.2 (104)
756	58.0 (81)	53.9 (85)	49.4 (93)	50.6 (91)	54.2 (86)	54.1 (87)
1522	73.7 (63)	78.8 (58)	57.2 (81)	57.1 (80)	49.3 (95)	51.6 (89)
2282	77.4 (59)	78.1 (60)	78.7 (58)	71.6 (64)	90.7 (53)	67.1 (71)
3000	76.0 (63)	81.4 (55)	78.6 (45)	67.1 (75)	62.5 (73)	62.5 (76)
E2						
0	51.5 (71)	49.6 (71)	55.2 (64)	45.1 (77)	49.0 (70)	44.9 (82)
167	63.1 (72)	55.7 (82)	60.6 (75)	57.0 (81)	62.9 (73)	56.8 (81)
335	83.7 (56)	70.3 (69)	60.1 (78)	59.4 (78)	63.4 (72)	77.6 (60)
756	80.8 (59)	71.9 (64)	67.2 (70)	70.4 (65)	66.6 (69)	66.8 (69)
1522	79.6 (57)	80.5 (56)	67.2 (67)	62.3 (71)	67.2 (68)	65.6 (68)
2282	98.2 (49)	99.3 (47)	112.0 (50)	118.8 (68)	76.1 (55)	67.6 (58)
3000	79.9 (47)	101.6 (47)	92.4 (41)	69.6 (40)	83.2 (64)	78.7 (70)

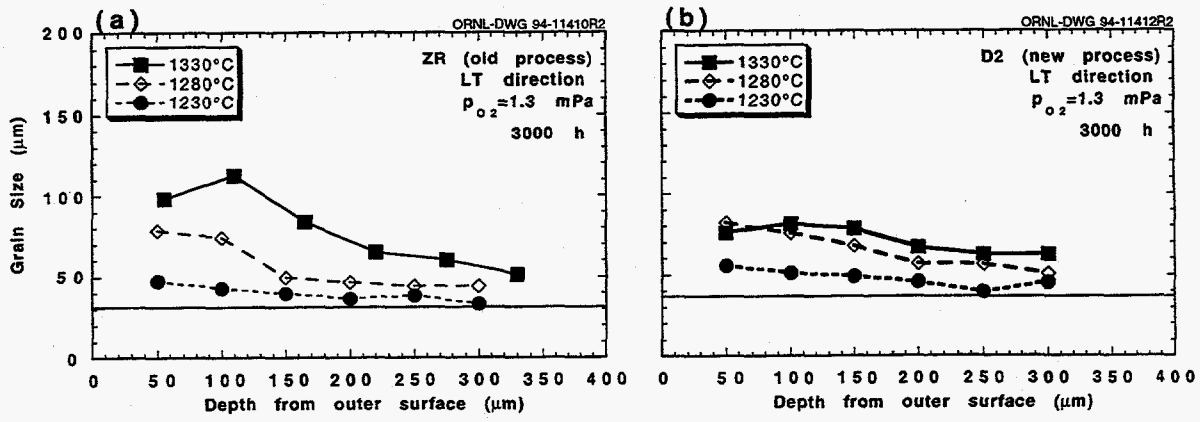

Fig. 12. Comparison of grain size versus distance from the surface for the (a) ZR and (b) D2 alloys exposed for 3000 h to 1.3 mPa oxygen at 1230, 1280, and 1330°C. The grain size for an unannealed specimen is included as a solid horizontal line.

Low-pressure Oxygen Annealing -- 13.3 mPa Oxygen

Oxygen anneals of the ZR, D2, and E2 materials have also been completed at an oxygen partial pressure of 13.3 mPa (10^{-4} torr) at 1330°C for times up to 3000 h (4 months). A summary of the average grain sizes measured in both the short transverse (ST) and long transverse (LT) directions with respect to the rolling direction is presented in Table X and Fig. 13. The optical microstructure of the ZR material after 3000 h of exposure at these annealing conditions is shown in Fig. 14 and should be compared to the as-recrystallized condition shown in Fig. 9(a). In the ST direction, the old-process ZR material had an average initial grain size of approximately 15 μm, while the new-process materials (D2 and E2) had grain sizes of approximately 22-26 μm. These initial grain sizes are comparable to those reported above for the results of the 1.3 mPa oxygen anneal. After 3000 h of exposure to 13.3 mPa of oxygen, the DOP-26 materials had grain sizes of 47-58 μm. All three materials had grains elongated in the LT direction (see Table X). The ZR material started at about 27 μm in the LT direction and grew to 73 μm, while the new process D2 and E2 materials grew from about 24-26 μm to 47-51 μm. As shown by the data in Fig. 13, the three DOP-26 materials used in this study had approximately the same grain growth characteristics under these oxygen annealing conditions (i.e., all of the data in Fig. 13 are considered to be within the range of experimental errors for these measurements).

Figure 15 compares the current results for the three DOP-26 materials exposed to 13.3 mPa oxygen with the data reported above for oxygen anneals at the same tempera-

Table X. Average Grain Size as a Function of Exposure at 1330°C in an Oxygen Partial Pressure of 13.3 mPa

Exposure Time (h)	Average grain size (μm)[a]					
	ZR (ST)	ZR (LT)	D2 (ST)	D2 (LT)	E2 (ST)	E2 (LT)
0	15.2 (937)	26.8 (1046)	24.1 (597)	40.0 (698)	26.3 (547)	44.7 (622)
170 (1 week)	27.6 (518)	38.6 (718)	35.3 (408)	55.8 (498)	36.1 (399)	52.3 (540)
720 (1 mon.)	41.4 (347)	54.2 (518)	40.1 (362)	58.4 (482)	40.8 (355)	62.2 (446)
3000 (4 mon.)	57.6 (251)	72.9 (416)	46.7 (280)	65.5 (439)	50.6 (292)	71.9 (396)

[a]ST = short transverse, LT = long transverse direction with respect to the rolling direction.

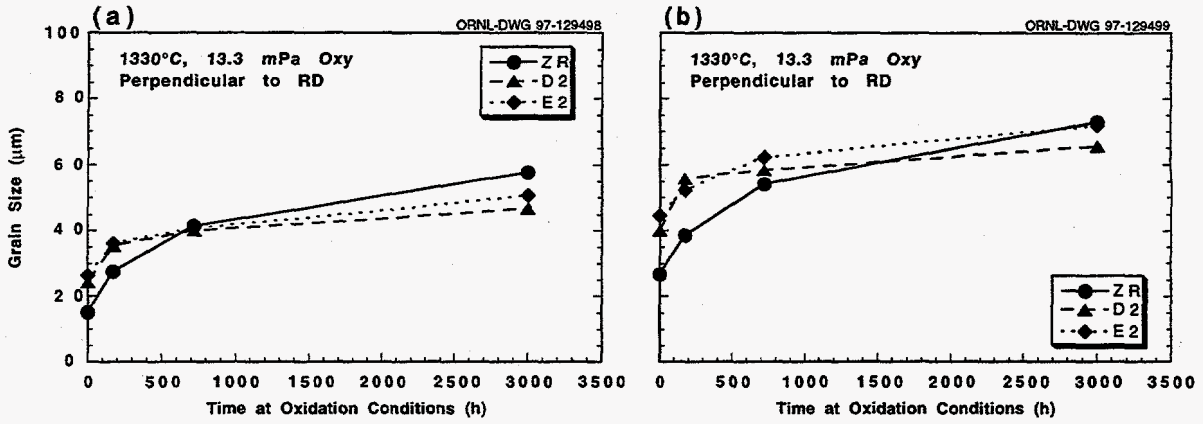

Fig. 13. Grain size as a function of time of exposure at 1330°C and 13.3 mPa oxygen partial pressure for old-process ZR and new-process D2 and E2 iridium alloys in the (a) ST and (b) LT directions with respect to the rolling direction.

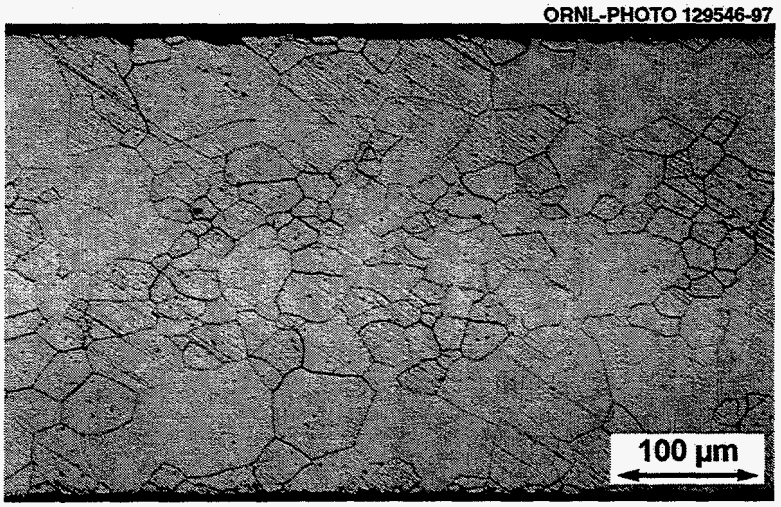

Fig. 14. Optical micrograph showing grain size and microstructure of the ZR material (old-process DOP-26) after oxygen annealing at 1330°C and 13.3 mPa oxygen for 3000 h.

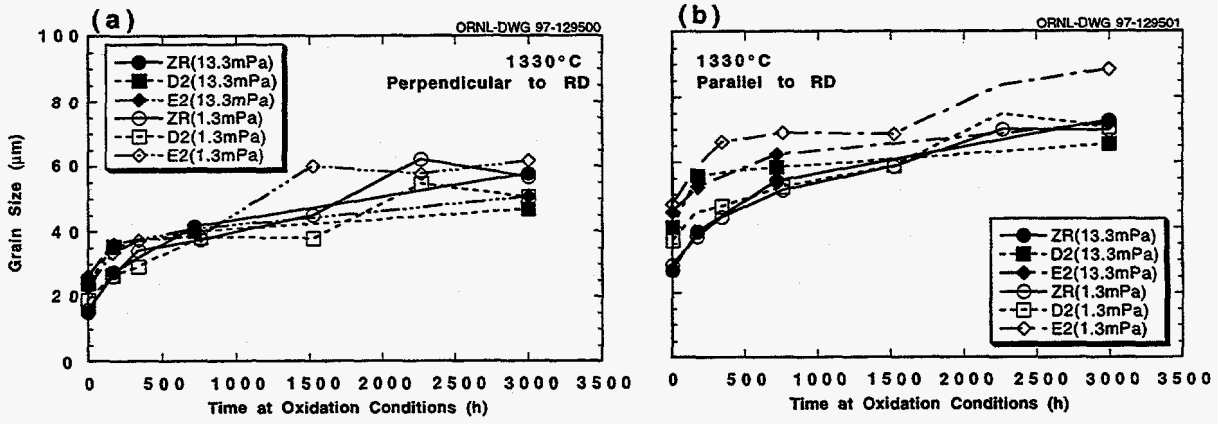

Fig. 15. Comparison of grain growth for the ZR, D2, and E2 DOP-26 materials exposed at 1330°C to an oxygen partial pressure of 13.3 mPa with earlier data at 1.3 mPa: (a) ST direction, (b) LT direction.

ture but at a lower oxygen partial pressure of 1.3 mPa (10^{-5} torr). The grain-growth rates in both the ST and LT directions are about the same for the 13.3 mPa and 1.3 mPa levels of oxygen. However, the average grain sizes for some of the exposure times are slightly lower after the 13.3 mPa oxygen exposure than for the 1.3 mPa oxygen level. This phenomenon is more evident in the plots of average grain size versus depth into the specimen. As shown in Fig. 15, the as-recrystallized grain sizes (at 0 time) of the specimens used in the 13.3 and 1.3 mPa oxygen tests were about the same, indicating that the techniques that were used to measure grain sizes were comparable for the two series of tests. However, in all three DOP-26 materials, the grain sizes of specimens exposed to the higher 13.3 mPa level of oxygen were slightly lower at all distances below the surface of the sample than the specimens exposed previously to 1.3 mPa of oxygen (see Figs. 16 18). These results indicate that the thermodynamics or kinetics of oxygen and thorium diffusion may be different for the two oxgyen levels at this temperature (1330°C).

In general, the tendency for anomalous grain growth at the surface that has been observed for DOP-26 materials in past oxygen-compatibility tests was also observed in the three materials tested at the 13.3 mPa oxygen level (see Table XI and Figs. 16-18). This tendency was the most obvious in data from the old-process E2 (Fig. 18) specimens.

Table XI. Average Grain Size as a Function Depth Below the Surface of the Specimen for Exposures to an Oxygen Partial Pressure of 13.3 mPa at 1330°C

Alloy	Exposure Time (h)	Depth below surface (μm)					
		50	100	150	200	250	300
ZR	0	26.0 (177)	25.6 (179)	27.7 (166)	28.8 (170)	24.9 (187)	28.1 (167)
	170	45.3 (101)	39.4 (117)	37.6 (122)	36.0 (127)	38.7 (118)	35.0 (133)
	720	67.6 (70)	56.0 (82)	52.8 (87)	49.3 (94)	50.1 (93)	49.7 (92)
	3000	89.0 (52)	101.7 (46)	89.8 (51)	58.4 (79)	50.6 (92)	47.7 (96)
D2	0	44.4 (108)	43.0 (106)	38.7 (120)	39.2 (118)	34.6 (132)	40.3 (114)
	170	57.2 (80)	62.5 (75)	54.0 (85)	54.4 (85)	56.5 (81)	50.2 (92)
	720	70.5 (65)	67.3 (68)	58.2 (79)	58.2 (79)	48.5 (95)	47.9 (96)
	3000	63.5 (73)	74.6 (65)	85.7 (55)	61.4 (76)	57.4 (80)	50.9 (90)
E2	0	40.8 (112)	43.2 (106)	50.6 (92)	46.9 (100)	45.1 (102)	41.5 (110)
	170	59.2 (80)	52.1 (89)	48.7 (94)	49.5 (93)	49.0 (97)	55.5 (87)
	720	70.4 (66)	60.8 (75)	57.9 (79)	60.2 (76)	59.8 (78)	64.1 (72)
	3000	75.5 (61)	79.7 (59)	89.0 (52)	67.7 (69)	60.4 (76)	58.8 (79)

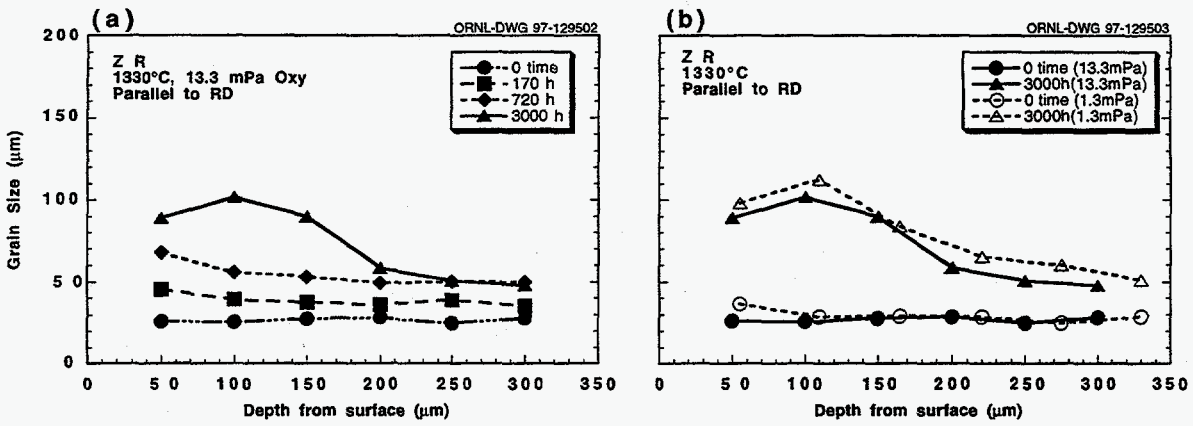

Fig. 16. Grain growth in the LT direction as a function of depth below the surface of the sample for ZR material oxygen annealed at 1330°C and an oxygen partial pressure of 13.3 mPa: (a) 0, 170, 720, and 3000 h; (b) 0 and 3000 h only compared to data from the earlier test at 1.3 mPa oxygen.

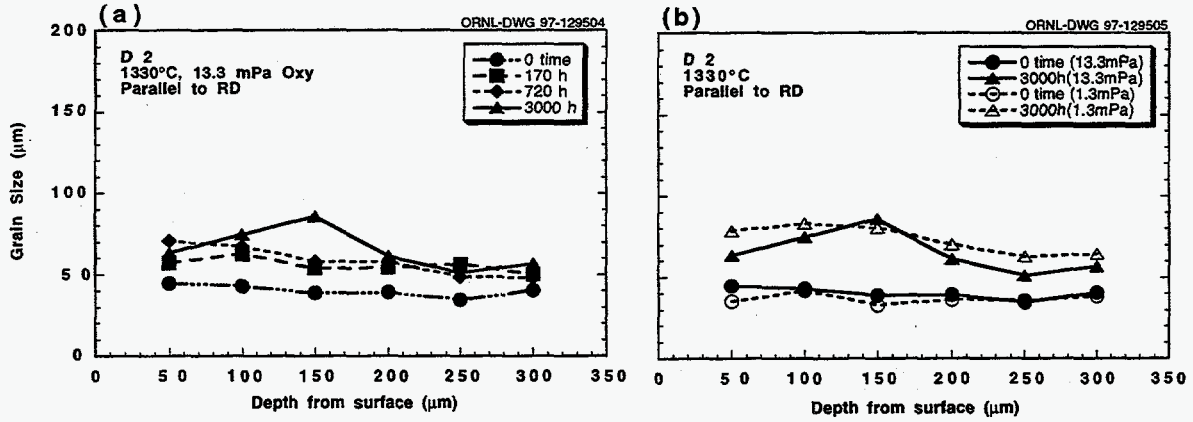

Fig. 17. Grain growth in the LT direction as a function of depth below the surface of the sample for D2 material oxygen annealed at 1330°C and an oxygen partial pressure of 13.3 mPa: (a) 0, 170, 720, and 3000 h; (b) 0 and 3000 h only compared to data from the earlier test at 1.3 mPa oxygen.

Auger Electron Spectroscopy (AES)

Auger electron spectroscopy was performed on the ZR and D2 materials after exposure to an oxygen partial pressure of 1.3 mPa for 3000 h, and the results were compared to specimens receiving no oxygen anneal [16]. The strongest Auger peak for thorium is at 65 eV, followed by peaks at 245 and 228 eV. However, because the two

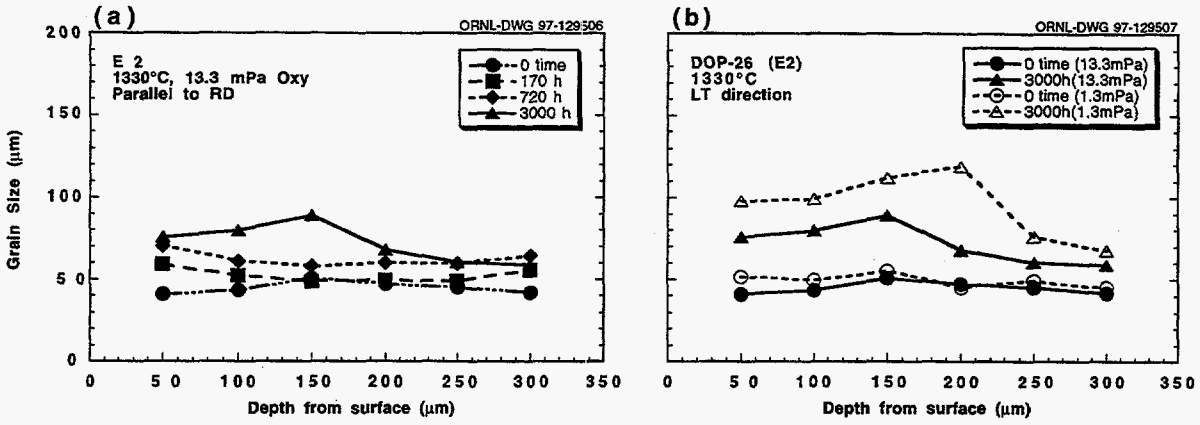

Fig. 18. Grain growth in the LT direction as a function of depth below the surface of the sample for E2 material oxygen annealed at 1330°C and an oxygen partial pressure of 13.3 mPa: (a) 0, 170, 720, and 3000 h; (b) 0 and 3000 h only compared to data from the earlier test at 1.3 mPa oxygen.

higher energy peaks overlap with the 244 and 229 eV iridium peaks, only the 65 eV peak for thorium was used for the analyses in this study. The closest iridium peak used for normalization is at 54 eV.

0-h oxygen anneal - Figure 19 shows a typical Auger fracture surface of an old-process DOP-26 sample (ZR alloy) annealed for 1 h at 1375°C with no oxygen exposure on which Auger analysis was carried out. This fractograph is representative of the fracture mode for both the new- and old-process specimens. Both alloys fractured predominantly by intergranular failure but contained some transgranular facets, allowing for analysis of both the bulk (transgranular surfaces) and grain boundary concentrations of thorium.

A typical Auger spectrum obtained from a transgranular fracture region of a new process D2 sample, along with a partial spectrum from an intergranular fracture region (a grain boundary) on the same sample (inset), is shown in Fig. 20. The small peak at approximately 65 eV in the inset indicates that thorium is present on the grain boundary. Figure 21 shows Auger spectra obtained at ≈8 μm intervals on the intergranular surface of a single NSG, from the surface towards the center of the sample. The height of the thorium peaks remained almost constant at each depth on that NSG, showing that thorium concentration is quite uniform over a given grain boundary in the D2 material with no oxygen anneal. Figure 22 is a plot of the thorium concentration (measured on different grain boundaries) as a function of depth from the free surface for new-process DOP-26

ORNL-PHOTO 129547-97

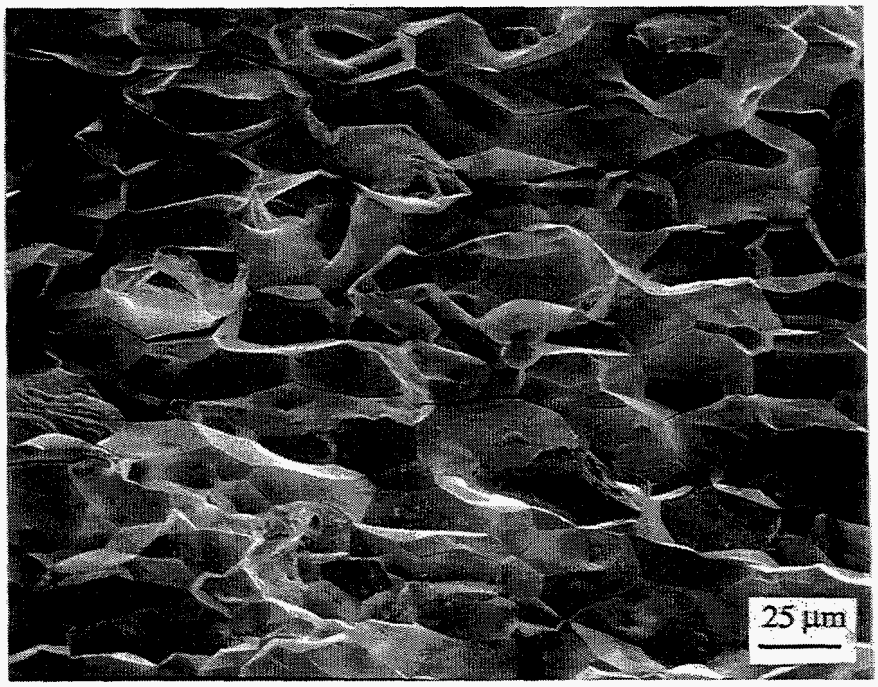

Fig. 19. Auger fracture surface of an old-process DOP-26 (ZR) specimen annealed for 1 h at 1375°C with no oxygen exposure.

ORNL-DWG 95-6145

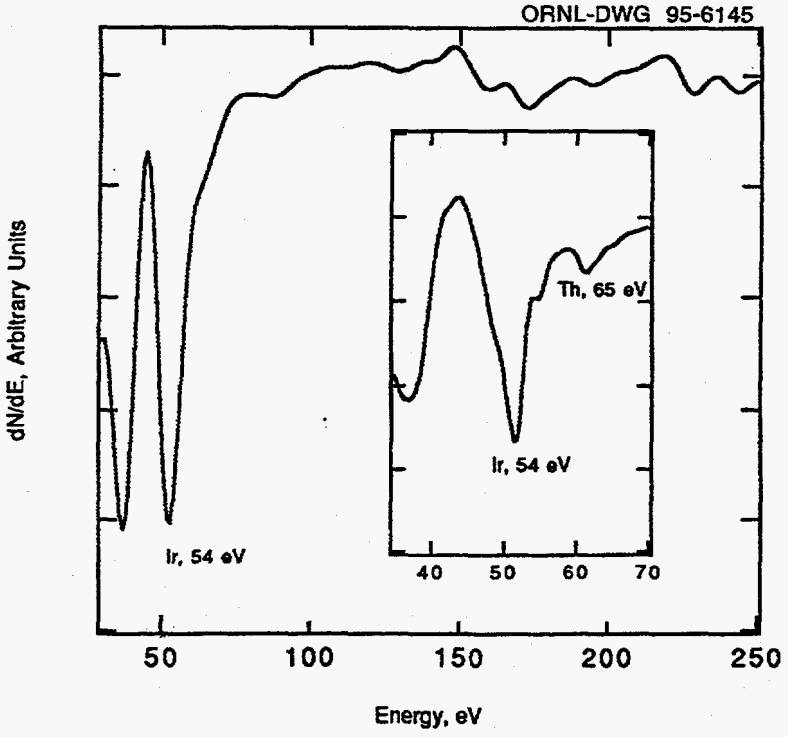

Fig. 20. Auger spectra from transgranular and intergranular (inset) fracture regions of a new-process DOP-26 (D2) specimen with no oxygen exposure.

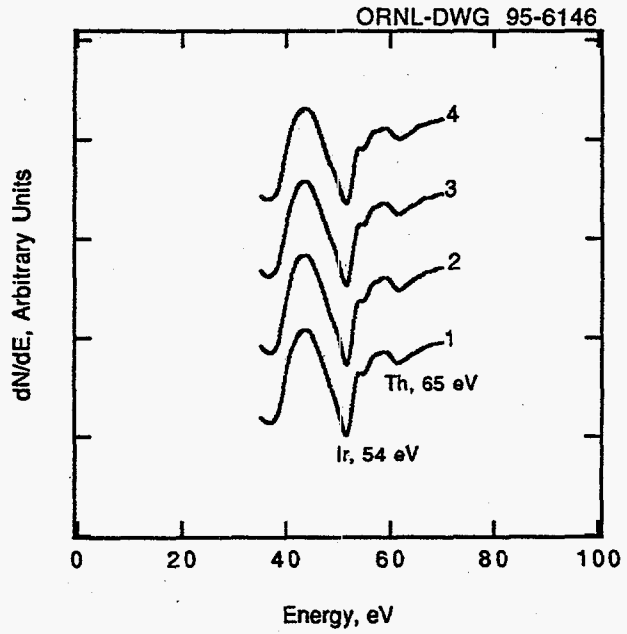

Fig. 21. Auger spectra from four points along a line within a near-surface grain (NSG) of the specimen shown in Fig. 19; points were 8 μm apart.

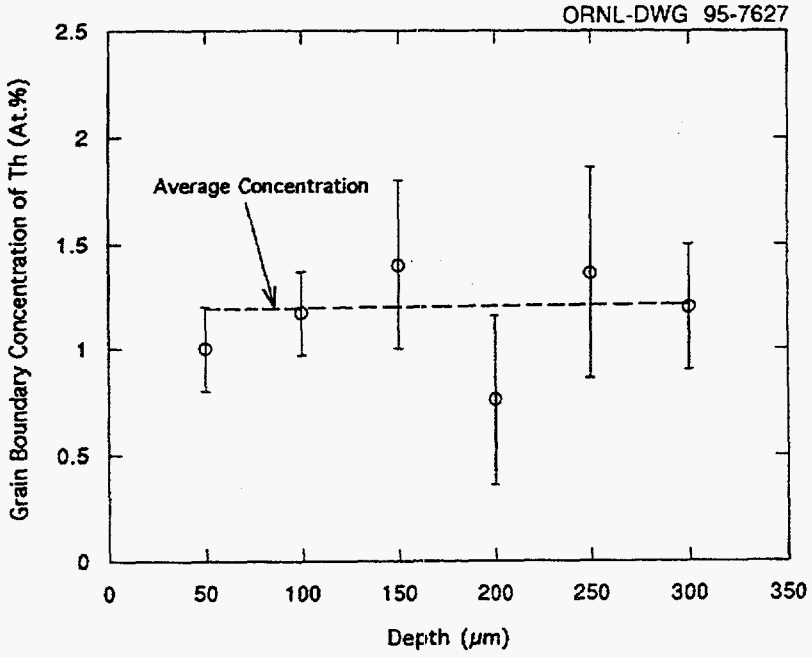

Fig. 22. Grain boundary thorium concentration as a function of depth from the surface for a new-process DOP-26 (D2) specimen with no oxygen exposure.

(D2 material). Within experimental scatter, the thorium concentration remained a constant at different depths. Therefore, an average thorium concentration was obtained by averaging the thorium peak height for different grain boundaries (more than 25 in number) over the entire sample.

A similar analysis was conducted on the specimen of the old-process DOP-26 (ZR material) shown in Fig. 19. Spectra from a transgranular and an intergranular (inset) region (Fig. 23) show that the grain boundaries of the ZR material were also enriched with thorium. The average grain boundary concentration of thorium in the new- and old-process DOP-26 was determined to be 1.7±0.5 and 2.0±0.4 at.%, respectively, prior to oxygen annealing.

3000-h oxygen anneal - Figure 24 shows the fracture surface (on which Auger analysis was carried out) of a new-process DOP-26 sample (D2 material) which was subjected to a 3000-h oxygen anneal at 1330°C. Figure 25 shows Auger peaks of thorium and iridium on one NSG boundary at intervals of ≈10 μm from the surface towards the

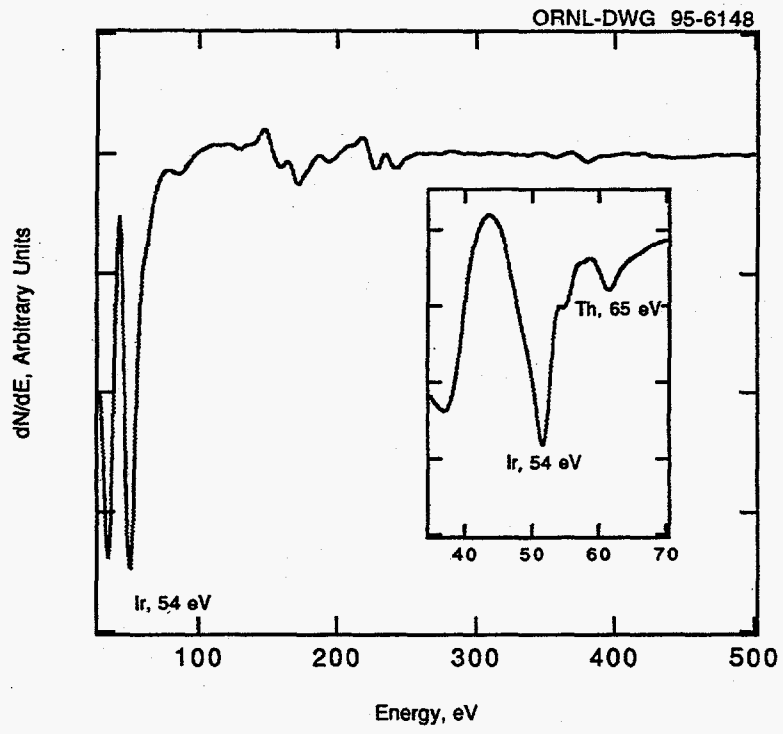

Fig. 23. Auger spectra from transgranular and intergranular (inset) fracture regions of an old-process DOP-26 (ZR) specimen with no oxygen exposure.

ORNL-PHOTO 129548-97

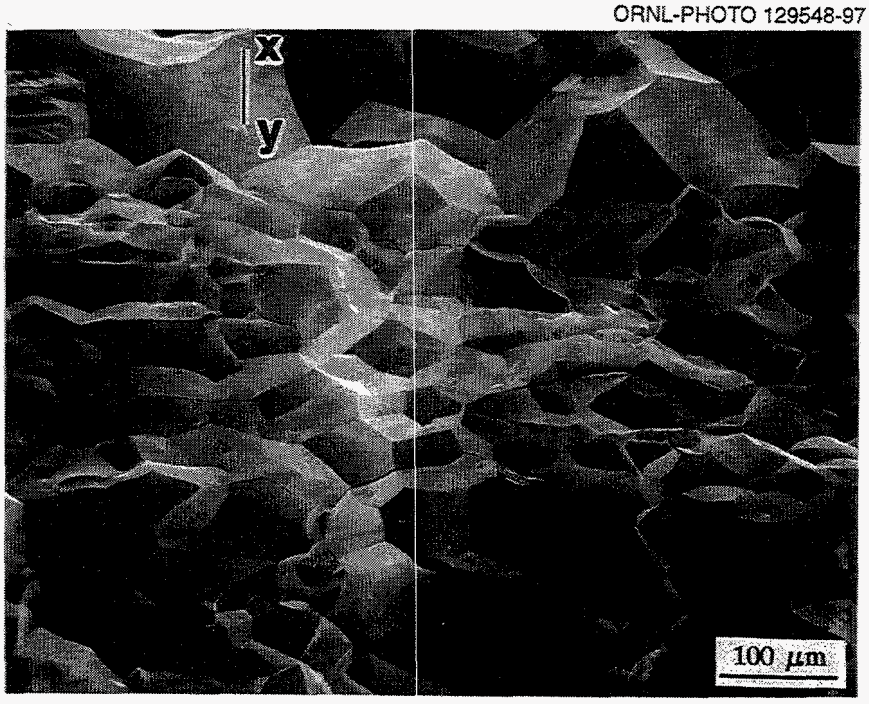

Fig. 24. Auger fracture surface of a DOP-26 (D2) specimen after a 3000-h oxygen anneal at 1330°C.

ORNL-DWG 95-7626

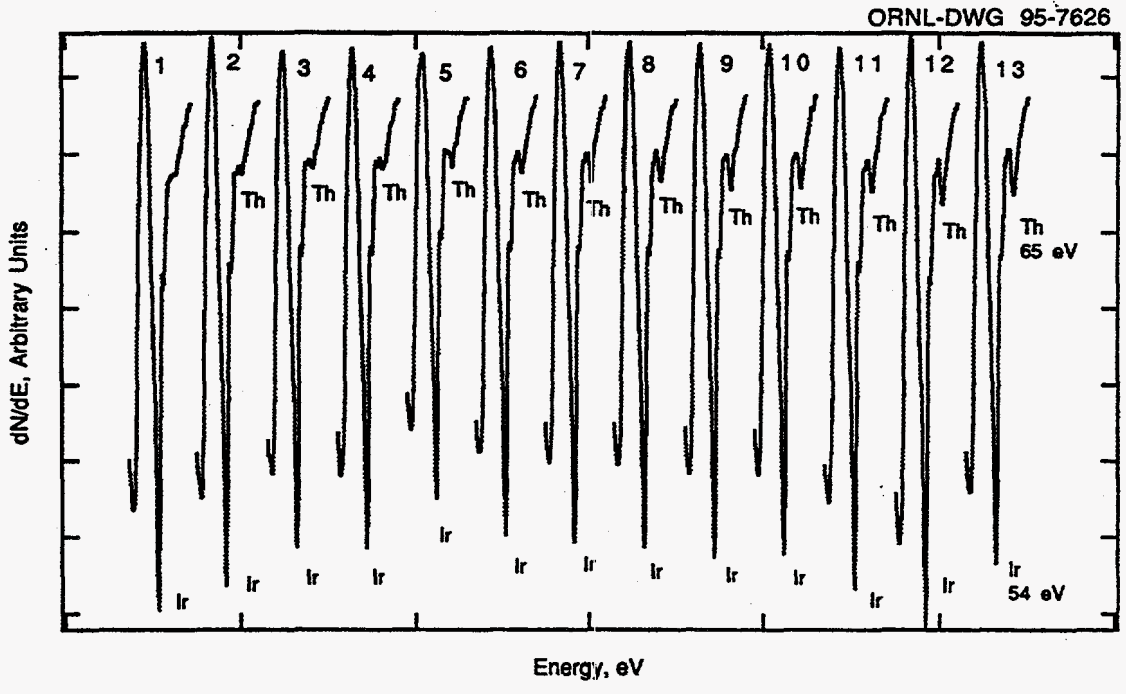

Fig. 25. Auger spectra from 13 points along line XY of Fig. 24; points were approximately 10 μm apart and on the same near-surface grain (NSG).

center along line XY shown in Fig. 24. From Fig. 25, it is clear that there is a depletion of thorium near the surface and that there is an increase in the thorium concentration with depth from the free surface. The average grain boundary concentration of thorium as a function of depth was determined from Auger spectra obtained from grain boundaries at intervals of 50 μm depth from the free surface towards the center of the sample and the data are plotted in Fig. 26. It is clear that there is a drop in thorium concentration as one moves from the interior to the surface, and that for distances within 50 μm of the surface the thorium concentration is below the detection limit of AES (≈0.5 at.%). Figure 27 shows a typical fracture surface from a specimen of old-process DOP-26 (ZR material) after a 3000-h oxygen anneal at 1330°C. Similar to the new-process DOP-26, the old-process DOP-26 exhibits a drop in grain boundary thorium level from the interior to the surface (see Fig. 26). Here also thorium was not detected on grain boundaries to a depth of nearly 50 μm from the surface.

The same procedures were used to determine the thorium concentration as a function of depth below the free surface in the old-process ZR and new-process D2 materials after oxygen-annealing at 1330°C in an oxygen partial pressure of 13.3 mPa. Again the results, shown in Fig. 28, indicate that the thorium level drops off significantly from the interior to the surface and was below the detectable limit on grain boundaries of within 50 μm of the surface. Within experimental error, the data for the 1.3 mPa anneal and the 13.3

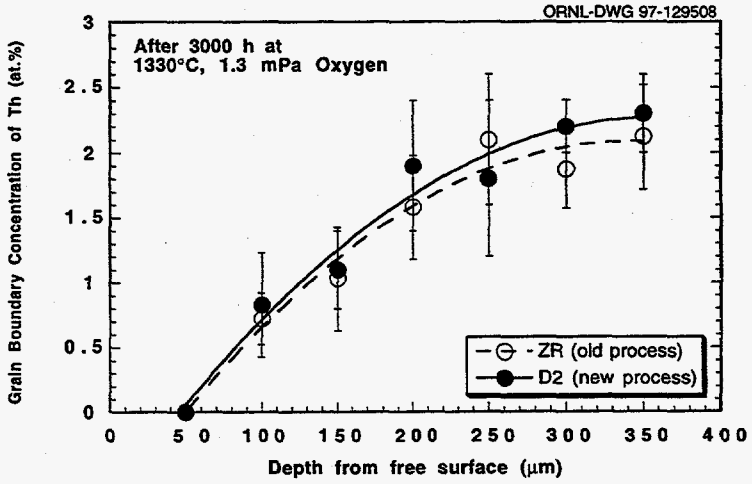

Fig. 26. Thorium concentration as a function of depth from the surface for DOP-26 specimens annealed for 3000 h at 1330°C in an oxygen partial pressure of 1.3 mPa.

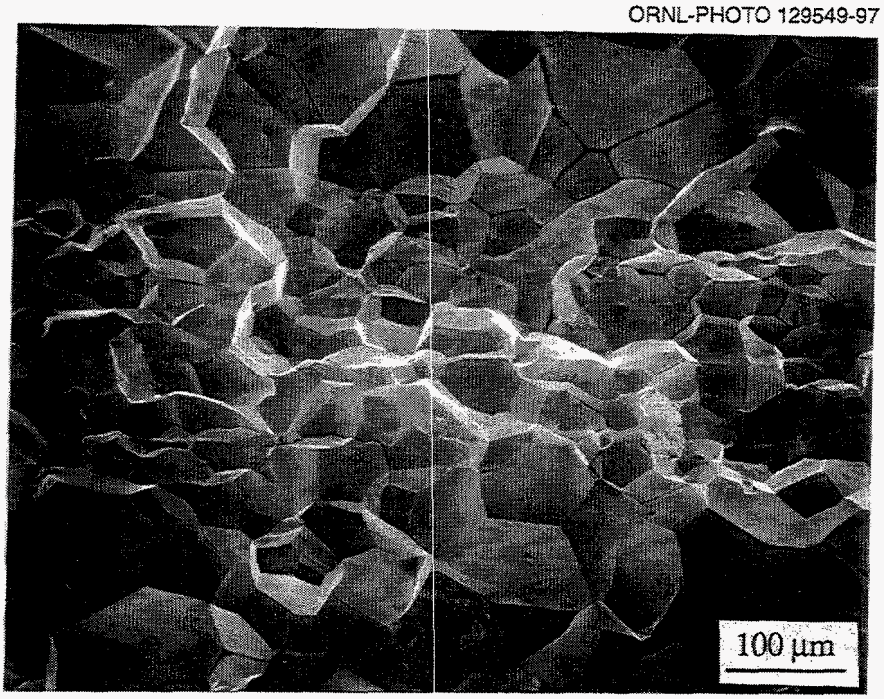

Fig. 27. Auger fracture surface of an old-process DOP-26 (ZR) specimen after a 3000-h oxygen anneal at 1330°C.

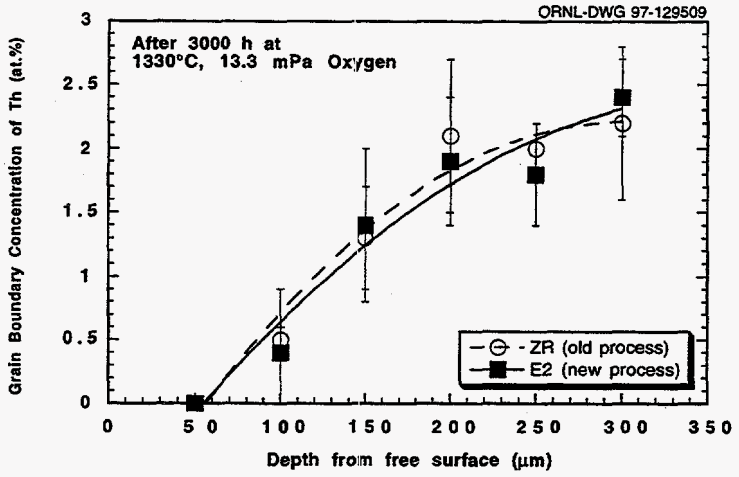

Fig. 28. Thorium concentration as a function of depth from the surface for DOP-26 specimens annealed for 3000-h at 1330°C in an oxygen partial pressure of 13.3 mPa.

mPa anneal showed no significant difference in thorium concentration as a function of depth from the surface (see Fig. 29).

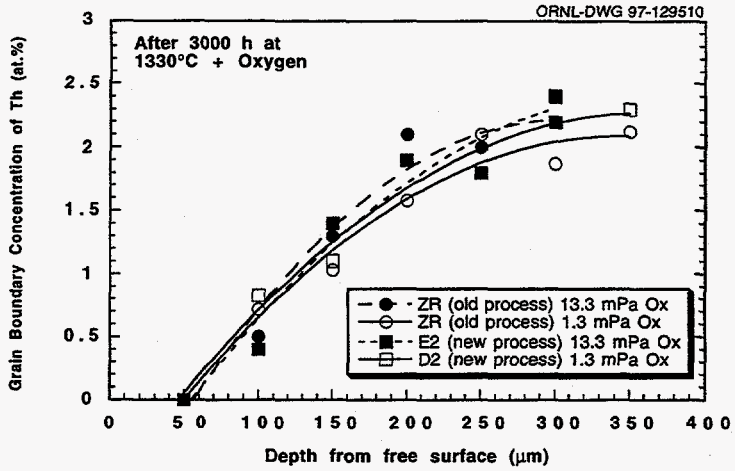

Fig. 29. A comparison of thorium concentration as a function of depth from the surface for old- and new-process DOP-26 specimens after 3000-h oxygen anneals at 1330°C.

Discussion

In an earlier study by White and Liu [11] in which samples of DOP-26 were annealed in low pressure oxygen (1.3 mPa) for up to 3000 h, anomalous grain growth of NSGs, similar to that observed in the present study, was seen. The explanation put forward in the earlier study for the anomalous grain growth involved dissolution of Ir_5Th precipitates (thereby unpinning the grain boundaries) and diffusion of thorium along the grain boundaries to the surface where it formed oxides. Auger analyses on one NSG in that study indicated a continuous increase in thorium concentration from the outer edge towards the center of the sample. Also, surface analysis indicated the presence of some discrete ThO_2 particles. It was shown that the dissolution of Ir_5Th particles, diffusion of thorium along grain boundaries to the surface, and oxidation of thorium to form discrete ThO_2 precipitates at the surface were thermodynamically favorable. This process resulted in the unpinning of grain boundaries and the exaggerated grain growth of NSGs. The present study was undertaken as an expansion of the earlier results.

Due to the complex mechanism of grain growth identified in these alloys, involving the dissolution of the Ir_5Th precipitates and the diffusion of thorium along grain boundaries to the surface, grain growth in these materials can not be described in terms of normal precipitate effects as proposed by Zener [25], Hillert [26], and Gladman [27]. There is also

no evidence for precipitate coarsening in this system which could lead to abnormal grain growth as described by Gawne and Higgins [28] for iron containing a dispersion of Fe_3C precipitates or by Petrovic and Ebert [29] for nickel alloys containing fine dispersions of thoria. Therefore, in order to get a first-approximation estimate of the activation energies for grain growth, the data were fit to the standard grain-growth equation:

$$d^2 - d_o^2 = kt \qquad (1)$$

with

$$k = k_o \exp(-Q/RT) \qquad (2)$$

where d is the grain diameter at time t, R is the gas constant (8.317 joules/mole/°C), k_o is a constant, T is the absolute temperature, and Q is the activation energy for grain growth. For heat treatments in vacuum, d_o was taken as the grain diameter at t = 1 h; for heat treatments in low-pressure oxygen, d_o was taken as the grain diameter after the recrystallization anneal at 1375°C.

Using equation (1) the change in grain size with time at each temperature was determined for the heat treatments in vacuum and in the 1.3 mPa oxygen environment. The straight-line fit of the data at each temperature equals the grain-growth constant k. The activation energy for grain growth was determined by plotting k versus the temperature according to equation (2) and the results of these analyses are shown in Figs. 30 and 31 for grain growth in vacuum and in low-pressure oxygen, respectively. These results, along with the r^2 correlations (in parentheses) for the straight-line fit of the data, are presented in Table XII. In this way the activation energies for grain growth in the new-process D2 material were determined to be approximately 566 and 420 kJ/mole for heat treatments in vacuum and in low-pressure oxygen, respectively. For comparison purposes, Table XII also includes data previously determined for an alloy designated DOP-4 which contained only 30 wppm Th [8,9,13] and for the DOP-26 ZR material fabricated by the old process [5]. The present data are comparable to the previous data; activation energies for specimens heat treated in vacuum range from 518 to 611 kJ/mole, while those for oxygen annealed specimens are 355-420 kJ/mole.

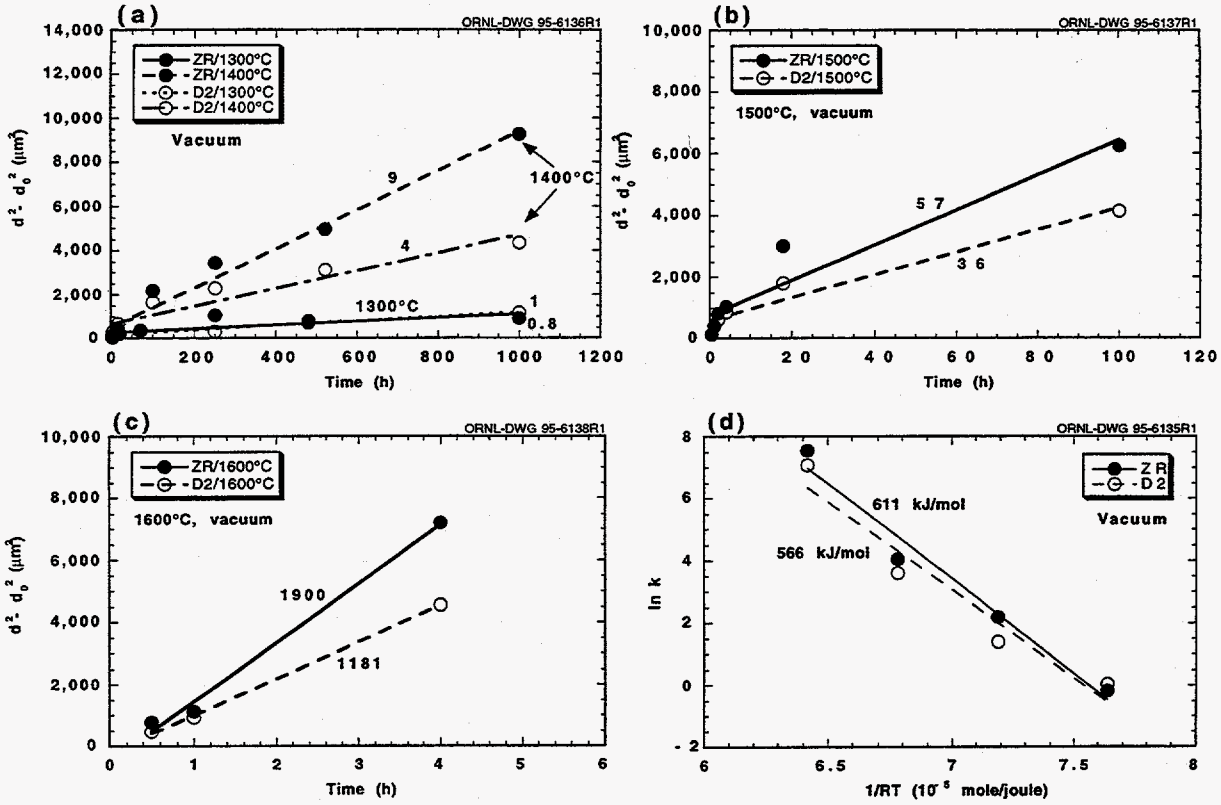

Fig. 30. Determination of the grain-growth constant k for ZR and D2 DOP-26 alloys heat treated in vacuum at temperatures of (a) 1300 and 1400°C, (b) 1500°C, and (c) 1600°C, and (d) the corresponding activation energy for grain growth Q.

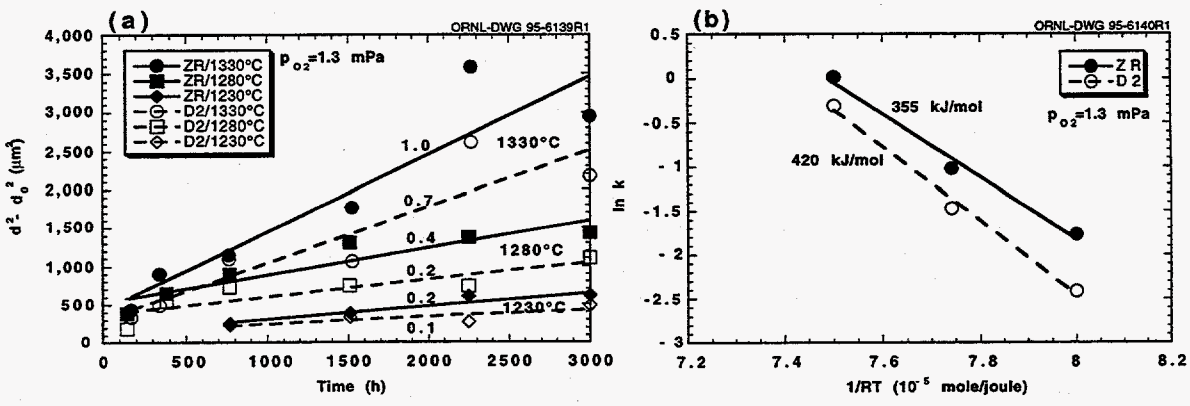

Fig. 31. Determination of (a) the grain-growth constant k and (b) the activation energy Q for grain growth of the ZR and D2 DOP-26 iridium alloys heat treated in a low-pressure (1.3 mPa) oxygen atmosphere.

Table XII. Least Squares Calculated Values of k and Q for DOP-26 Iridium Alloys[a]

Alloy	k ($\mu m^2/h$)				Q (kJ/mole)
Vacuum	1300°C	1400°C	1500°C	1600°C	
ZR	0.8 (0.55)	9 (0.98)	57 (0.92)	1901 (0.99)	611 (0.97)
D2 [Ref. 16]	1.0 (0.94)	4 (0.90)	36 (0.94)	1181 (1.0)	566 (0.94)
	1310°C	1415°C	1530°C		
DOP-4[b]	1.1	17.1	130		518±46
1.3 mPa Oxygen	1230°C	1280°C	1330°C		
ZR	0.2 (0.91)	0.4 (0.85)	1.0 (0.85)		355 (0.99)
D2 [Ref. 16]	0.1 (0.64)	0.2 (0.75)	0.7 (0.83)		420 (0.99)

[a]Number in parentheses is the r^2 correlation factor for the straight-line fit of the data.
[b]This Ir-0.3 wt% W alloy contains only 30 wppm Th [Refs. 8,9,13].

An important observation that can be made from this data is that the activation energy for grain growth in vacuum is higher than that for grain growth in low-pressure (1.3 mPa) oxygen. This is not surprising as grain boundary mobility is less in vacuum due to pinning of grain boundaries by Ir_5Th precipitates. On the other hand, in the low-pressure oxygen atmosphere, there is diffusion of thorium to the surface coupled with Ir_5Th precipitate dissolution. This causes unpinning of the grain boundaries, which results in much higher mobility and higher grain growth rates. Even though the comparison of the absolute values of activation energies does not give the phenomenological explanation for observed abnormal grain growth of NSGs, it does point out a marked difference between the kinetics of grain growth observed in the vacuum and low-pressure oxygen atmospheres used in this study. This difference in activation energies is apparent even though, as White and Liu pointed out [11], the oxidation of thorium is probably thermodynamically favorable in both the atmospheres used in this study. (They calculated that, for iridium alloys with 60 wt ppm Th, ThO_2 is stable at partial oxygen pressures of greater than about 10^{-21} Pa.) It is not known what the partial pressure of oxygen was in the vacuum anneals used in the current tests (much less than 10^{-4} Pa), but the difference between it and the low-pressure oxygen atmosphere that was used was enough to measurably affect the activation energy.

Auger analyses on the 3000-h oxygen-annealed samples of both old-process ZR and new-process D2 DOP-26 materials showed an absence of thorium on grain boundaries located within 50 μm of the specimen surface. The grain growth data combined with

Auger analysis indicate that a mechanism of diffusion of thorium and dissolution of Ir_5Th precipitates similar to that put forward in the previous study [11] would explain the observed exaggerated grain growth of NSGs.

As there are no self- or solute-diffusion data available for iridium, one option is to get an estimate for the activation energy for diffusion by considering fcc metals in the same group of metals (Group VIII) to which iridium belongs. Platinum is an fcc metal in Group VIII and its activation energy for self-diffusion is 278.4 kJ/mole [30]. To get an approximate value of the activation energy for self-diffusion in iridium, one can scale up from platinum according to the melting point. But according to Porter and Easterling [30], for a given crystal structure and bond type, Q/RT_m is roughly constant where Q is the activation energy for self-diffusion in kJ/mole, R is the gas constant, and T_m is the melting point. For fcc metals, Q/RT_m ranges from 16 to 22 [30]. So using the midpoint value of 19, the activation energy for self-diffusion in iridium can be approximated as 430 kJ/mole, which can be taken as an upper limit. White and Liu [11] used similar reasoning to arrive at an activation energy of 419 kJ/mole. Liao [31] and Gubbi [32] used an activation energy of 270 kJ/mole, taken as an average value of the activation energies for Group VIII metals. The activation energies determined in the present study for the low-pressure oxygen atmosphere, in which Ir_5Th precipitates have dissolved and the thorium has diffused to the surface leaving only the Ir-0.3wt% W matrix, compare well with the activation energy for self diffusion in iridium calculated theoretically and with the value calculated by White and Liu [11].

Summary and Conclusions

The grain growth characteristics of new-process (D2 and E2) and old-process (ZR) DOP-26 iridium materials were compared for specimens annealed in a vacuum of approximately 0.7 mPa (5×10^{-6} torr) and also for specimens annealed in low-pressure oxygen environments containing partial oxygen pressures of approximately 1.3 mPa (10^{-5} torr) or 13.3 mPa (10^{-4} torr). Initially, the old-process ZR material had a fairly even distribution of Ir_5Th precipitates and a slightly smaller initial average grain size (16 μm), while the new-process materials had stringers of precipitates distributed throughout and a slightly larger average initial grain size (19 μm). Although the distribution of Ir_5Th particles was different

in materials produced by the two processes, the results of this study indicated that the grain growth behaviors of the two materials were not significantly different. Therefore, it is anticipated that both old- and new-process DOP-26 materials used should perform similarly in high-temperature impact testing and in the expected service environment.

Grain growth in vacuum was determined to be uniform and characteristic of alloys containing precipitates. However, heat treatment in the low-pressure oxygen atmosphere resulted in anomalous growth of the near-surface grains, especially for the 1280 and 1330°C temperatures used in this study. Auger analyses of the specimens annealed at 1330°C in oxygen partial pressures of 1.3 and 13.3 mPa indicated that thorium, which is added to this alloy for high-temperature strength, diffuses out of the specimen towards the surface. The grain-growth data and Auger results support the earlier mechanism proposed by White and Liu [11] to explain the anomalous grain growth in this system. According to that mechanism, even an oxygen partial pressure of 1.3 mPa provides enough driving force for dissolution of the Ir_5Th precipitates in DOP-26 and diffusion of thorium to the surface to form ThO_2. This results in the unpinning of grains and accelerated growth of grains near the surface of the specimen.

Using standard grain growth equations, the activation energies for grain growth in vacuum (566 and 611 kJ/mole-K for D2 and ZR materials, respectively) were found to be higher than for grain growth in low-pressure oxygen (420 and 355 kJ/mole-K for D2 and ZR, respectively), suggesting a marked difference between the kinetics of grain growth observed in the two environments. This difference was explained on the basis of grain boundary mobility in vacuum versus low-pressure oxygen. The grain boundary mobility is less in vacuum due to pinning by Ir_5Th precipitates. On the other hand, in the low pressure oxygen atmosphere, the unpinning of grain boundaries (due to diffusion of thorium to the surface coupled with Ir_5Th precipitate dissolution) results in much higher mobility and higher rates of grain growth.

Oxygen compatibility studies of the three DOP-26 alloys were also completed at an oxygen partial pressure of 13.3 mPa and a temperature of 1330°C for times up to 3000 h. The data suggest that the grain growth rate and average grain size as a function of time and of depth into the specimen may be slightly lower at this higher partial pressure of oxygen than was found for the earlier tests conducted at 1.3 mPa of oxygen. However, the Auger analysis indicated no significant difference in the thorium concentration at depths to

about 300 μm below the free surface for the 1.3 versus 13.3 mPa oxygen-annealed specimens. These results suggest the need for further testing at the higher oxygen level.

GRAIN GROWTH BEHAVIOR OF CASSINI CLAD VENT SET CUP MATERIAL

Results And Discussion

Table XIII and Figure 32 show the variation in grain size as a function of 1-h heat treatment at temperatures of 1200-1800°C for specimens taken from the top, bend, and center regions, respectively, of selected Cassini clad vent set cups. Data for specimens which were cut 0, 45, and 90° to the rolling direction (RD) are included in each plot. Also included in each plot is the grain growth data determined earlier [see Fig. 4(a)] for a

Table XIII. Grain Growth Data Versus Heat Treatment Temperature and Location in Vent Set Cup

Position	Temperature (°C)	Grain Size (μm)		
		0° to RD	45° to RD	90° to RD
Top	1200	30.7	31.2	25.5
	1300	20.6	23.3	23.1
	1400	24.1	24.3	26.0
	1500	28.3	29.7	27.4
	1600	52.4	29.9	44.0
	1700	108.5	86.5	94.7
	1800	134.8	106.0	108.5
Bend	1200	31.1	28.1	21.9
	1300	24.6	22.9	20.7
	1400	23.7	24.3	26.6
	1500	25.7	29.1	27.1
	1600	28.9	28.6	42.6
	1700	66.8	64.2	73.0
	1800	144.6	171.2	92.7
Center	1200	29.3	27.0	25.1
	1300	23.0	21.4	19.8
	1400	24.7	23.3	27.6
	1500	21.7	20.2	21.9
	1600	41.9	35.0	39.1
	1700	60.7	75.7	143.5
	1800	210.8	134.8	175.0

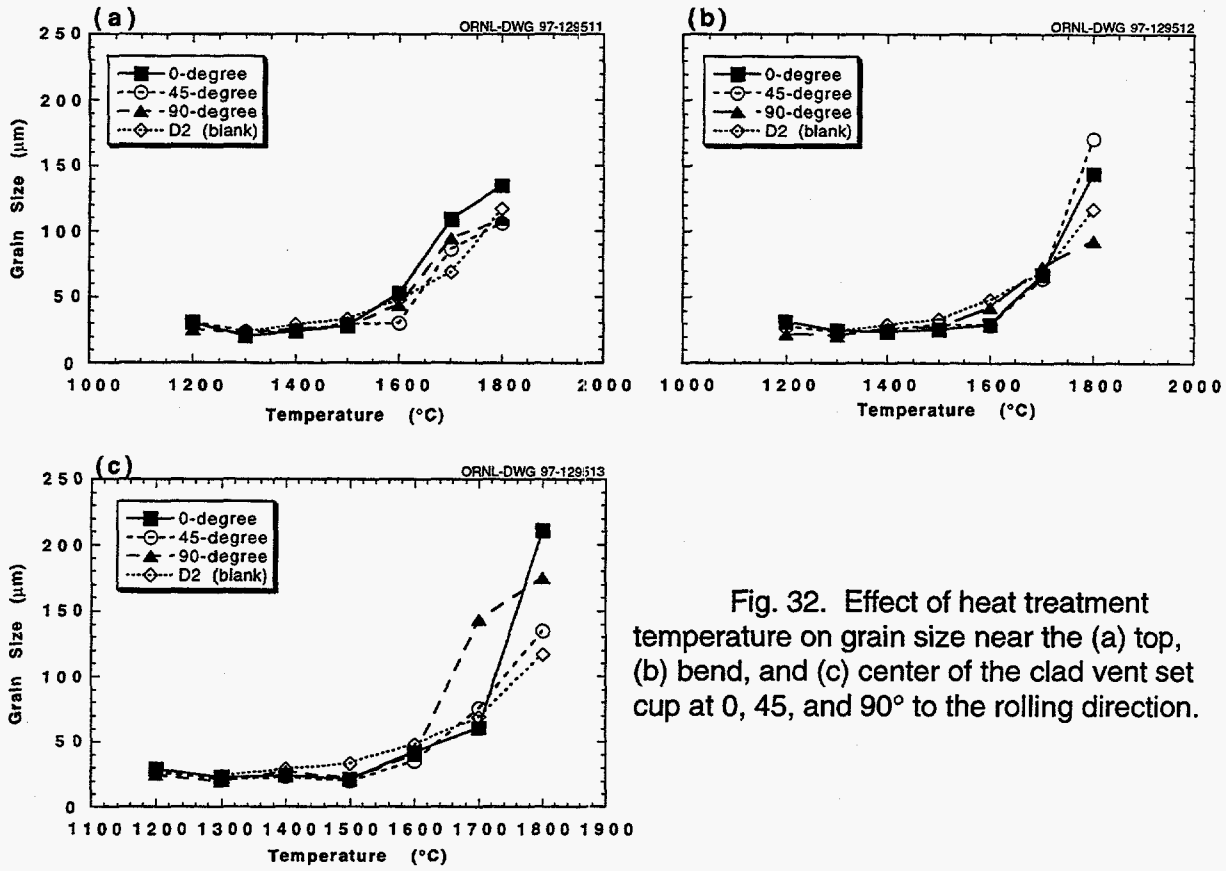

Fig. 32. Effect of heat treatment temperature on grain size near the (a) top, (b) bend, and (c) center of the clad vent set cup at 0, 45, and 90° to the rolling direction.

specimen taken from a blank fabricated from the D2 ingot of material. Within the expected experimental error of the grain-size data, no difference related to the position in the cups could be determined. Grain sizes of approximately 20-30 µm were maintained up to a heat treatment temperature of 1600°C, regardless of position in the cup. Above 1600°C, grain growth occurred to produce grain sizes on the order of 100-200 µm. A larger amount of scatter was observed in the data for heat treatment temperatures above 1600°C and was attributed to these larger grain sizes. Larger grains means that there are fewer grains through the thickness of the specimen for counting, and therefore statistically more scatter in the data. Likewise, no difference could be detected between the grain growth characteristics of the cups used for this study and the D2 blank (sheet) material which is typical of the sheet material from which the Cassini clad vent set cups were deep-drawn.

Table XIV and Figures 33-34 show the variation in grain size as a function of annealing time at 1400 and 1500°C for specimens taken from the top, bend, and center regions (refer to Fig. 3) of the cups. Figure 33 shows data at 1400°C, while Fig. 34 shows

Table XIV. Average Grain Size Versus Location in the Clad Vent Set Cup and Time of Heat Treatment at 1400 and 1500°C

Position	Temperature (°C)	Length of Anneal (h)	Grain Size (μm)		
			0° to RD	45° to RD	90° to RD
Top	1400	0		22.8	
		1	21	26	26
		18	32	31.2	30
		100	34	33	34
		520	52.5	55	48
	1500	0		20.7	
		1	28	27.8	25.8
		18	48	41	45
		100	77	71	81
		240	142	130	148
Bend	1400	0		20.2	
		1	24	24.3	25
		18	29.3	29.7	30
		100	33	34	33.2
		520	52	45	51
	1500	0		20.2	
		1	33	24	26
		18	41	46	50
		100	74	74	85
		240	136	148	132
Center	1400	0		23	
		1	24	25	27
		18	29.5	30.2	31
		100	32.5	33.2	35
		520	54.3	53	46
	1500	0		21.2	
		1	31	26	24.5
		18	42	45	43
		100	65	67	86
		240	127	150	125

the data for 1500°C heat treatments. Data for specimens which were cut 0, 45, and 90° to the rolling direction (RD) are included in each plot. Also included for comparison are grain growth data reported earlier for specimens taken from sheets of the D2 ingot (new process) heat treated at the same temperatures (see Fig. 5) [16]. Examination of the data

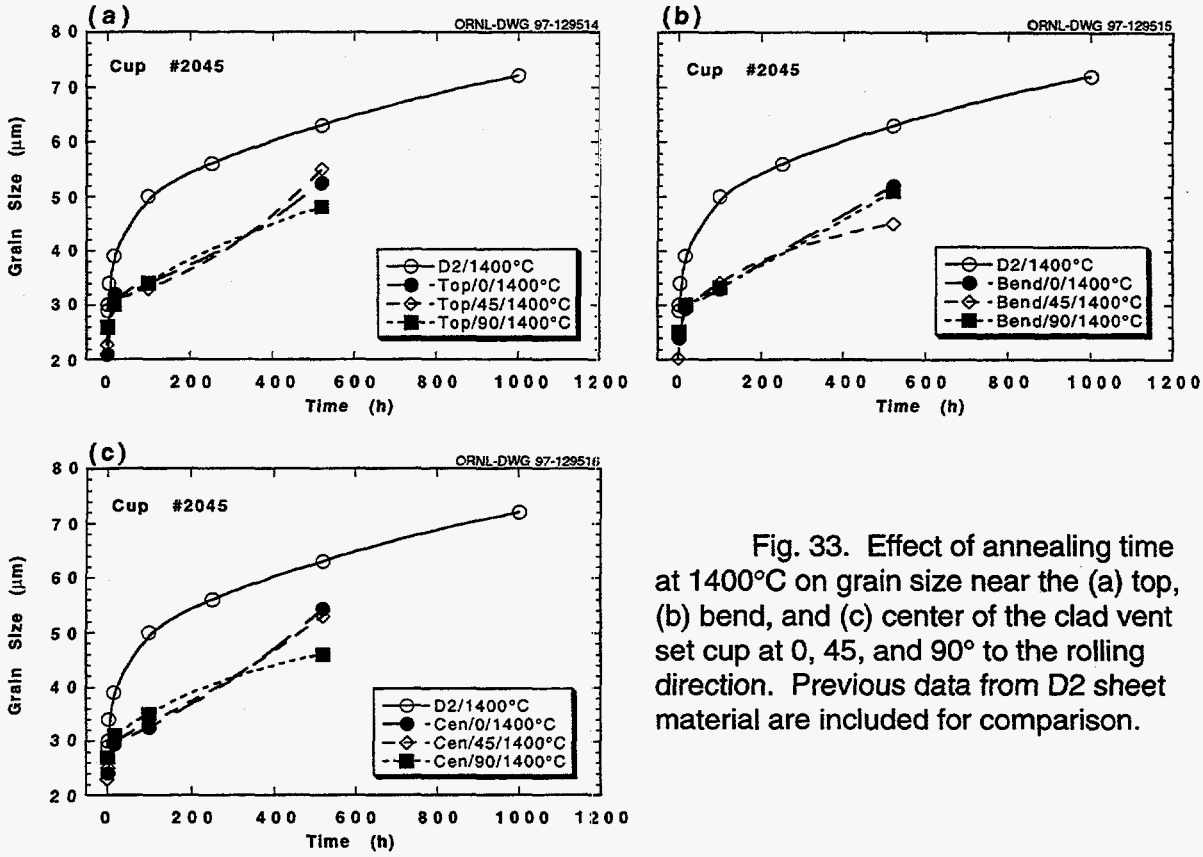

Fig. 33. Effect of annealing time at 1400°C on grain size near the (a) top, (b) bend, and (c) center of the clad vent set cup at 0, 45, and 90° to the rolling direction. Previous data from D2 sheet material are included for comparison.

plotted in Figs. 33 and 34 shows that, within the expected experimental error, no difference in grain size related to the position in the cup with respect to the rolling direction could be determined; grain sizes at 0, 45, and 90° to the rolling direction were comparable at both temperatures. In general, the data show initially a grain size of approximately 20 μm which increased to 40-50 μm after 520 h at 1400°C and to 125-150 μm after 240 h at 1500°C. Figures 35 and 36 show that the grain sizes of specimens taken from the top, bend, and center of the cup are also comparable. These results support the conclusions reported above for the 1-h heat treatments.

A comparison in Figs. 34 and 36 to the data presented in Fig. 5 for D2 sheet material shows that cup material has approximately the same grain growth behavior as the sheet material at 1500°C. Since the earlier data for sheet material goes only to an annealing time of 100 h, it is not possible to determine if the grain growth rate at 1500°C was the same for the cup material versus the sheet material. However, the data at 1400°C (Figs. 33 and 35) indicates that the grain growth rate is approximately the same for sheet and

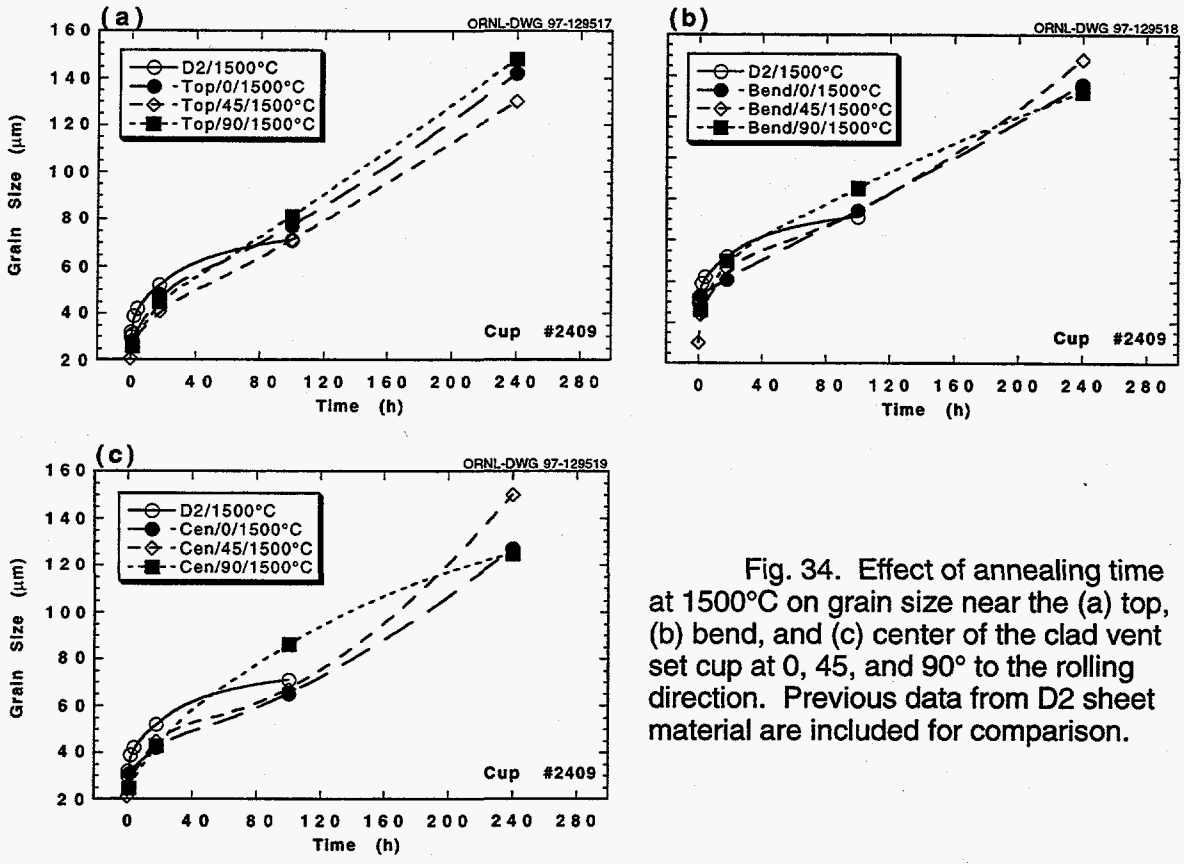

Fig. 34. Effect of annealing time at 1500°C on grain size near the (a) top, (b) bend, and (c) center of the clad vent set cup at 0, 45, and 90° to the rolling direction. Previous data from D2 sheet material are included for comparison.

cup material, but the grain size at each time is much higher for the D2 sheet. This difference in grain size for annealing times at 1400°C can be attributed to the difference in cold work present in the cup versus sheet material. The blank sheet material was not recrystallized before the heat treatments for grain growth studies were performed. It therefore contained considerable cold work (and retained energy) from the rolling operations and therefore recrystallized easily and grew large grains at 1400°C. The cup material, on the other hand, had already been recrystallized during the various fabrication and forming operations necessary to produce the vent cup, and did not contain enough energy to produce large grains at this temperature. The 1500°C temperature was high enough to give the extra energy the cup material needed for grain growth. Therefore, at this higher temperature, grain sizes of cup material were more comparable to the sheet material. This conclusion is also illustrated in Fig. 37 which shows the large increase in grain growth rate between the 1400 and 1500°C anneals.

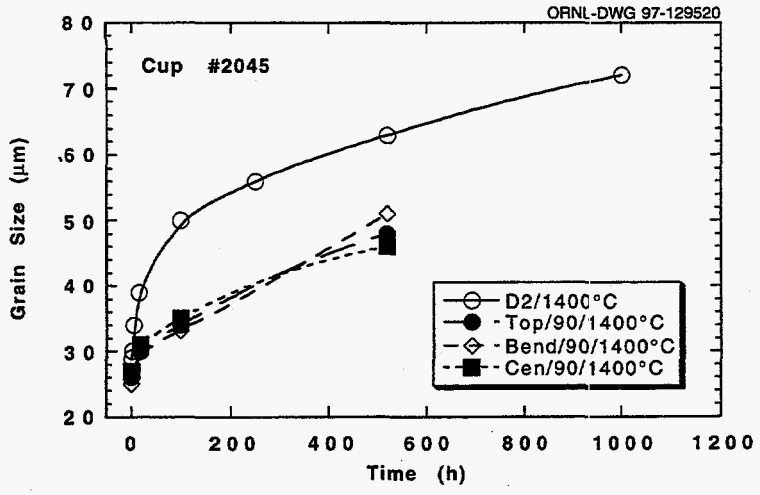

Fig. 35. Effect of annealing time at 1400°C on grain size at 90° to the rolling direction for specimens taken from the top, bend, and center locations in the clad vent set cup. Previous data from D2 sheet material are included for comparison.

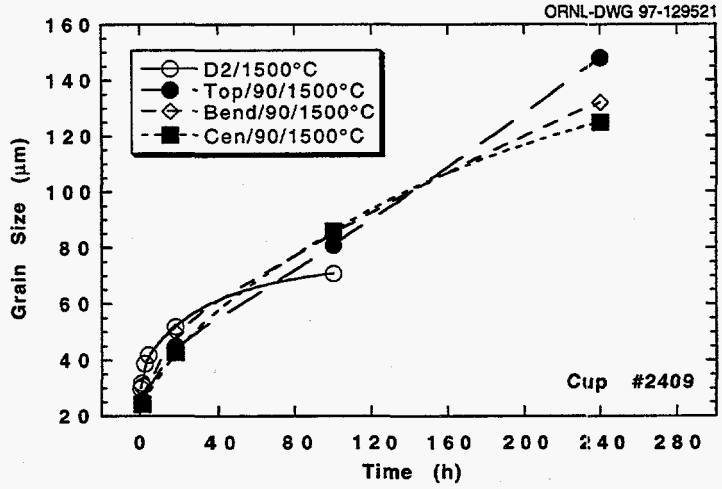

Fig. 36. Effect of annealing time at 1500°C on grain size at 90° to the rolling direction for specimens taken from the top, bend, and center locations in the clad vent set cup. Previous data from D2 sheet material are included for comparison.

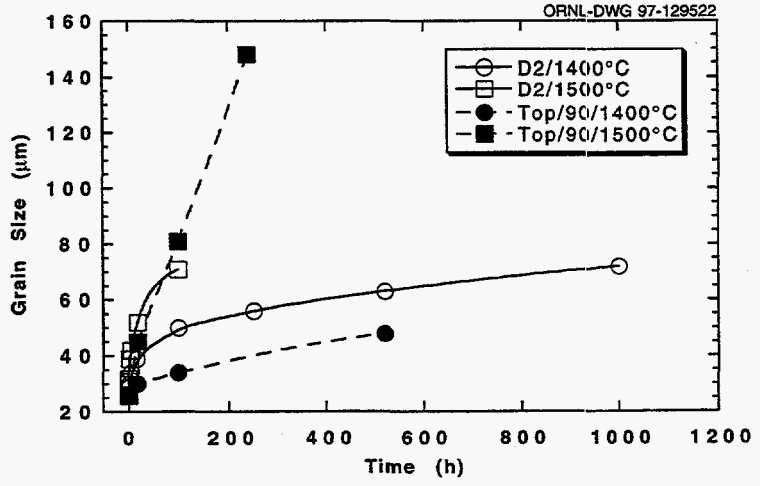

Fig. 37. Effect of annealing time at 1400 and 1500°C on grain size of specimens taken from the top of the clad vent set cup at 90° to the rolling direction. Previous data from D2 sheet material are included for comparison.

Conclusions

Based on heat treatments of one hour at temperatures between 1200 and 1800°C and for various times at 1400 and 1500°C, the grain growth characteristics of specimens taken from Cassini clad vent set cup material (fabricated by the new-process) appears to be the same as specimens taken from the blank sheet material from which the cups were fabricated. There also does not appear to be any difference in grain growth between specimens taken from different locations in the cup relative to the rolling directions or cup geometry. It is therefore anticipated that the mechanical properties of the clad vent set material will be comparable to the blank sheet material.

HIGH-TEMPERATURE HIGH-STRAIN-RATE TENSILE DUCTILITY

Results

Specimens for high-temperature high-strain-rate tensile testing were heat treated in vacuum for 1 h at temperatures between 1300 and 1800°C. The average grain sizes produced ranged between approximately 21 and 117 μm. Table XV and Figure 38 show, for new-process DOP-26, the variation in ductility with grain size (number of grains across 0.64 mm thickness) for test temperatures from 800 to 1100°C. A general trend of decreasing ductility with increasing grain size irrespective of test temperatures can be seen. By

Table XV. High-Temperature High-Strain-Rate Tensile Ductility vs Grain Size and Test Temperature for New-process DOP-26

Impact Test Temp. (°C)	Ductility (%)[a]						
	21.5 μm (1300°C)	24.1 μm (1350°C)	27.2 μm (1400°C)	32.9 μm (1500°C)	47.1 μm (1600°C)	59.6 μm (1700°C)	116.6 μm (1800°C)
800	24.0		16.4	16.5	15.0		7.0
850	21.8		16.5		9.4		5.1
900	30.7		19.6		13.2	10.4	7.7
980		33.7	35.9	35.4	16.9	7.7	4.7
1050	39.4		32.2		30.6	16.5	
1100	45.3		39.9	42.3	36.9	28.9	9.2

[a] Column headings denote grain size and the 1-h vacuum annealing temperature used to produce that grain size.

comparing the straight lines of fit obtained for different test temperatures, one can see the tendency for ductility to increase with increasing test temperature for a given grain size. Another observation that can be made from Fig. 38 is that at test temperatures around 1100°C, new-process DOP-26 is quite ductile independent of grain size.

Figure 39 is a plot of high-temperature high-strain-rate tensile ductility for new-process DOP-26 as a function of test temperature for various grain sizes. Within experimental scatter, new-process DOP-26 exhibits a similar variation of ductility with temperature for different grain sizes, with ductility increasing with increase in test temperature. The brittle-to-ductile transition shifts progressively to higher temperatures with increasing grain size until, at the largest grain size tested, the alloy remains brittle (i.e., ductility of <10%) throughout the whole test temperature range. By the same token, at the smallest grain

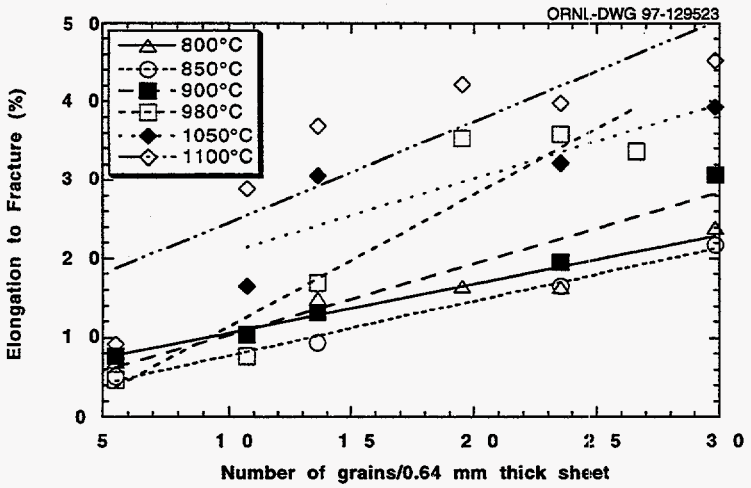

Fig. 38. High-temperature high-strain-rate tensile ductility of new-process DOP-26 as a function of grain size for various test temperatures in the range of 800 to 1100°C.

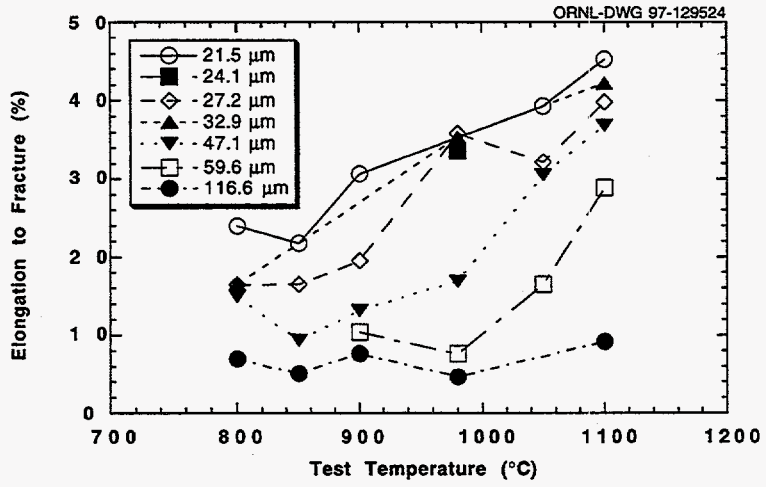

Fig. 39. High-temperature high-strain-rate tensile ductility of new-process DOP-26 as a function of test temperature for grain sizes in the 22 to 117 µm range.

size (or highest test temperature) the alloy is relatively ductile over the whole temperature (or grain size) range tested. As seen in Fig. 38, samples with smaller grain sizes possess higher ductilities compared to those with larger grain sizes.

The effects of grain size and test temperature on ductility can be combined in one plot, as shown in Fig. 40 which gives constant ductility contours in a two-dimensional grain size-test temperature plot. It is quite evident that samples with large grain sizes (above ~45 μm) give low ductilities at low test temperatures, and ductility values increase slightly with increasing temperature. High ductilities are, in general, characteristic of samples with small grain sizes at all test temperatures.

Figure 41 shows the ductility of old-process DOP-26 as a function of the number of grains across a 0.64-mm-thick sheet for test temperatures in the range of 800 to 1100°C. These data were obtained from the final safety analysis report for the Galileo mission [33]. To facilitate comparison with the new-process ductilities reported above, Fig. 42 replots the data for old- and new-process DOP-26 as separate graphs for each individual test temperature. It is seen that new-process DOP-26 has ductilities comparable to or better than those of old-process DOP-26 over the temperature and grain size ranges tested.

Figure 43 shows the typical fracture surfaces of new-process DOP-26 after testing at various test temperatures for one grain size. The fracture mode changes from a predominantly intergranular fracture at low test temperatures (up to ~900°C) to predominantly

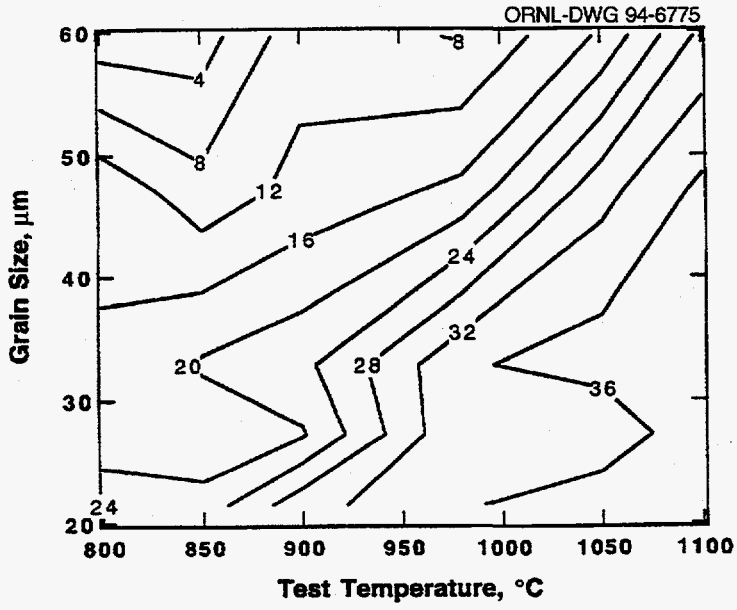

Fig. 40. High-temperature high-strain-rate tensile ductility contours as a function of grain size and test temperature. Ductility values are listed for each constant ductility contour.

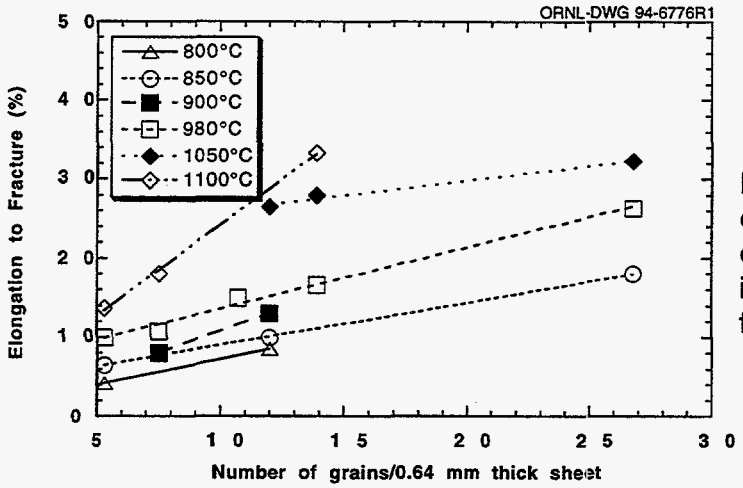

Fig. 41. High-temperature high-strain-rate tensile ductility of old-process DOP-26 as a function of grain size for test temperatures in the 800 to 1100°C range. (Data from ref. 33.)

transgranular fracture at high test temperatures (1050 to 1100°C). In the intermediate test temperatures, the fracture is a mixture of intergranular and transgranular modes.

Figure 44 is a contour map showing the variation in the amount of transgranular fracture in the impact-tested specimens of new-process DOP-26 as a function of grain size and test temperature. In general, the amount of transgranular fracture increases with ductility. Thus, the amount of transgranular fracture increases as one moves from the top left to the bottom right of Fig. 44, consistent with the constant ductility contours of Fig. 40. The failure mode of samples with large grains (with grain size of >45 μm) is predominantly intergranular at low and medium test temperatures, and becomes slightly transgranular at high test temperatures. In contrast, samples with smaller grains fail in a predominantly transgranular fashion at low and medium temperatures, and in a highly ductile mode at higher temperatures.

From Figs. 40 and 44 a broad correlation between ductility, which is a function of both grain size and test temperature, and the amount of transgranular fracture can be seen. In general, higher ductilities (at high test temperatures and small grain sizes) are associated with transgranular fracture, and lower ductilities (at low test temperatures and large grain sizes) are associated with intergranular fracture. This is consistent with the observations made earlier from Fig. 38 and 39 about the dependence of ductility on grain size and test temperature.

Figure 45 shows the variation of ductility with test temperature for old- and new process DOP-26. These alloys were tested with the new specimen design. The results

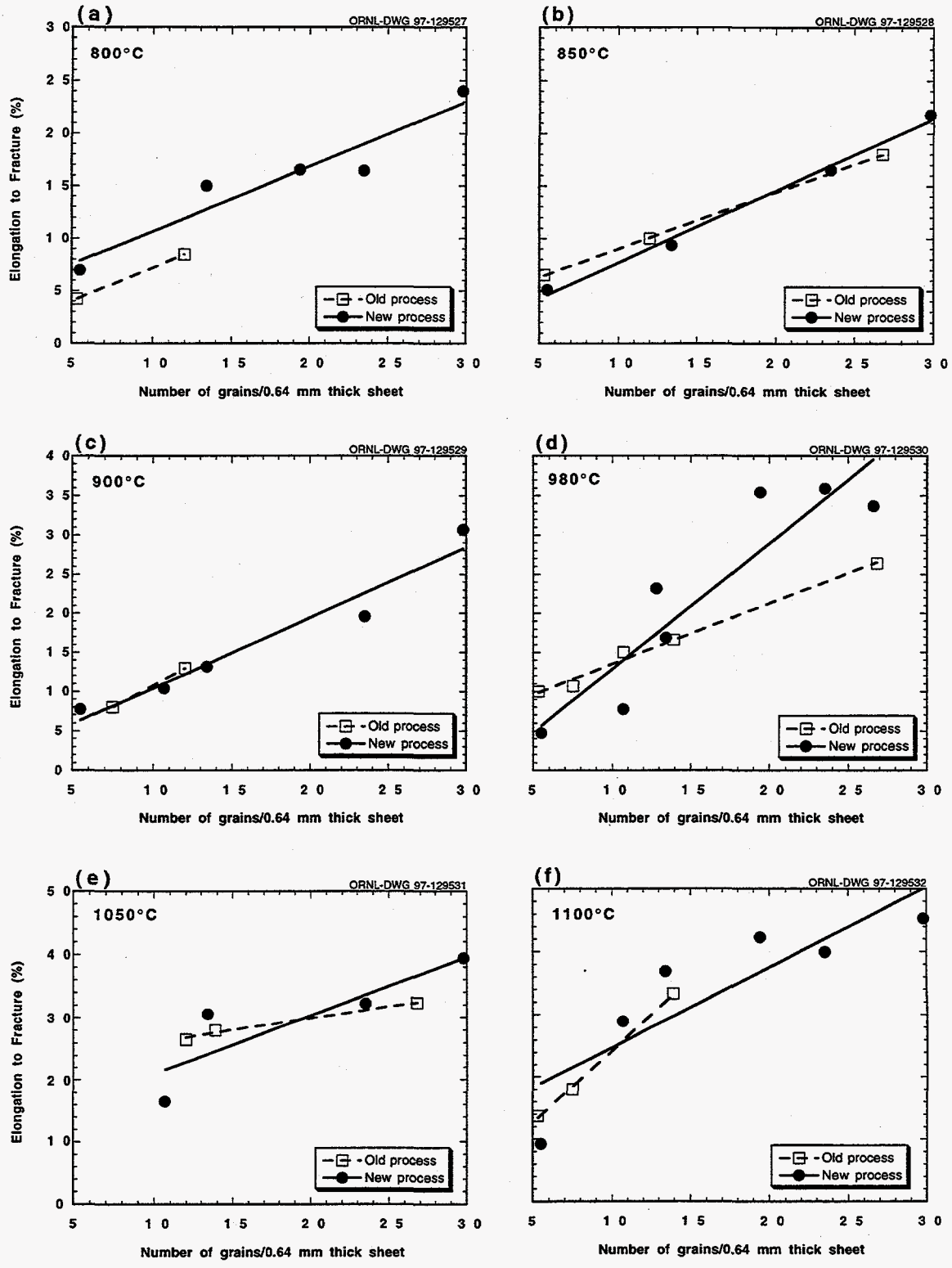

Fig. 42. Comparison of high-temperature high-strain-rate tensile ductilities of new- and old-process DOP-26 with grain size at (a) 800, (b) 850, (c) 900, (d) 980, (e) 1050, and (f) 1100°C.

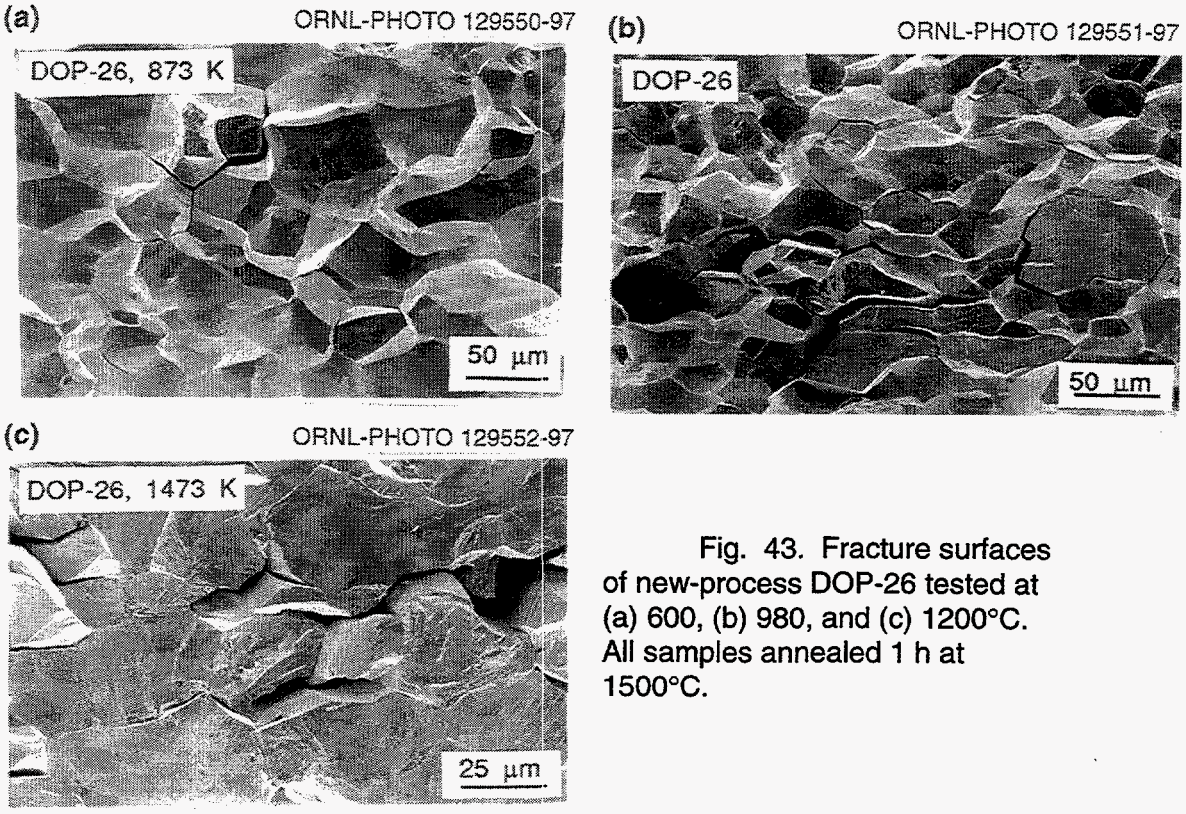

Fig. 43. Fracture surfaces of new-process DOP-26 tested at (a) 600, (b) 980, and (c) 1200°C. All samples annealed 1 h at 1500°C.

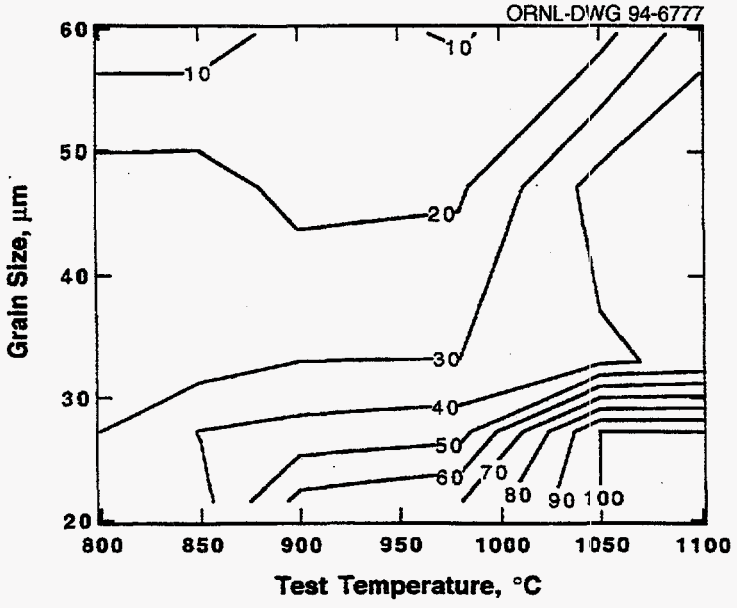

Fig. 44. Contour map showing percent transgranular fracture as a function of grain size and test temperature for new-process DOP-26. The values on each contour give the percent transgranular fracture for that particular line.

obtained earlier for old-process DOP-26 with the old specimen design [33] are also shown in Fig. 45. It is seen that old- and new-process DOP-26 have essentially identical ductilities at all test temperatures as long as the same specimen design is used. However, old-

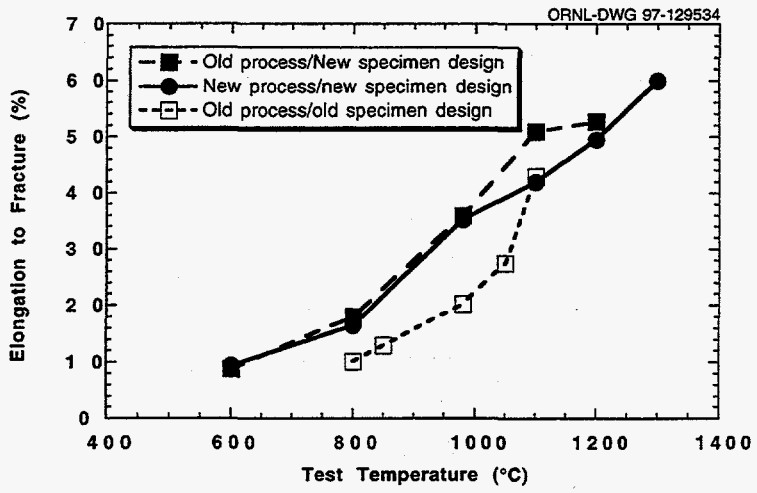

Fig. 45. Variation of high-temperature high-strain-rate tensile ductility with test temperature for new- and old-process DOP-26.

process DOP-26 tested using the old specimen design has lower ductility than when it is tested using the new specimen design (at least at intermediate test temperatures). This is not surprising given that the new specimen preparation procedure minimizes surface flaws and is therefore expected to produce results more nearly representative of the intrinsic ductilities of the alloys being tested. These results indicate that high-temperature high-strain-rate tensile ductilities will not change significantly upon scale-up to the new-process, as long as the new specimen design is used to test both sets of alloys.

Discussion

In order to understand the influence of various factors like grain size and grain boundary cohesion on high-temperature high-strain-rate tensile ductility, one can consider the following equation (derived by considering a model of stress concentrations induced by dislocation pile-ups at grain boundaries) [5]:

$$\varepsilon_f = (\sigma_o - \sigma_i/k) + (\sigma_c/k)\sqrt{(s/d)} \qquad (3)$$

where ε_f = true fracture strain; σ_o = frictional stress against dislocation motion on slip planes; σ_c = cohesive strength of grain boundaries, or critical strength needed for breaking grain boundaries; k and σ_i are strength coefficient and yield strength, respectively, which are material constants; d is the grain diameter; and s is the distance beyond the tip of the pile up. According to this equation, if high-temperature high-strain-rate tensile ductility is

plotted as a function of $d^{-1/2}$, the slope of the resulting straight line gives an indication of grain boundary cohesive strength.

According to equation (3), ductility decreases with increase in grain size. It is already seen in Fig. 38 that there is a decrease in ductility with increase in grain size. Also, equation (3) indicates a linear relationship between ductility and inverse square root of grain size.

Figure 46 is a plot of high-temperature high-strain-rate tensile ductility of new-process DOP-26 as a function of inverse square root of grain size for various test temperatures (data taken from Table XV). At all test temperatures one can observe a reasonably good straight line relationship between ductility and inverse square root of grain size.

In equation (3), k and σ_i are considered as work hardening rate and yield strength of the material, respectively. With increase in temperature one can expect both k and σ_i to decrease. Tensile testing of iridium alloys doped with thorium at a slow strain rate (~10^{-3}/s) by Liu et al. [8] has shown that yield strength decreases with an increase in test temperature from 650 to 1350°C. Work hardening or strain hardening rate for fcc materials, in general, decreases with increasing temperature. This can be attributed to the increase in the tendency for dislocations to cross-slip with an increase in temperature. Hence, it is not unreasonable to assume here that both k and σ_i decrease with an increase in test temperature.

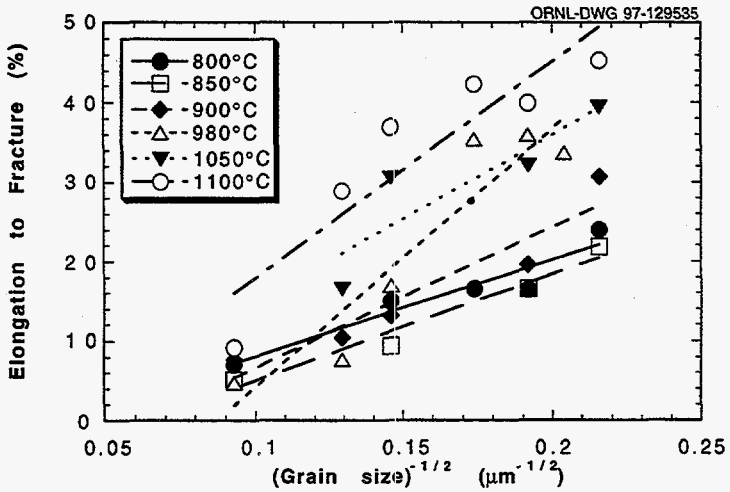

Fig. 46. High-temperature high-strain-rate tensile ductility of new-process DOP-26 material as a function of grain size for test temperatures of 800 to 1100°C.

Equation (3) predicts that high-temperature high-strain-rate tensile ductility increases with a decrease in both k and σ_i (due to increase in test temperature) for a given grain size. This can be seen from Figs. 39 and 41 where, for a fixed grain size, ductility increases with increasing test temperature.

Summary And Conclusions

High-temperature high-strain-rate tensile testing was conducted on samples of new-process DOP-26 in order to study the influence of grain size and test temperature on the ductility. Results reveal that ductility increases with an increase in test temperature and a decrease in grain size. Grain size and test temperature effects on ductility have been explained based on an equation derived from a model of dislocation pile ups at the grain boundaries.

The transgranular fracture contour maps, generated for new-process DOP-26 alloy, show a good correlation among fracture mode, test temperature and grain size. Lower values of transgranular fracture areas (i.e., predominantly intergranular fracture mode at low ductilities) correspond to low test temperatures and large grain sizes, and higher values of transgranular area (i.e., ductile, predominantly transgranular fracture at high ductilities) are predicted for high test temperatures and small grain sizes.

Similarly, the ductility contour maps that were generated predict lower ductilities for low test temperatures and large grain sizes, and ductility increases with increasing test temperature and decreasing grain size. A broad correlation between ductility and transgranular fracture was seen, by comparing the corresponding contour maps, with intergranular fracture associated with lower ductilities and transgranular fracture with higher ductilities.

Comparison of the results from high-temperature high-strain-rate tensile testing of old- and new-process DOP-26 alloys using the new specimen design at a constant grain size and different test temperatures indicates that there is no significant difference in the ductilities of the two alloys. Also, old-process DOP-26 exhibits higher ductility when tested using new specimen design than that obtained using the old specimen design. This is due to the improved surface finish obtained in the new specimen preparation.

Grain growth studies in an earlier investigation revealed that the kinetics of grain growth for old- and new-process DOP-26 alloys is essentially identical for all temperatures and times tested. Hence, it can be concluded that scaling-up the alloy fabrication to the new-process will not affect either the high-temperature high-strain-rate tensile ductility (as long as the alloys are tested using the new specimen design) or the grain growth kinetics.

EFFECT OF LOW-PRESSURE OXYGEN EXPOSURE ON HIGH-TEMPERATURE HIGH-STRAIN-RATE TENSILE DUCTILITY

Results and Discussion

In Fig. 47 the closed symbols show the high-temperature high-strain-rate tensile ductility as a function of test temperature for new- and old-process DOP-26 in both the as-recrystallized-in-vacuum and the oxygen-annealed conditions. Included for comparison (open symbols) are data presented above in Table XV [20] for vacuum-annealed specimens with comparable grain sizes of 47.1 and 59.6 μm. The average grain size (21-23 μm) and the ductilities for the as-recrystallized specimens are comparable to data reported in Fig. 4 for new- and old-process DOP-26 material recrystallized for 1 h at 1375°C

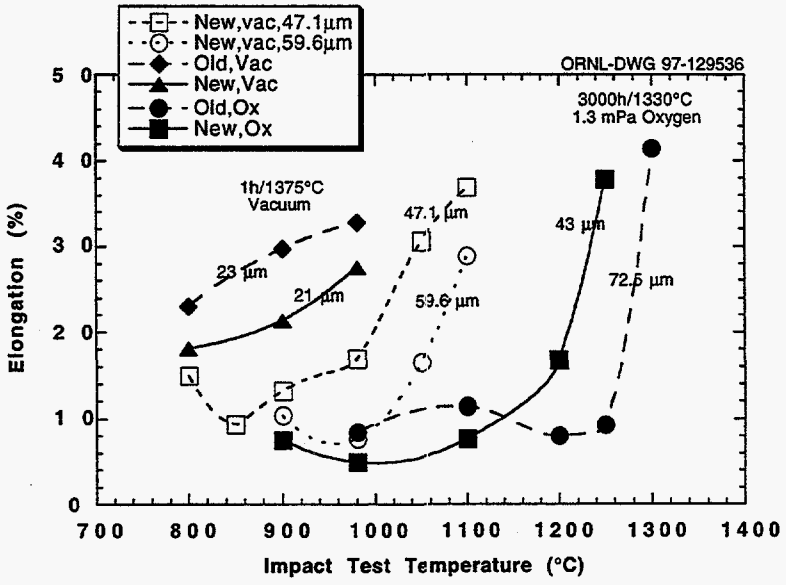

Fig. 47. High-temperature high-strain-rate tensile ductility of old- and new-process DOP-26 after low-pressure oxidation (1.3 mPa oxygen) for 3000 h at 1330°C compared to data on vacuum-annealed new-process specimens.

in vacuum [16,20]. The fracture mode was transgranular cleavage over the entire temperature range tested (Fig. 48). However, the average grain size of the oxygen-annealed specimens was much larger (43 μm for the new-process and 72 μm for the old-process materials) and they exhibited a significant embrittlement compared to the as-recrystallized specimens, both in terms of reduced ductility at any specific test temperature and in the shift of the brittle-to-ductile transition to higher temperatures. As noted above, the biggest factor producing this embrittlement was the depletion of thorium during oxidation. But part of the total embrittlement is due to grain size differences; as noted previously [8,9,15,20] and above in this report, increasing the grain size is known to reduce ductility. A comparison of the curve for the 21-μm grain-size vacuum-annealed material with the curve for the 47-μm grain-size vacuum-annealed material gives an indication of the degree of embrittlement produced by grain growth alone. These curves indicate that doubling the grain size alone results in an increase of the DBT temperature from approximately 800°C to about 1000°C.

The oxygen-annealed old-process material used in this study had a uniform distribution of grains of 72 μm average diameter, while the new-process material showed evidence of anomalous near-surface grain growth and an average grain size of 43 μm (see Fig. 49). In order to isolate the effect of anomalous grain growth during oxygen annealing from other possible embrittling mechanisms, a comparison of the high-temperature high-strain-rate tensile ductilities for the 47 μm vacuum-annealed and the 43 μm oxygen-annealed new-

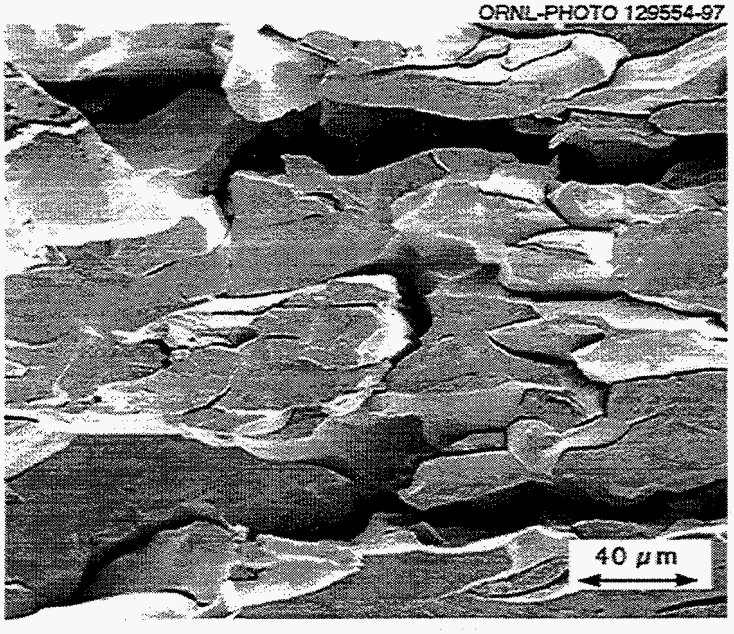

Fig. 48. Scanning electron fractograph of as-recrystallized new-process DOP-26 tensile tested at 980°C. Ductility was 27.6%.

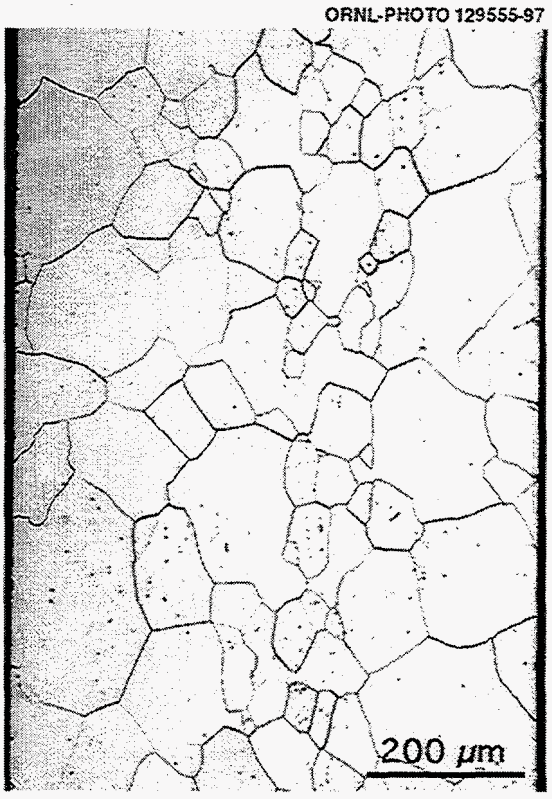

Fig. 49. Optical micrograph showing typical microstructure of new-process DOP-26 oxygen-annealed for 3000 h at 1330°C. Note anomalous growth of near-surface grains.

process material shows that oxygen-annealing reduced the ductility significantly for test temperatures between approximately 900 and 1200°C. Bearing in mind that each data point in Fig. 47 represents only 1-2 tests, oxygen-annealing appears to have also shifted the brittle-to-ductile transition temperature from approximately 1000°C to 1200°C for specimens having nominally the same average grain size.

This shift is probably caused by a combination of two factors: anomalous grain growth of near-surface grains and thorium depletion at grain boundaries leading to decreased cohesion. These events occur simultaneously in a high-temperature oxygen containing environment and can be explained by a mechanism proposed by White and Liu [11]. As noted above, in the DOP-26 alloy, thorium segregates to grain boundaries, producing an increase in cohesive strength, and, in excess of the solubility limit, forms Ir_5Th precipitates in the matrix that enhance strength through grain-boundary pinning and grain size refinement. However, during annealing in atmospheres containing even low partial pressures of oxygen, the dissolution of the Ir_5Th precipitates and diffusion of thorium to the surface to form ThO_2 are thermodynamically favorable, leading to anomalous

growth of grains near the surface and decreased cohesive strength of the grain boundaries.

The effect of decreased cohesion due to depletion of thorium from the grain boundaries during oxygen annealing is difficult to quantify. However, the question of whether the near-surface grain size has an effect on high-temperature high-strain-rate tensile ductility can be discussed with respect to the data presented in Fig. 47. The new-process oxygen-annealed specimens had near-surface grains that ranged between 60 and 80 μm in diameter, but an average grain size of 43 μm (see Fig. 49). The old-process material was uniform in morphology with an average grain size of 72 μm. However, for test temperatures below the DBT (which for oxygen-annealed specimens is near 1200°C as indicated in Fig. 47), testing of both materials resulted in low ductilities and fracture surfaces that were almost totally intergranular in appearance [see Fig. 50(a)]. Above the DBT, much greater ductilities and totally trans-granular cleavage failure were observed [see Fig. 50(b)]. Previous results shown above in Fig. 39 showed that as-recrystallized DOP-26 with grain sizes in the 40-50 μm range have a DBT near 1000°C. Below this temperature, the ductilities are 10-20% and the fracture surfaces are mixed mode with 20-30% transgranular cleavage. In contrast, the unoxidized as-recrystallized specimens used in this study (grain size = 21-23 μm) showed a transgranular fracture mode which is typical of ductile DOP-26 (see Fig. 48). This difference in ductility between the as-recrystallized and oxygen-annealed specimens of comparable grain size indicates that the size of the near-surface grains is an important parameter in producing embrittlement. The extremely large near-surface grains observed in this study resulted in large unstable crack nuclei that propagated quickly through the specimen, producing a brittle intergranular fracture in tests below 1200°C.

The shift of the data in Fig. 47 for the old-process oxygen-annealed material compared to the new-process oxygen-annealed material may be due to compositional differences between the two heats used. Our previous oxidation study at 1330°C (described above), in which old-process material from heat ZR-600 was used, indicated that after 3000 h the average grain size of DOP-26 should be approximately 50-60 μm. The results of that study indicated that there should be no significant difference in grain growth characteristics in low-pressure oxygen for the new-process compared to the old process material. The larger grain size of the A604 heat used in the current study and the shift in the data curves in Fig. 47 for oxygen-annealed old- and new-process material is believed to be due

Fig. 50. Scanning electron fractographs of oxygen-annealed new-process DOP-26 high-strain-rate tested at (a) 980 (ductility was 5.1%) and (b) 1300°C (ductility was over 40%).

to the lower thorium content of the A604 old-process heat. The A604 heat contains only 48 ppm Th instead of the 69 ppm Th present in the ZR-600 heat [34]. It has been known for some time that the metallurgical and mechanical properties of Ir 0.3 % W alloys are affected by the amount of thorium addition [8]. The lower thorium concentration of the A604 heat explains not only the shift in the high-temperature high-strain-rate tensile ductility, but also the difference in the grain morphology that was observed in the optical metallography

specimens. The lower thorium content means that, under the oxidizing conditions used in this study, the specimens made from the A604 heat were probably depleted of thorium (and therefore lost the grain-boundary pinning action of the Ir_5Th particles), while the F2 material still had enough thorium toward the center of the specimen to slow down the grain growth.

Conclusions

In summary, high-temperature high-strain-rate tensile tests as a function of test temperature were conducted on both old- and new-process DOP-26 specimens which had been exposed to 1.3 mPa of oxygen for 3000 h at 1330°C. The ductility data were then compared to data from specimens that had been recrystallized in vacuum at 1375°C (the standard recrystallization temperature) to produce grain sizes of 21-23 μm and to specimens that had been recrystallized at higher temperatures in vacuum to produce grain sizes comparable to those produced by the oxygen-annealing conditions used in this study. The results indicate that exposure to low-pressure oxygen embrittles both old- and new process DOP-26 material, and that the embrittlement is due to the loss of thorium and the growth of the near-surface grains in the oxygen-annealed specimens. In this series of tests, the brittle-to-ductile transition temperature was increased (for comparable average grain sizes of new-process material) from approximately 1000°C in the unoxidized samples to 1200°C in the oxygen-annealed samples.

GRAIN GROWTH BEHAVIOR AND HIGH-TEMPERATURE HIGH-STRAIN-RATE DUCTILITY OF WELDED DOP-26

Results and Discussion

Figure 51 shows optical micrographs of the weld centerline, weld metal, and base metal of new-process DOP-26 in the as-welded condition (a recrystallization anneal of 1 h at 1300°C was done before welding). In this condition, the grain sizes were approximately 22, 41, and 72 μm in the base metal, weld centerline, and weld metal, respectively.

The results of the grain growth study at 1400 and 1500°C are presented in Table XVI and plotted in Figs. 52 and 53. Representative optical microstructures of the welded, heat-treated DOP-26 material are shown in Figs. 54 and 55. All grain sizes were measured

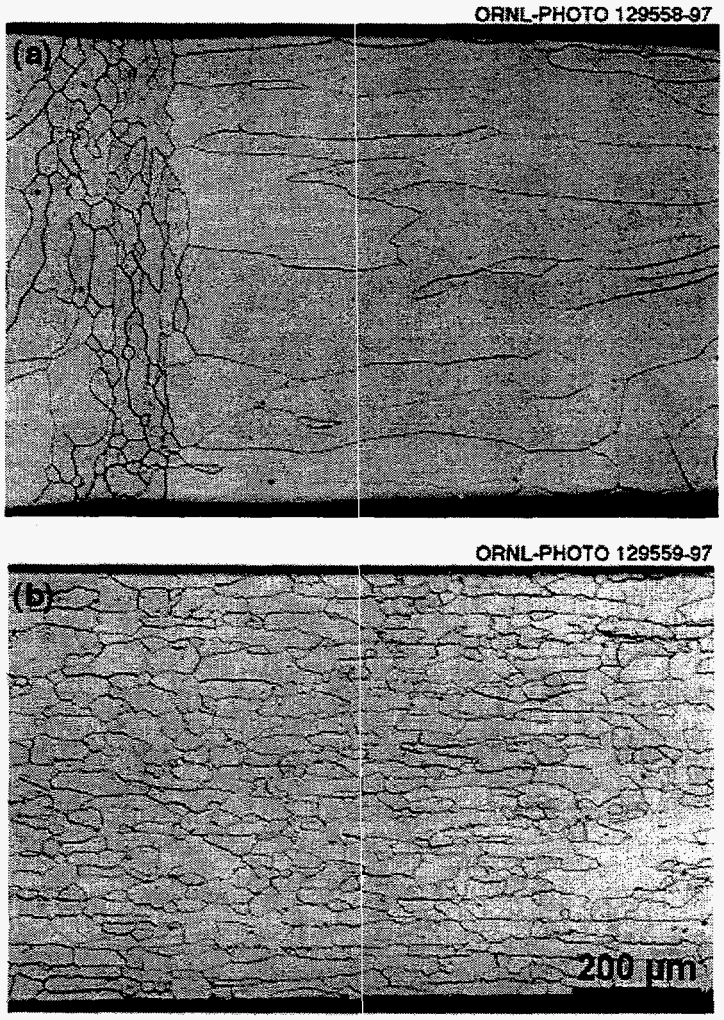

Fig. 51. Optical micrographs of the (a) weld centerline and weld metal and (b) base metal of welded new-process DOP-26.

in a direction perpendicular to the thickness of the sheet in a plane parallel to the rolling direction; the number in parentheses in Table XVI is the number of intercepts counted. The width of the weld region was approximately 3000-3500 μm in all the samples tested. The grain size of the base metal was measured at a distance of at least 2000 μm from the centerline of the weld (outside of the weld region and heat-affected zone).

Figure 52(a) shows that at 1400°C the grain size of the base metal grew slowly from approximately 22 μm to about 45 μm after 1065 h. During this same length of exposure, the grain size of the weld centerline and weld metal remained fairly constant at approximately 30-60 and 70-85 μm, respectively. At 1500°C, however, the grain sizes of all three

Table XVI. Grain Growth Data for Welded DOP-26

Blank designation	Heat Treatment		Grain Size (μm)		
	Temperature (°C)	Time (h)	Base metal[a]	Weld centerline[c]	Weld metal[d]
FR3-6		0	21.5 (700)	40.6 (18)	72.5 (21)
FR3-6	1400	4	24.2[b] (600)	29.6 (23)	84.4 (17)
		18	24.0[b] (612)	30.0 (20)	85.6 (17)
		110	27.2[b] (538)	26.1 (23)	78.4 (19)
		250	36.9[b] (384)	57.5 (12)	76.5 (19)
		565	33.0[b] (451)	32.7 (22)	71.6 (21)
		1065	44.6[b] (358)	42.4 (21)	82.4 (27)
ER6-15	1500	4	35.0[b] (423)	51.5 (13)	73.9 (19)
		18	51.0[e] 580)	37.8 (18)	81.4 (17)
		96	293.5[e] (164)	34.7 (19)	78.7 (16)
		250	400.9[e] (85)	206.7 (3)	610.0 (2)

[a] Grain size of the base metal was measured at approximately 2000 μm from the centerline of the weld in a direction perpendicular to the thickness of the sheet.
[b] The error in the data represents the standard deviation in the grain sizes measured for 11 lines across a field approximately 1100 μm wide.
[c] The approximate position of the centerline of the weld was marked and the grain size was measured perpendicular to the thickness of the sheet.
[d] Grain size of the weld metal was measured perpendicular to the sheet thickness at a distance of approximately 500 μm from each side of the centerline of the weld.
[e] The error in the data represents the standard deviation in the grain sizes measured for approximately 50 lines across the specimen.

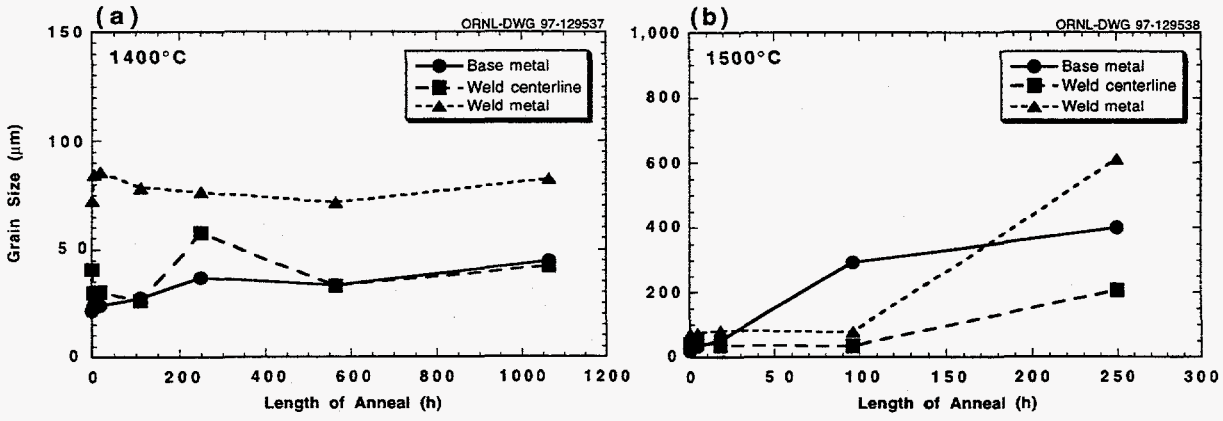

Fig. 52. Grain size of base metal, weld centerline, and weld metal in new-process welded DOP-26 heat treated at (a) 1400 and (b) 1500°C.

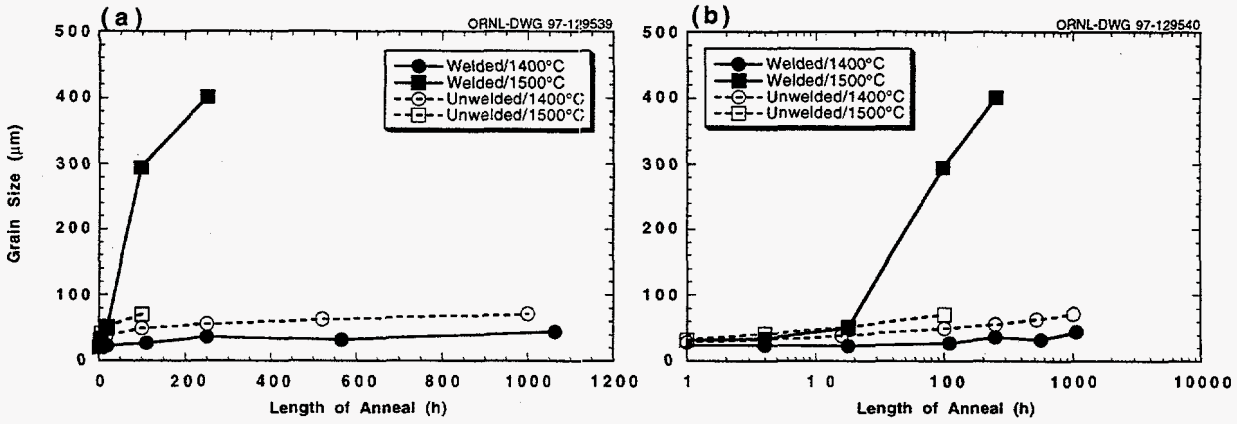

Fig. 53. Linear (a) and log annealing time (b) plots of base metal grain size versus time of anneal at 1400 and 1500°C.

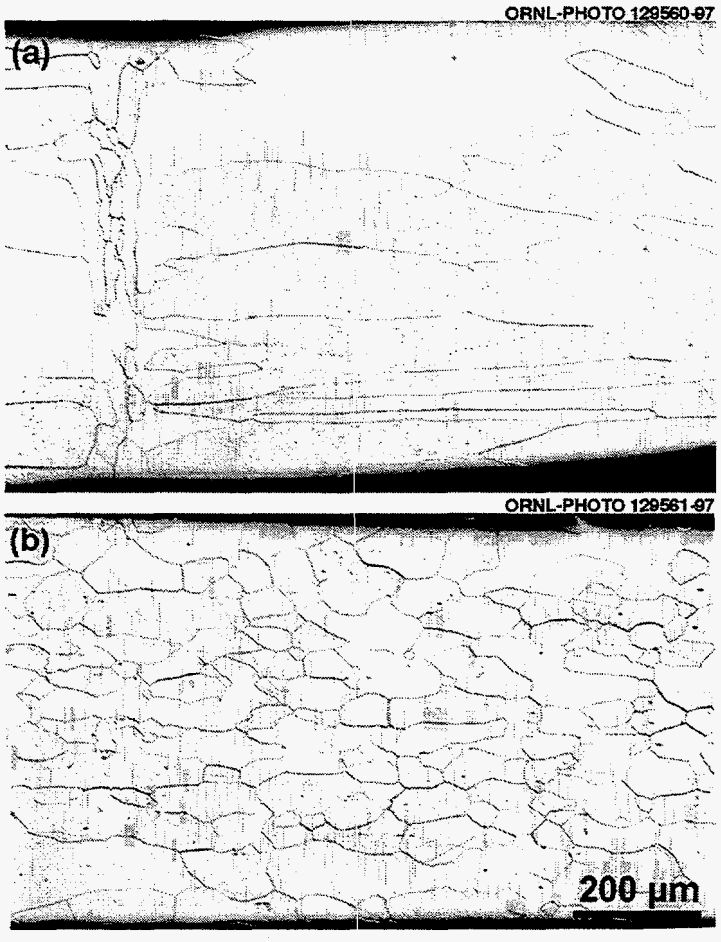

Fig. 54. Optical micrographs of the (a) weld centerline and weld metal and (b) base metal of welded new-process DOP-26 after a heat treatment of 250 h at 1400°C.

Fig. 55. Optical micrographs of the (a) weld centerline and weld metal and (b) base metal of welded new-process DOP-26 after a heat treatment of 18 h at 1500°C.

regions started to increase after short annealing times; the base metal grain size had increased even for the 4 h anneal, while the weld centerline and weld metal began increasing dramatically between the 96 and 250 h anneals. The base metal microstructure was fairly uniform for all 1400°C anneals up through the one at 565 h and for the 4 h at 1500°C anneal (see Fig. 54). The 1065 h anneal at 1400°C and the 4, 18, and 96 h anneals at 1500°C produced anomalously large grains mixed in with the otherwise uniform microstructure (see Fig. 55). The 250 h anneal at 1500°C resulted in only very large grains (Fig. 56). In this specimen, the weld zone was completely obliterated and its location was detectable only as a thicker region between two areas of reduced thickness. Because of the large grain size and the smaller number of intercepts counted, the scatter in the grain size measurements for this specimen were very large.

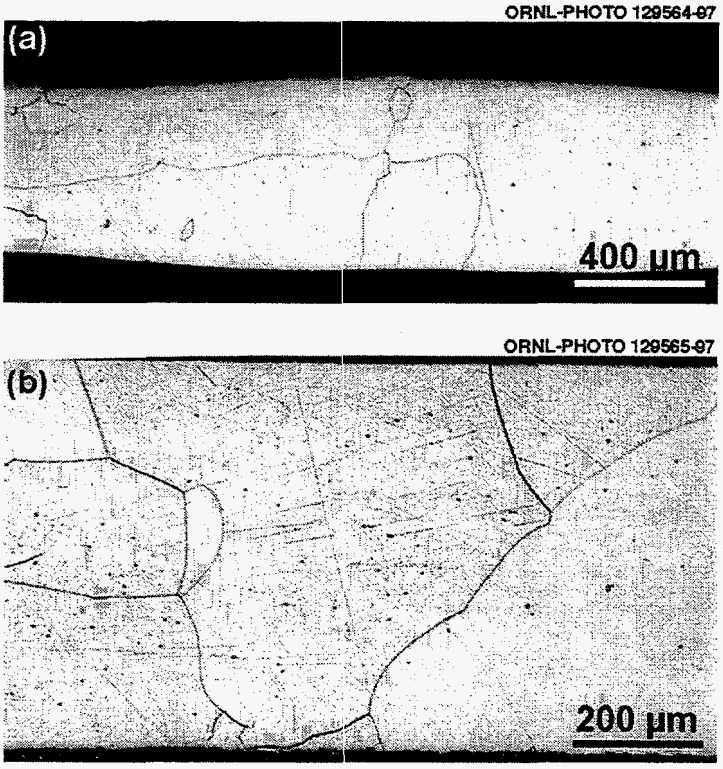

Fig. 56. Optical micrographs of the (a) weld centerline and weld metal and (b) base metal of welded new-process DOP-26 after a heat treatment of 250 h at 1500°C.

Figure 53(a) compares the grain size for the base metal of the welded specimens to the data shown in Fig. 5 for unwelded new-process DOP-26 [16]. It is plotted using log values of the time in Fig. 53(b) in order to better compare grain sizes at times less than 20 h. At 1400°C the data are comparable for the welded and unwelded material. At 1500°C, the measured grain sizes of the welded DOP-26 are much greater than that of the unwelded material at annealing times of 100 and 250 h. However, as noted above, the scatter in the 1500°C grain size data of the welded specimens was very large as a consequence of the fewer number of grain boundaries across the thickness of the specimens [as shown in the micrograph in Fig. 56(a)]. Consequently, for the 100 h anneal, the actual average grain size of the welded specimen could be much closer to the grain size range for the unwelded specimen.

Table XVII and Fig. 57 show the elongations to fracture versus test temperature for high-temperature high-strain-rate tensile tests conducted on the welded new-process

Table XVII. High-Temperature High-Strain-Rate Tensile Ductility of Welded DOP-26

Blank Designation[a]	Test Temperature (°C)	Ductility (%)	Average Ductility (%)	Fracture mode	Position of fracture
E5-17	900	14.4	11.6		base metal
ER8-1		8.7		IG+TG	base metal
E5-17	980	15.1	12.4	IG[b]	weld centerline
ER8-1		9.6		IG[b]	weld centerline
E5-17	1100	10.6	13.2	IG[b]	weld centerline
ER8-1		15.9		TG+IG	base metal
AR2-15	1200	10.0	11.4		weld centerline
AR2-15		12.7		IG[b]	weld centerline

[a]Heat treatment = 19h/1500°C.
[b]Although predominantly intergranular, about 10% transgranular cleavage was observed.

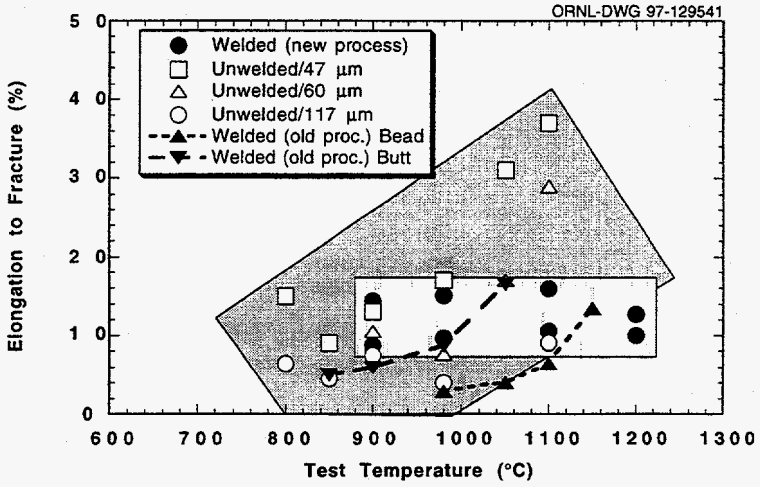

Fig. 57. Ductility versus test temperature for welded new-process DOP-26 (light shaded region). For comparison purposes, data for old-process DOP-26 material with butt or bead-on-plate welds (dashed lines) [21] and new-process DOP-26 with grain sizes of 47, 60, and 117 μm (dark shaded region) are included [20].

DOP-26. The elongation ranged from approximately 9 to 15% and did not appear to be dependent on the test temperature. Also included in Fig. 57 are ductility data (replotted from Fig. 39 above) for unwelded new-process DOP-26 at grain sizes of 47-117 μm [20], a grain size range which is comparable to the grain sizes measured for the weld centerline and weld metal in the current specimens (see Table XVI). The elongation for the welded

DOP-26 is comparable to unwelded material at test temperatures below approximately 980°C. Data for welded (both 2.5 mm-wide butt welds and 3.7 mm-wide bead-on-plate welds) old process DOP-26 [21,35], with a post-weld heat treatment of 1 h at 1500°C as opposed to the 19 h at 1500°C used in this study, are included in Fig. 57 (dashed lines) for comparison purposes. A comparison of the data in Fig. 57 shows that the ductilities of the old- and new-process materials fall within the same broad scatter band.

Figure 58 shows the ductility as a function of distance along the 12.7 mm gage length for three representative specimens tested at 900, 980, and 1100°C. These values were obtained by first using a 1000-g load on a microindentation tester to place small indents along the gage of each specimen. The elongations were then determined by measuring the distances between the indents before and after testing. In this figure, the approximate position of the weld region (which includes the weld centerline and the heat affected zone) is denoted by a shaded region. All three of these specimens fractured near the weld centerline and the approximate position of the fracture is also noted in the figure. The data in this figure indicates that elongation during testing was approximately uniform along the gage length of the specimen, irrespective of the presence of the weld.

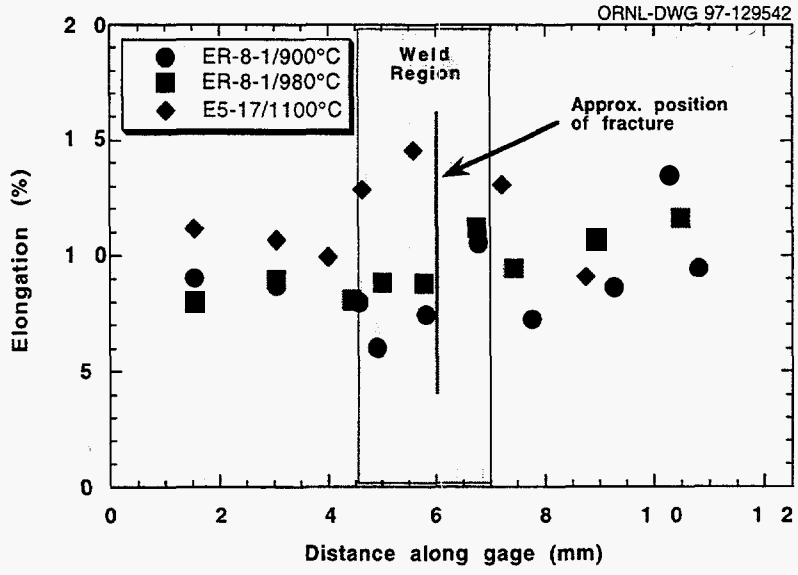

Fig. 58. High-temperature high-strain-rate tensile ductility of welded new-process DOP-26 measured at points along the gage length of the specimen.

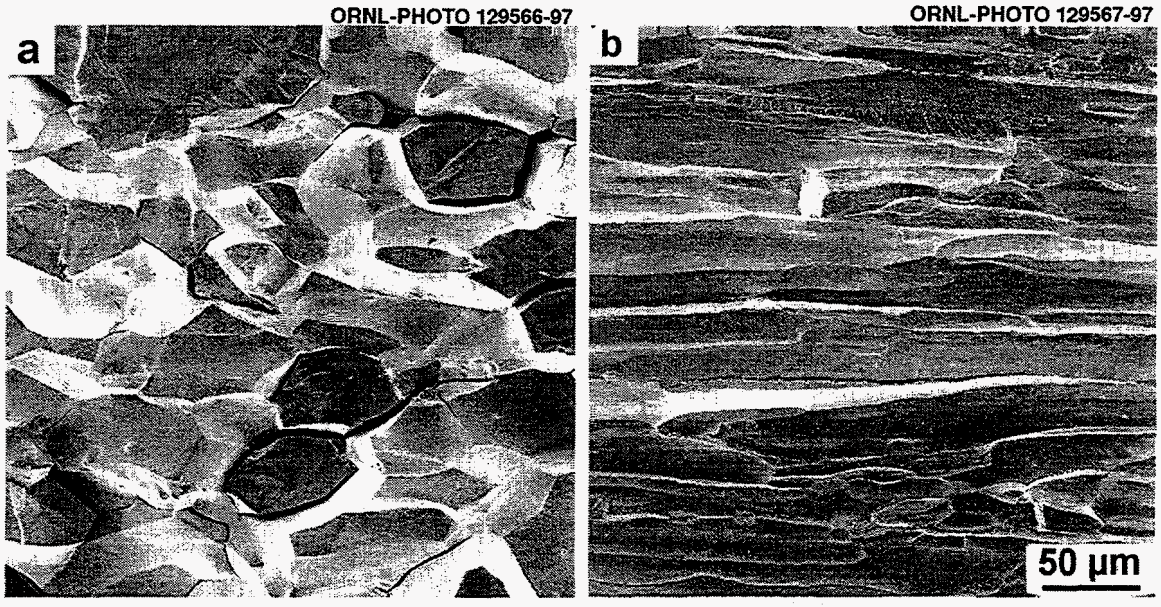

Fig. 59. Scanning electron micrographs of the fracture surfaces of welded new-process DOP-26 impact tested at (a) 900 (fractured in base metal) and (b) 980°C (fractured in weld centerline).

The fracture surfaces were studied using scanning electron microscopy (SEM) and representative fractographs are shown in Fig. 59. At 900°C the fracture occurred in the base metal with a mixed mode of intergranular fracture with approximately 20-30% transgranular character [Fig. 59(a)]. This mode of fracture is indicative of unwelded DOP-26 alloys fractured under these conditions (see Fig. 48 above) [8,10,20,32]. Specimens tested at temperatures of 980°C and above tended to fracture at or very near the centerline of the weld. These specimens also showed predominantly a grain boundary fracture [Fig. 59(b)] with a very brittle appearance (even though ductilities were 9-15%). In all of the specimens that fractured near the weld centerline, some transgranular cleavage facets (estimated visually at approximately 5-10%) were also observed. The grains appearing on the fracture surface were elongated and parallel to the welding direction [Fig. 59(b)]. At low magnification, the grain boundaries were smooth and clean. However, at higher magnification (Fig. 60), second phase particles were visible which in some cases were aligned in long stringers along the welding direction. Figure 60 also shows that these precipitates were present on the weld metal grain boundaries but not on transgranular regions. Similar precipitates were also observed in welded specimens of old-process DOP-26 and were identified as being Th-based [21], and are probably Ir_5Th.

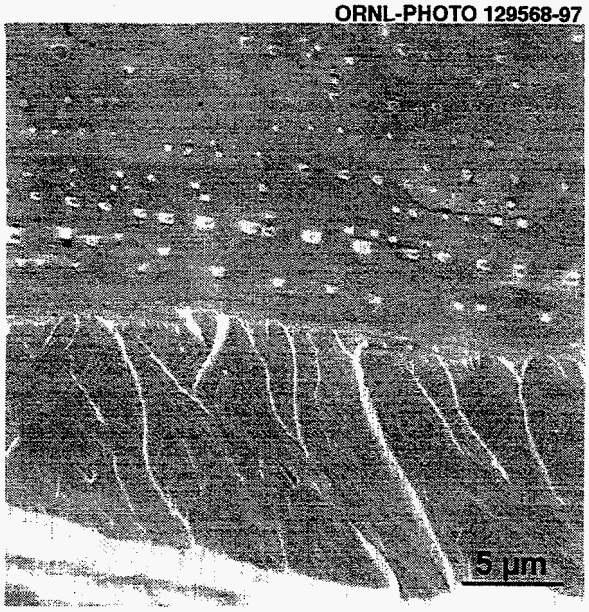

Fig. 60. High magnification scanning electron micrograph of the fracture surface of welded new-process DOP-26 high-strain-rate tested at 980°C showing the presence of Ir_5Th precipitates on the grain boundary (top half of micrograph) and absence of precipitates on transgranular region (lower half of micrograph). Fracture in this specimen occurred at the weld centerline.

Summary and Conclusions

In summary, based on heat treatments in vacuum for various times at 1400 and 1500°C, the base metal grain growth characteristics of welded new-process DOP-26 are not significantly different from that of the unwelded new-process DOP-26 materials. Additionally, the welded specimens of new-process DOP-26 exhibited high-temperature high-strain-rate tensile ductilities of 9-15% and did not appear to be dependent on the test temperature for tests between 900 and 1200°C. The welded specimens exhibited lower ductilities than unwelded specimens, mainly due to the coarser grain structure in the weld region. However, the high-temperature high-strain-rate tensile results for the new-process DOP-26 are comparable to that generated earlier for old-process DOP-26. These studies will continue with tests of specimens oriented parallel to the weld.

ACKNOWLEDGEMENTS

The authors gratefully acknowledge J. P. Moore (ORNL) and W. J. Barnett (USDOE) for program management and support. Thanks are also due to Janie Gardner, Elmer Lee, Joe Wright, and Herschel Pierce for technical assistance and C. T. Liu, Lee Heatherly, J. P. Moore, and W. J. Barnett for reviewing the manuscript.

REFERENCES

1. *Metals Handbook*, Ninth Edition, Vol. 2, ASM, Metals Park, OH, 1979, p. 740.

2. A. H. Cottrell, p. 7 in *The Mechanical Properties of Matter*, John Wiley and Sons, New York, 1964.

3. B. L. Mordike, and C. A. Brookes, *Platinum Metals Rev.* 4, 94 (1960).

4. S. S. Hecker, D. L. Rohr, and D. F. Stein, *Metall. Trans.* A9, 481 (1978).

5. C. T. Liu and H. Inouye, *Development and Characterization of an Improved Ir-0.3% W Alloy for Space Radioisotopic Heat Sources*, ORNL-5290, Oak Ridge National Laboratory, Oak Ridge, TN, October 1977.

6. G. B. Ulrich, p. 187 in *Heat-Resistant Materials*, edited by K. Natesan and D. J. Tillack, ASM International, Materials Park, OH, 1992.

7. T. G. George and M. F. Stevens, *JOM* 40(10), 32 (1988).

8. C. T. Liu, H. Inouye, and A. C. Schaffhauser, *Metall. Trans.* A12, 993 (1981).

9. C. T. Liu, H. Inouye, and A. C. Schaffhauser, *Metallurgical and Mechanical Properties of Thorium-Doped Ir-0.3% W Alloys*, ORNL-5616, Oak Ridge National Laboratory, Oak Ridge, TN, April 1980.

10. C. L. White, R. E. Clausing, and L. Heatherly, *Metall. Trans.* 10A, 683 (1979).

11. C. L. White and C. T. Liu, *Acta Metall.* 29, 301 (1981).

12. T. B. Massalski, editor-in-chief, *Binary Alloy Phase Diagrams*, ASM, Metals Park, OH, 1986.

13. D. E. Harasyn and A. C. Schaffhauser, *Metall. Trans.* A10, 823 (1979).

14. S. A. David and C. T. Liu, *Met. Tech.*, March 1980, pp. 102-106.

15. C. G. McKamey, E. H. Lee, J. W. Cohron, and E. P. George, *Scripta Mater.* 35, 181 (1996).

16. C. G. McKamey, A. N. Gubbi, Y. Lin, and E. P. George, *J. Alloys and Compounds* 244, 175 (1996).

17. E. K. Ohriner and E. P. George, "Plan to Evaluate Effects of Intermetallic Particle Distribution on Properties of DOP-26 Iridium Alloy," attachment to Letter No. 0719-66-91, M. M. Martin to W. J. Barnett, July 19, 1991.

18. E. K. Ohriner, p. 1093 in *Proc. 10th Symp. on Space Nuclear Power and Propulsion*, Am. Inst. of Physics, New York (1993).

19. E. K. Ohriner, p. 605 in *Proc. Int. Conf. on Tungsten and Refractory Metals*, Metal Powder Industries Federation, Princeton, NJ (1995).

20. A. N. Gubbi and E. P. George, unpublished results, 1995.

21. C. T. Liu and S. A. David, *Weld Metal Grain Structure and Mechanical Properties of Iridium Alloy DOP-26*, ORNL-5857, Oak Ridge National Laboratory, Oak Ridge, TN, August 1982.

22. Document No. GPHS-M-185 Rev. D, "General Purpose Heat Source Material Specification - Iridium Blanks," Oak Ridge National Laboratory, Oak Ridge, TN, August 1994.

23. D. J. McGuire, J. P. Moore, E. K. Ohriner, and G. B. Ulrich, *Production of Iridium Alloy and Carbon-Bonded Carbon Fiber Components for the Cassini Mission to Saturn*, ORNL-6933, Oak Ridge National Laboratory, Oak Ridge, TN, to be published, 1998.

24. L. E. Davis, N. C. McDonald, P. W. Palmberg, G. E. Riach, and R. E. Weber, *Handbook of AES*, Physical Electronic Industries, 1976.

25. C. Zener, *Trans. AIME* 175, 15 (1949).

26. M. Hillert, *Acta Metall.* 13, 227 (1965).

27. T. Gladman, *Proc. Roy. Soc.* A294, 298 (1966).

28. D. T. Gawne and G. T. Higgins, *J.I.S.I.* 209, 562 (1971).

29. J. J. Petrovic and L. J. Ebert, *Metall. Trans.* 3, 1131 (1972).

30. D. A. Porter and K. E. Easterling, p. 77 in *Phase Transformations in Metals and Alloys*, Van Nostrand Reinhold (UK) Co. Ltd., 1987.

31. J. J. Liao, Ph.D. Dissertation, Auburn University, 1992.

32. A. N. Gubbi, Ph.D. Dissertation, Auburn University, 1994.

33. Appendix B of "Final Safety Analysis Report For the Galilio Mission, Vol. 1, Reference Design Document," General Electric Company Astro-Space Division Document No. 87SDS4213, May 1988.

34. E. K. Ohriner, personal communication, August 1995.

35. J. P. Moore, Appendix B, "Final Safety Analysis Report for the Cassini Mission," May 1996.

INTERNAL DISTRIBUTION

1. Central Research Library
2. Document Reference Section
3. Laboratory Records Department
4. D. F. Craig
5. E. A. Franco-Ferrei
6-7. E. P. George
8. J. F. King
9. C. T. Liu
10. D. J. McGuire
11-16. C. G. McKamey
17. G. E. Michaels
18-20. J. P. Moore
21-22. E. K. Ohriner
23-24. G. B. Ulrich
25. M. R. Upton

EXTERNAL DISTRIBUTION

26. AMERICAN TECHNOLOGY, INCORPORATED, 142 Fairbanks Road, Oak Ridge, Tennessee 37830

    E. E. Hoffman

27-28. BABCOCK AND WILCOX OF OHIO, INCORPORATED, 1 Mound Road, Mail Stop 102-216, Miamisburg, Ohio 45343-3000

    D. M. Gabriel
    E. W. Johnson

29. JOHNS HOPKINS UNIVERSITY, Applied Physics Laboratory, 11100 Johns Hopkins Road, Laurel, Maryland 20723-6099

    Y. Chang

30-32. LOCKHEED MARTIN MISSILES AND SPACE, Building B, Post Office Box 8555, Philadelphia, Pennsylvania 19101

    L. E. DeFillipo
    R. J. Hemler
    R. M. Reinstrom

33-36. LOS ALAMOS NATIONAL LABORATORY, NMT-9, Mail Stop E502, Post Office Box 1663, Los Alamos, New Mexico 87545

E. M. Foltyn
T. G. George
M. A. Reimus
G. Rinehart

37-38. ORBITAL SCIENCES CORPORATION, 20301 Century Blvd., Mail Stop A-35, Germantown, Maryland 20874

R. T. Carpenter
E. A. Skrabek

39-40. TELEDYNE BROWN ENGINEERING-ENERGY SYSTEMS, 10707 Gilroy Road, Hunt Valley, Maryland 21031

S. T. Christenbury
M. F. McKittrick

41. TETRA TECH NUS, 910 Clopper Road, Gaithersburg, Maryland 20878

H. Firstenberry

42-43. WESTINGHOUSE ADVANCED TECHNOLOGY BUSINESS AREA, Post Office Box 355, Pittsburgh, Pennsylvania 15230-0355

C. E. Grosso
M. O. Smith

44-55. DEPARTMENT OF ENERGY, Space and National Security Programs, Germantown Building, 199901 Germantown Road, Germantown, Maryland 20874-1290

W. J. Barnett (NE-50)
C. E. Brown (NE-40)
B. A. Cook (NE-50)
J. Dowicki (NE-50)
R. R. Furlong (NE-50)
L. C. Herrera (NE-50)
R. G. Lange (NE-40)
A. S. Mehner (NE-50)
D. Owens (NE-50)
R. C. Raczynski (NE-50)
L. L. Rutger (NE-50)
E. A. Wahlquist (NE-50)

56. DEPARTMENT OF ENERGY, Albuquerque Field Office, Reimbursable and Energy Technologies Division, Post Office Box 5400, Albuquerque, New Mexico 87115

    R. L. Holton

57. DEPARTMENT OF ENERGY, Miamisburg Office, Post Office Box 66, Miamisburg, Ohio 45343-0066

    T. A. Frazier

58-59. DEPARTMENT OF ENERGY, Oak Ridge Operations Office, Post Office Box 2001, Oak Ridge, Tennessee 37831

    P. A. Carpenter
    S. R. Martin, Jr.